FINNISH METEOROLOGICAL INSTITUTE
CONTRIBUTIONS

No. 55

IONOSPHERE-ATMOSPHERE INTERACTION DURING SOLAR PROTON EVENTS

Pekka T. Verronen

Department of Physical Sciences
Faculty of Science
University of Helsinki
Helsinki, Finland

ACADEMIC DISSERTATION in physics

To be presented with the permission of the Faculty of Science of the University of Helsinki for public critisism in Small Audiorium E204 at Physicum in Kumpula Campus on May 20, 2006, at 10 a.m.

Finnish Meteorological Institute
Helsinki, 2006

ISBN 951–697–650–6 (paperback)
ISBN 952–10–3111–5 (pdf)
ISSN 0782–6117

Yliopistopaino
Helsinki, 2006

FINNISH METEOROLOGICAL INSTITUTE

Published by Finnish Meteorological Institute
(Erik Palménin aukio 1) , P.O. Box 503
FIN-00101 Helsinki, Finland

Series title, number and report code of publication
Contributions 55, FMI-CONT-55

Date
April 2006

Authors
Pekka T. Verronen

Name of project

Commissioned by

Title
Ionosphere-atmosphere interaction during solar proton events

Abstract
Among the most striking natural phenomena affecting ozone are solar proton events (SPE), during which high-energy protons precipitate into the middle atmosphere in the polar regions. Ionisation caused by the protons results in changes in the lower ionosphere, and in production of neutral odd nitrogen and odd hydrogen species which then destroy ozone in well-known catalytic chemical reaction chains. Large SPEs are able to decrease the ozone concentration of upper stratosphere and mesosphere, but are not expected to significantly affect the ozone layer at 15-30 km altitude.

In this work we have used the Sodankylä Ion and Neutral Chemistry Model (SIC) in studies of the short-term effects caused by SPEs. The model results were found to be in a good agreement with ionospheric observations from incoherent scatter radars, riometers, and VLF radio receivers as well as with measurements from the GOMOS/Envisat satellite instrument. For the first time, GOMOS was able to observe the SPE effects on odd nitrogen and ozone in the winter polar region. Ozone observations from GOMOS were validated against those from MIPAS/Envisat instrument, and a good agreement was found throughout the middle atmosphere.

For the case of the SPE of October/November 2003, a long-term ozone depletion was observed in the upper stratosphere. The depletion was further enhanced by the descent of odd nitrogen from the mesosphere inside the polar vortex, until the recovery occurred in late December. During the event, substantial diurnal variation of ozone depletion was seen in the mesosphere, caused mainly by the strong diurnal cycle of the odd hydrogen species.

In the lower ionosphere, SPEs increase the electron density which is very low in normal conditions. Therefore, SPEs make radar observations easier. In the case of the SPE of October, 1989, we studied the sunset transition of negative charge from electrons to ions, a long-standing problem. The observed phenomenon, which is controlled by the amount of solar radiation, was successfully explained by considering twilight changes in both the rate of photodetachment of negative ions and concentrations of minor neutral species.

Changes in the magnetic field of the Earth control the extent of SPE-affected area. For the SPE of November 2001, the results indicated that for low and middle levels of geomagnetic disturbance the estimated cosmic radio noise absorption levels based on a magnetic field model are in a good agreement with ionospheric observations. For high levels of disturbance, the model overestimates the stretching of the geomagnetic field and the geographical extent of SPE-affected area.

This work shows the importance of ionosphere-atmosphere interaction for SPE studies. By using both ionospheric and atmospheric observations, we have been able to cover for the most part the whole chain of SPE-triggered processes, from proton-induced ionisation to depletion of ozone.

Publishing unit
Earth Observation Unit

Classification (UDK)
551.510.413.3

Keywords
solar proton event, mesosphere,
stratosphere, ionosphere,
odd nitrogen, odd hydrogen, ozone

ISSN and series title
0782-6117 Finnish Meteorological Institute Contributions

ISBN
951-697-650-6 (paperback)
952-10-3111-5 (pdf)

Language
English

Sold by
Finnish Meteorological Institute / Library
P.O.Box 503, FIN-00101 Helsinki
Finland

Pages
146

Price

Note

ILMATIETEEN LAITOS

Julkaisun sarja, numero ja raporttikoodi
Contributions 55, FMI-CONT-55

Julkaisija Ilmatieteen laitos, (Erik Palménin aukio 1)
PL 503, 00101 Helsinki

Julkaisuaika
Huhtikuu 2006

Tekijä(t)
Pekka T. Verronen

Projektin nimi

Toimeksiantaja

Nimeke
Ionosfääri-ilmakehä-vuorovaikutus auringon protonimyrskyjen aikana

Tiivistelmä
Auringon protonimyrskyt ovat yksi keski-ilmakehän otsoniin vaikuttavista luonnonilmiöistä. Protonimyrskyn aikana korkeaenergiset protonit tunkeutuvat maan ilmakehään napa-alueilla ja ionisoivat ilmakehän kaasuja. Myrskyn seurauksena tapahtuu ionosfäärissä muutoksia, jotka johtavat parittoman typen ja parittoman vedyn oksidien tuottoon. Nämä oksidit toimivat katalyytteinä otsonia tuhoavissa kemiallisissa reaktioissa. Suuret protonimyrskyt vähentävät otsonin määrää ylä-stratosfäärissä sekä mesosfäärissä, mutta niiden ei ole havaittu vaikuttavan merkittävästi otsonikerrokseen 15-30 km korkeudella.

Tässä väitöstyössä on tutkittu Sodankylän ioni- ja neutraalikemiamallilla (SIC) protonimyrskyjen aiheuttamia lyhytaikaisia muutoksia. Mallin tulosten todettiin vastaavan hyvin ionosfääritutka-, riometri- ja VLF-radioaaltomittauksia sekä GOMOS/Envisat-satelliittimittalaitteen havaintoja. GOMOSin avulla voitiin ensimmäistä kertaa havaita protonimyrskyn aiheuttamat otsonin ja parittoman typen muutokset pohjoisella talvinavalla. GOMOSin otsonimittausten luotettavuus tarkistettiin vertaamalla niitä MIPAS/Envisat-mittalaitteen havaintoihin, ja vastaavuus todettiin hyväksi koko keski-ilmakehän korkeusalueella.

Loka-marraskuun 2003 aurinkomyrskyjen jälkeen havaittiin pitkäaikainen otsonin väheneminen ylä-stratosfäärissä. Otsonin määrän todettiin edelleen vähenevän parittoman typen laskeutuessa alas mesosfääristä polaaripyörteen sisällä, kunnes palautuminen tapahtui joulukuun lopulla. Myrskyn aikana mesosfäärin otsonin muutoksissa todettiin selkeä vuorokausivaihtelu, mikä johtui pääasiassa yö/päivä-muutoksista parittoman vedyn määrässä.

Ala-ionosfäärissä protonimyrkyt kasvattavat elektronitiheyttä, joka normaalioloissa on erittäin alhainen. Täten myrskyt helpottavat merkittävästi tutkahavaintojen tekemistä. Lokakuun 1989 protonimyrskyn tapauksessa tutkittiin ala-ionosfäärissä auringonlaskun aikana tapahtuvaa siirtymää elektroneista negatiivisiin ioneihin. Havaittu, auringon säteilyn määrän kontrolloima ilmiö pystyttiin selittämään ottamalla huomioon muutokset sekä fotohajoamisen nopeudessa että pienkaasujen pitoisuuksissa.

Maan magneettikentän muutokset vaikuttavat protonimyrskyn vaikutusalueen laajuuteen. Marraskuun 2001 protonimyrskyn tutkimus näytti, että alhaisille ja keskisuurille häiriötiloilla maan magneettikenttää kuvaavan mallin perusteella laskettu kosmisen radiosäteilyn vaimeneminen vastaa hyvin ionosfäärimittauksia. Korkeille häiriötiloille malli yliarvioi magneettikentän venymisen ja protonien vaikutusalueen laajuuden.

Tämä työ osoittaa ionosfääri-ilmakehä-vuorovaikutuksen tärkeyden protonimyrskytutkimukselle. Hyödyntämällä sekä ionosfääri- että ilmakehämittauksia voitiin suurelta osin kattaa koko myrskyjen laukaisema prosessiketju, alkaen protonien aiheuttamasta ionisaatiosta aina otsonin vähenemiseen saakka.

Julkaisijayksikkö
Kaukokartoitusyksikkö

Luokitus (UDK)
551.510.413.3

Asiasanat
auringon protonimyrsky, mesosfääri, stratosfääri, ionosfääri, pariton typpi, pariton vety, otsoni

ISSN ja avainnimike
0782-6117 Finnish Meteorological Institute Contributions

ISBN
951-697-650-6 (pehmeäkantinen)
952-10-3111-5 (pdf)

Kieli
Englanti

Myynti
Ilmatieteen laitos / Kirjasto
PL 503, 00101 Helsinki

Sivumäärä
146

Hinta

Lisätietoja

Contents

Thankyous

This work has been hosted by the Finnish Meteorological Institute (under Directors General Prof. Erkki Jatila and Prof. Petteri Taalas), first in the Geophysical Research Division (Directors Prof. Risto Pellinen and Prof. Tuija Pulkkinen) and during the last years in the Earth Observation Unit (Director Prof. Jarkko Koskinen) of the Research and Development Division (Director Prof. Yrjö Viisanen).

I thank Prof. Erkki Kyrölä and Ph.D. Esa Turunen, my supervisors, for their trust, support, and guidance over the years. I also thank my professor at the University of Helsinki, Prof. Hannu Koskinen, for his space physics courses and advice. Further, I thank Prof. Tuomo Nygrén and Prof. Donal Murtagh for the careful inspection of my thesis.

Regarding the original papers, I thank my co-authors for fruitful collaborations, especially the magnificent CHAMOS team. I gratefully acknowledge the extensive amount of effort by the international GOMOS team, started about ten years before my arrival at the Finnish Meteorological Institute, which has been essential to my work.

I thank my colleagues at the Finnish Meteorological Institute during the years for the pleasant working atmosphere. I also thank the personnel of Sodankylä Geophysical Observatory for making me feel so welcome during my numerous visits to the north.

Finally, I would like to thank my wife Heidi, my daughters Annisofia and Ainomaria, and my parents Leena and Heikki for their support. I wish to dedicate this work to my grandmother Seidi Sofia, who past away last year.

This work has been for the most part funded by the Academy of Finland, first through the Finnish Graduate School in Astronomy and Space Physics (Directors Prof. Jorma Kangas and Prof. Tuomo Nygrén), and later through the ANTARES space research programme. During this work I have received travel grants from the Vilho, Yrjö, and Kalle Väisälä foundation and the Magnus Ehrnrooth foundation.

Helsinki, April 20, 2006

Pekka T. Verronen

List of original publications

I Seppälä, A., Verronen, P. T., Kyrölä, E., Hassinen, S., Backman, L., Hauchecorne, A., Bertaux, J. L., and Fussen, D., Solar Proton Events of October-November 2003: Ozone depletion in the Northern hemisphere polar winter as seen by GOMOS/Envisat, *Geophysical Research Letters*, *31*, L19 107, 2004.

II Verronen, P. T., Seppälä, A., Clilverd, M. A., Rodger, C. J., Kyrölä, E., Enell, C.-F., Ulich, Th., and Turunen, E., Diurnal variation of ozone depletion during the October-November 2003 solar proton events, *Journal of Geophysical Research*, *110*, A09 S32, 2005.

III Verronen, P. T., Kyrölä, E., Tamminen, J., Funke, B., Gil-López, S., Kaufmann, M., López-Puertas, M., Clarmann, T.v., Stiller, G., Grabowski, U., and Höpfner, M., A comparison of night-time GOMOS and MIPAS ozone profiles in the stratosphere and mesosphere, *Advances in Space Research*, *36*, 958–966, 2005.

IV Verronen, P. T., Ulich, Th., Turunen, E., and Rodger, C. J., Sunset transition of negative charge in the D-region ionosphere during high-ionization conditions, *Annales Geophysicæ*, *24*, 187–202, 2006.

V Rodger, C. J., Clilverd, M. A., Verronen, P. T., Ulich, Th., Jarvis, M. J., and Turunen, E., Dynamic geomagnetic rigidity cutoff variations during a solar proton event, Accepted for publication in *Journal of Geophysical Research*, 2006.

1 Introduction

Ozone is one of the key constituents of the atmosphere. Despite its relatively small abundance, it effectively absorbs a great part of the UV radiation. Therefore, ozone plays an important role in the energy budget and dynamics of the atmosphere, and at the same time protects the life on Earth [*e.g.* Brasseur and Solomon, 2005]. The last 20 years have been times of intense ozone research due to the effects of man-made CFC gases on the ozone amount, and especially because of the discovery of the spring-time ozone hole over Antarctica [Farman et al., 1985]. Today, the ozone hole can be explained by heterogeneous reactions taking place on surfaces of polar stratospheric cloud (PSC) particles, which convert chlorine from inactive to active, ozone-destroying forms [Solomon, 1999, and references therein]. An important part in the ozone hole formation is played by the polar vortex which confines the air inside, thus preventing mixing and resulting in very cold temperatures and PSC formation. In the Arctic the polar vortex is typically not as cold and stable as in the Antarctic, and the observed ozone loss there has been less dramatic [Brasseur and Solomon, 2005, pp. 482–491]. However, since the 1990s several exceptionally cold winter periods have occurred, during which the Arctic ozone loss tends to strengthen. Although the reasons for the stratospheric cooling are not well known, it has been related to, *e.g.*, greenhouse gas emissions or dynamical changes caused by tropospheric wave pattern oscillations.

Atmospheric ozone is also affected by natural causes, *e.g.* due to volcanic eruptions or changes in the solar forcing. For example, the solar ultraviolet flux varies with the 11 year solar cycle much more strongly than the total solar irradiance. Also, ultraviolet radiation received by the atmosphere changes by about 7% with the variation of the distance between the Sun and the Earth. These kind of variations may modulate the middle atmospheric ozone [*e.g.* Callis et al., 1991]. Therefore, when estimating the changes caused by anthropological sources, it is essential to contrast them with variations and changes due to natural processes.

Among the most striking natural phenomena affecting ozone are solar proton events (SPE), during which energetic solar protons precipitate into the middle atmosphere in the polar regions. Ionisation caused by the protons results in production of odd nitrogen and odd hydrogen species, which then destroy ozone in catalytic chemical reactions. SPEs are not the cause of the ozone hole and are not expected to significantly affect the lower stratospheric ozone, *i.e* the ozone layer. Nevertheless, the substantial perturbations caused by the largest SPEs are extremely useful in testing our understanding of the upper stratospheric and mesospheric photochemistry of ozone and related species [Jackman and McPeters, 2004]

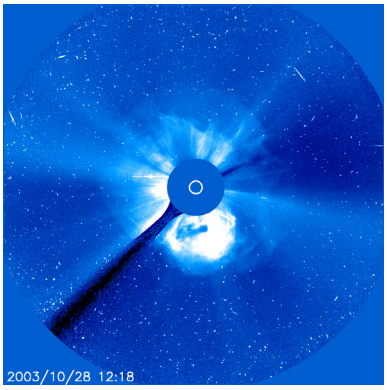

FIGURE 1.1. A coronal mass ejection on October 28, 2003 as seen by the LASCO instrument on board the European Space Agency's SOHO satellite. The Sun is located behind the circular protection cover in the middle of the picture and the CME is seen as a white cloud leaving the Sun.

1.1 Solar proton events and the middle atmosphere

1.1.1 From coronal mass ejection to ozone depletion

Solar proton events (SPE), also known as polar cap absorption (PCA) events in the history of radio physics, begin as emission of electrons and ions from the surface of the Sun. The ions are mostly protons ($\approx 90\%$) but heavier particles are also emitted, the relative abundances being similar to those in the solar corona. For the most energetic coronal mass ejections (CME), particle energies can be up to MeV or even GeV level, thus far exceeding the normal solar wind values, *e.g.* $\sim$1 keV for protons. The acceleration of emitted particles is driven by processes related to the solar flare accompanying the CME, and/or by solar wind shock fronts [*e.g.* Cane et al., 2003]. Fig. 1.1 shows an observation of a CME being ejected from the Sun.

Even particles having GeV energies are guided by the interplanetary magnetic field (IMF) over the Sun-Earth distance [*e.g.* Hargreaves, 1992, pp. 353–355]. Therefore, the emitted particles will follow the spiral field lines of IMF, and the location of the CME on the solar surface will determine whether or not the released particles will hit the Earth's magnetosphere. Also, the guidance of IMF results in some additional time delay between the CME and the arrival of particles at the Earth. Typically, a delay of several hours is observed. Particles having different energies have different Larmor radii, and the particles with lower energies are more sensitive to the form of IMF. As a result, the bulk velocity of the particle "cloud" is much less than that of individual particles, which can be used to explain the duration of near-Earth effects, typically of the order of days, and the isotropic

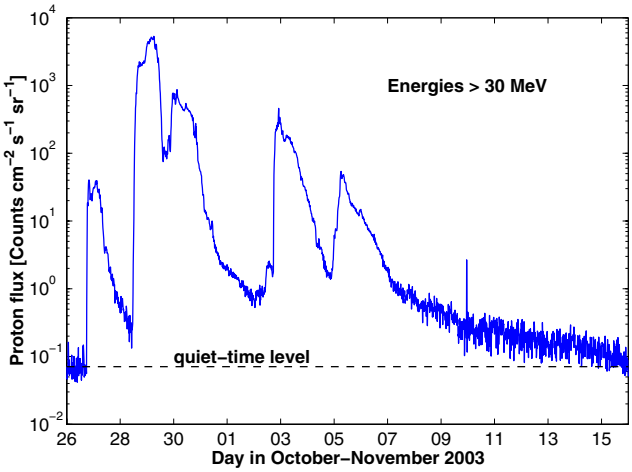

FIGURE 1.2. High-energy proton flux measurements by GOES satellite in the late October, 2003. Note the increase of flux by several orders of magnitude. The series of SPEs begins on October 26 and the flux values return to the quiet-time level in mid November.

angular distribution of the particles near the Earth. Fig. 1.2 shows measured proton fluxes in the geostationary orbit after a large CME.

In order to reach the atmosphere of Earth, the particles have to penetrate the magnetosphere, which requires relatively high energies. The magnetospheric trajectories of high-energy particles can be calculated using the Størmer theory [Størmer, 1930]. Because the Larmor radii of these particles are relatively large ($\sim$1000 km), a uniform magnetic field cannot be assumed during one gyration and the particle trajectories can be very complex, even when assuming a simple dipole field. Particles travelling along the magnetic field lines are least affected, and thus the polar regions, where the field lines penetrate the atmosphere and the Earth's surface, are easier to access. According to the Størmer theory, every geomagnetic latitude has a cutoff limit which the rigidity of an incoming particle (defined as momentum per charge) must exceed in order it to reach that particular location. Penetration to lower latitudes requires higher rigidities, and a certain latitude is affected by particles having rigidity equal to, or higher than the corresponding cutoff. The cutoff rigidity varies spatially and also with time, being dependent on the IMF on as well as on the Earth's internal magnetic field, on timescales from minutes to years. The magnetic storms, for example, tend to compress the magnetosphere and lower the cutoff rigidity for a given latitude. Fig. 1.3 shows calculated cutoff energies for medium level of geomagnetic disturbance. As a consequence of geomagnetic cutoff, the particles are able to affect atmosphere above a certain magnetic latitude, covering the polar cap regions in both hemispheres.

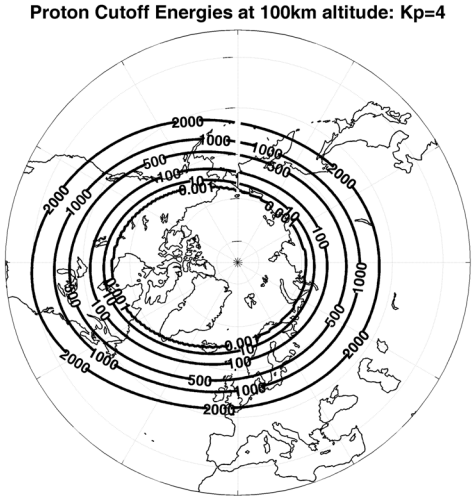

FIGURE 1.3. Estimated proton cutoff energies for the Northern Hemisphere (courtesy of C. J. Rodger, University of Otago). Medium level of geomagnetic disturbance. Energy contours are in MeV.

Typically latitudes above about 60° are affected more or less uniformly, although the effects have sometimes been observed near the geomagnetic poles first, and later throughout the polar cap.

As particles propagate down into the atmosphere they lose their energy in collisions with atmospheric gases. In such a collision, with the proton energies considered, the atmospheric molecule is ionised, and an ion-electron pair is created. In addition to the primary protons, the secondary electrons produced in ionisation may have enough energy to further ionise and dissociate atmospheric gases. Approximately 36 eV of energy is required in the production of one ion pair [*e.g.* Rees, 1989, pp. 35–45], thus a proton with 10 MeV initial energy is able to ionise about 280,000 molecules along its path before all the energy is lost. The atmospheric penetration depth is dependent on the particle energy, the 1–500 MeV solar protons depositing their energy in the mesosphere and stratosphere [*e.g.* Hargreaves, 1992, pp. 217–218]. The most energetic protons, with $E > 1$ GeV, are able to reach the ground level, although at these energies the galactic cosmic rays generally predominate.

The ionisation caused by solar particle precipitation can far exceed the normal geomagnetically quiet-time sources in the middle atmosphere, see Fig. 1.4. As a result the ion concentrations are significantly elevated at altitudes below about

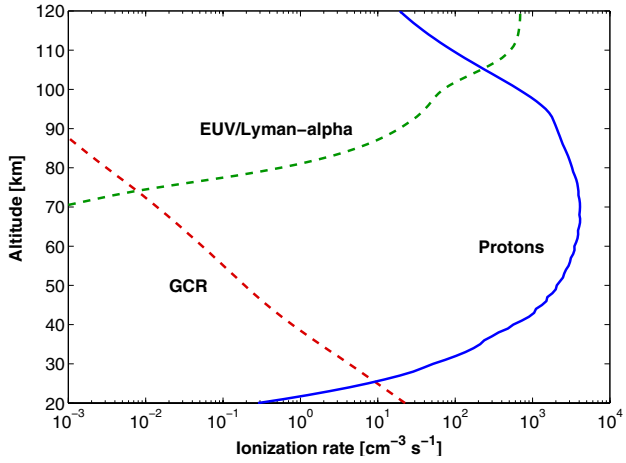

FIGURE 1.4. Calculated ionisation rate due to solar proton precipitation on October 29, 2003, contrasted with high-latitude, quiet-time ionisation rates by galactic cosmic rays (solar maximum) and solar EUV/Lyman-α radiation (SZA = 83.5°). Sodankylä Ion and Neutral Chemistry model results.

100 km and the ion composition may also change. The ion concentrations are closely tied to the ionisation level, and after a reduction in proton forcing the fast recombination with free electrons results in a quick return to quiet-time levels. SPEs also lead to changes in atmospheric composition, including the increase of odd nitrogen (NO_x = N + NO + NO_2) and odd hydrogen (HO_x = H + OH + HO_2), and the subsequent loss of ozone. NO_x is produced in dissociation of molecular nitrogen by the primary and secondary solar particles and, to a lesser extent, in ion chemical reactions following the ion pair production. Production of HO_x is solely due to ion chemistry, involving a rather complex scheme of water cluster ion reactions. The depletion of ozone is due to the increase of NO_x and HO_x, which accelerates the catalytic ozone loss cycles involving these species. The magnitude and duration of depletion depends on the particle flux, altitude, season (solar illumination level and atmospheric dynamics), and the chemical state of the atmosphere. The short-term ozone depletion due to HO_x increase lasts some hours and can be greater than 90% in the middle mesosphere, while the long-term decrease, several tens of percent, is typically seen in the upper stratosphere and is due to NO_x increase. Because of the long chemical lifetime of NO_x, the effects on ozone can last for months and the produced NO_x can be transported from the location of the precipitation, so that lower altitudes and latitudes may also be affected. The effect on global, total ozone is considered to be moderate, of the order of few percent at the maximum [Jackman et al., 1996]. Fig. 1.5 presents upper stratospheric measurements of ozone, made after a large SPE.

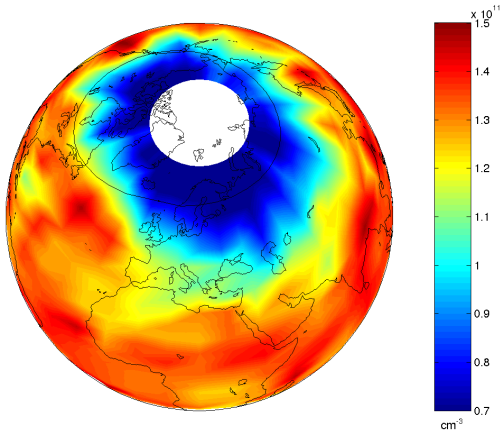

FIGURE 1.5. Northern hemispheric distribution of ozone at 46 km altitude after the October-November 2003 SPE (courtesy of A. Seppälä, Finnish Meteorological Institute). The map is constructed using GOMOS measurements. Note the low amounts of ozone in the polar region.

SPEs provide a direct connection between the Sun and the Earth's middle atmosphere. They are relatively sporadic but tend to be more probable during times of maximum solar activity. Tens of SPEs may occur during a solar cycle, but only in few cases the protons have energies sufficient to penetrate down to the stratopause region. However, those cases are extreme examples of solar forcing on the middle atmosphere and can significantly affect the lower ionosphere and middle atmosphere. The magnitude of an SPE can be determined using the peak flux unit (pfu) for > 10 MeV protons, measured in the geostationary orbit and given in $\mathrm{cm}^{-2}\ \mathrm{sr}^{-1}\ \mathrm{s}^{-1}$. In the last 35 years, exceptionally large events with $pfu > 10,000$ have occurred in 1972, 1989, 1991, 1994, 2000, 2001, and 2003. A more or less complete list of SPEs, including pfu values, can be found from, *e.g.*, *http://umbra.nascom.nasa.gov/SEP/seps.html* (accessed in December, 2005).

1.1.2 Brief review of research to date

The existence of solar proton events was realised in the 1950s after a large solar flare in February, 1956, was followed by radio communication blackouts that lasted for several days. Early work, which was based on the HF and VHF radio techniques already identified this polar region phenomenon as a result of enhancement in ionospheric D-region ionisation due to precipitating high-energy protons of solar origin [Bailey, 1964, and references therein], which was soon confirmed by

in-situ experiments [Reid and Collins, 1959; Anderson and Enemark, 1960]. Since then, the lower ionospheric characteristics during SPEs, *e.g.* day/night differences and twilight asymmetries in electron density, have been studied using especially riometer measurements of cosmic radio noise absorption [Reid, 1961; Gillmor, 1963; Chivers and Hargreaves, 1965]. Later studies of SPEs, making use of the incoherent scatter radar technique [Reagan and Watt, 1976; Hargreaves et al., 1987; Collis and Rietveld, 1990; Turunen, 1993] or subionospheric propagation of VLF signals [*e.g.* Westerlund et al., 1969; Clilverd et al., 2005a], have provided important insight to the composition and processes of D-region ionosphere.

Neutral atmospheric changes due to solar proton events were predicted by Hertzberg [1960] and Dalgarno [1971], who put forward the possibility of odd nitrogen production by particle precipitation. The importance of this to the ozone balance was later pointed out by Crutzen et al. [1975]. After the first measurements of middle atmospheric ozone were made during an SPE using rocket and satellite instruments [Weeks et al., 1972; Heath et al., 1977], it was evident that odd nitrogen increase alone could not explain the ozone depletion observed in the mesosphere, and Swider and Keneshea [1973] suggested odd hydrogen production due to ion chemical reactions as a possible reason. The theory of odd nitrogen and odd hydrogen production during proton precipitation was then refined in studies by Porter et al. [1976], Heaps [1978], Rusch et al. [1981], and Solomon et al. [1981]. After the July 1982 SPE it was shown by Solomon et al. [1983] and Jackman and McPeters [1985] that theoretical predictions were qualitatively in a good agreement with satellite measurements of ozone [Thomas et al., 1983; McPeters and Jackman, 1985], although around the stratopause region the observed depletions were significantly larger than the predicted ones. McPeters and Jackman [1985] and Jackman et al. [1990] studied the SPEs between 1979 and 1983 using ozone observations and model predictions, and found ozone depletion to take place only after the largest events.

The focus was then turned on the long-term effects of the SPEs. Middle and upper stratospheric enhancement of NO_x lasting from several months to years was predicted in the polar latitudes due to the October 1989 SPE, while the subsequent fate of the produced NO_x and effect on ozone was found to be strongly dependent on the illumination conditions and transport processes, such as the structure of polar vortex [Reid et al., 1991; Jackman et al., 1995]. While SPEs can significantly enhance the odd nitrogen production locally, the annual high-latitude odd nitrogen production due to SPEs has been estimated to be moderate for most years when compared to other middle atmospheric sources, showing orders-of-magnitude variation from year to year, and exceeding the other production sources only during the years when major SPEs occurred [Jackman et al., 1980; Vitt and Jackman, 1996]. The effects of the two exceptionally large events (in 1972 and 1989) were compared by Jackman et al. [2000], who showed that the

chemical state of the stratosphere has a significant impact on the modelled long-term effects. The SPE effect on total ozone column has been found to be fairly small, *e.g.* a few percent after the major SPE of October 1989 [Jackman et al., 1996], although measurements of proton fluxes at the highest energies that could directly affect the altitudes of ozone layer are lacking. Sinnhuber et al. [2003] have shown that if the structure and strength of the geomagnetic field change significantly, *e.g.* during a polarity transition (which tends to occur at irregular intervals of about 200,000 years), the total ozone could be reduced by tens of percent due to SPEs which would drastically alter the temperature and dynamics of the middle atmosphere.

Studies of the HO_x and NO_x enhancement during SPEs were for a long time based on modelling and indirect observations, *i.e.* ozone measurements. Especially for HO_x, there have been no measurements until very recently. Using measurements from the SBUV/Nimbus 7 instrument, an increase in the column density of nitric oxide had been observed in the mesosphere and thermosphere after the July 1982 SPE by McPeters [1986], who noted the hemispheric differences in duration of the enhancement due to different illumination conditions. However, the first *in-situ* rocket measurements of NO were made during the great SPE in October, 1989 [Zadorozhny et al., 1992; Zadorozhny et al., 1994], the observations showed order-of-magnitude increase in the stratopause region in a good agreement with theoretical predictions. First simultaneous satellite measurements of NO, NO_2 and ozone were made during the July 2000 SPE by the HALOE/UARS instrument, and a good agreement with model predictions was found although the ozone depletion around the stratopause was underestimated in the modelling Jackman et al. [2001]. Randall et al. [2001], using the HALOE/UARS instrument, observed elevated concentrations of NO_2 in the middle stratosphere several months after the event, probably due to NO_x descent from mesospheric altitudes inside the polar vortex.

1.1.3 Open questions

Although SPEs have been studied for about 50 years, there are still open questions concerning their effects in the atmosphere. Basic theory of HO_x and NO_x increase, and the subsequent ozone loss, has been quite successfully tested with ozone and NO_x measurements. However, these observations have been limited in both time and space, such that only observations of sunlit atmosphere have been available. This has restricted the testing of the theories in the winter pole region, and the polar night effects have been based almost entirely on model predictions. Another great need is for measurements of odd hydrogen species during SPE conditions, since to date no such observations have been available. The process of HO_x production is complex, involving ion chemistry, and there are a number uncertainties

in the currently used models. Therefore, HO_x observations could significantly help to test and understand not only atmospheric response but also ionospheric response, and this kind of measurements might be the key in interpreting the differences found between observations and model predictions in the stratopause region [see, *e.g.*, Jackman et al., 2001].

As mentioned above, the satellite instruments used in the previous studies were dependent upon the solar light, such that they could provide direct information on the daytime changes only. However, when a large SPE occurred in October-November, 2003, there were a number of new instruments in orbit, some of which were capable of night-time observations of multitude of atmospheric species [Papers I and II as well as Degenstein et al., 2005; Rohen et al., 2005; Clarmann et al., 2005; Lopéz-Puertas et al., 2005a,b; Orsolini et al., 2005]. Data from these instruments will undoubtedly expand our knowledge on the atmospheric effects of SPEs, both short-term and long-term, in more detail that was possible before. Although the lack of night-time measurements has now been overcome in SPE research, the absence of HO_x measurements still remains. Observations from the MLS instrument on board the EOS-Aura satellite, made during the January 2005 SPE, may prove useful in studies of HO_x production in the near future.

1.2 Scope of this work

One of the pre-launch scientific goals for the GOMOS instrument, on board the European Space Agency's Envisat satellite (see Section 3.2.1 for details on GOMOS), was SPEs and their effects on the winter pole middle atmosphere, in low illumination conditions [Verronen et al., 1999]. In October, 2003, one of the largest SPEs in 50 years occurred, and GOMOS was able to measure both enhancement of odd nitrogen and depletion of ozone in the Northern Hemisphere polar region. GOMOS lived up to the high expectations and provided unique data of stratospheric and mesospheric changes during the SPE. These data are really the backbone of this Ph.D. thesis.

Another important part of this work has been the conversion of the Sodankylä Ion Chemistry model (SIC) into a combined ion and neutral photochemistry model, details of which will be given in Chapter 4. The pure ion chemistry model was taken by the author of this thesis in the late 1990s as a basis for the development work, with the idea of detailed modelling the production of HO_x and NO_x, and the subsequent depletion of ozone in the middle atmosphere during SPEs, using the latest information on ion and neutral chemical processes. Since then, the new SIC model has been successfully used in several such studies.

In addition, the new input of this work to the SPE research comes from the utilisation of both ionospheric and atmospheric measurements. Traditionally,

the ionospheric and atmospheric science communities have been rather separated, showing different interests in studies of SPEs. This kind of separation is, of course, artificial because the ionosphere and the neutral atmosphere are not individual entities but are closely connected to each other. For this work, using a combined ion and neutral chemistry model, it is natural to take advantage of both ionospheric and neutral atmospheric observations, because it allows for a better insight of the chain of processes starting from proton-induced ionisation and leading to ozone depletion.

This thesis consists of an introductory part and five original publications, which are referred to as Papers I–V. In the remaining introduction, Chapter 2 outlines some characteristics of the lower ionosphere, discusses formation and loss of odd nitrogen, odd hydrogen, and ozone in the middle atmosphere, and gives a description of the changes caused by the solar proton events. Observations of perturbations caused by SPEs are outlined in Chapter 3, with a special focus on the measurements used in this thesis work. Chapter 4 gives a detailed description of the Sodankylä Ion and Neutral Chemistry model, SIC, discussing its features and applicability. Chapter 5 summarises the results of the original papers and concluding remarks then are given in Chapter 6.

In addition to the more detailed summary given in Chapter 5, the contents of papers I–V are briefly outlined below, noting also the contribution of the author of this thesis to each of them.

I Increase of NO_x, its descent inside the polar vortex, and subsequent long-term depletion of ozone are studied after the SPE of October/November 2003. GOMOS observations of NO_2 and ozone are used. P. T. Verronen contributed significantly to the analysis and interpretation of the data and wrote approximately half of the text.

II Ozone depletion during the SPE of October/November 2003 is studied with a special interest on its diurnal variation in the mesosphere. SIC model results are used together with VLF signal propagation measurements and observations of NO_2 and ozone from the GOMOS instrument. P. T. Verronen executed the SIC model runs, analysed them and the GOMOS data, and wrote the text, except for the VLF parts.

III Night-time ozone measurements from the GOMOS instrument are validated by comparing them with those from the MIPAS instrument. P. T. Verronen made most of the data analysis, and wrote the text with the MIPAS parts being significantly contributed to by the co-authors.

IV Sunset transition of negative charge from electrons to negative ions is studied during the SPE of October 1989. A variety of ionospheric observations as well as rocket measurements of neutral nitric oxide are used together with

the SIC model. P. T. Verronen executed the SIC model runs, analysed the measurement data together with the co-authors, and wrote the text of the paper.

V Geomagnetic cutoff variation during the SPE of November 2001 are studied using SIC model results and cosmic radio noise absorption measurements. A method based on satellite observations, magnetic field modelling, and measured planetary magnetic index provides proton cutoff energies that are used to modify the SIC input flux of protons. P. T. Verronen executed the SIC model runs and contributed to the analysis of the model output.

2 Photochemical effects of proton precipitation in the middle atmosphere

2.1 Increase in ionisation

Energy input into the atmosphere by short-wave solar radiation and precipitating energetic particles results in ionisation of atmospheric neutral constituents, creating the ionosphere, a region of the atmosphere which is partly ionised (0.1% or less) and of net neutral charge. Ionosphere is traditionally divided into altitude regions with different ionisation sources and electron density levels. Table 2.1 gives the main characteristics of these layers.

The D region is located at altitudes below 95 km. Permanent ionisation is provided by solar radiation, especially Lyman-α affecting nitric oxide (NO) and, to a lesser extent, EUV (102.7–111.8 nm) acting on $O_2(^1\Delta_g)$ [Hargreaves, 1992, pp. 229–231]. At altitudes below 60 km the main quiet time ionisation source is galactic cosmic rays (GCR). Lyman-α flux varies with both the 11-year solar cycle and the 27-day rotational period, but the variation is by a factor of two and is thus relatively moderate compared to much larger variations at shorter EUV and X-ray wavelengths [Brasseur and Solomon, 2005, pp. 164–169]. The diurnal variation is naturally substantial and the night-time fluxes, due to scattering by the geocorona, are about 100 to 1000 times lower than the direct Lyman-α flux. Also GCR varies with the 11-year solar cycle, showing up to an order of magnitude larger fluxes during solar minima. Its variation, and the fluxes in general, are larger at higher latitudes.

The permanent, quiet-time ionisation rates at D-region altitudes vary from 10^4 to 10^7 m^{-3} s^{-1} [*e.g.* Brasseur and Solomon, 2005, pp. 552–553]. These ion production rates are relatively low compared to levels at the higher altitudes so that sporadic and strong ionisation sources affecting the D region, such as hard X-rays ($\lambda < 1$ nm) during high solar activity and especially during solar flares or relativistic electron precipitation (REP) from radiation belts, are able to enhance the ion pair production levels in the D region high above the typical conditions. X-rays affect the whole sunlit atmosphere while REPs occur in the sub-auroral latitudes ($60 - 70^\circ$) and are more probable during the declining phase of the solar cycle. Auroral electron precipitation normally ionises the E region at auroral latitudes, although sometimes the D region is also affected if the electrons have a higher energy.

As noted in Section 1.1, large solar proton events, another sporadic source of ionisation, affect the polar cap areas above $\sim 60^\circ$ magnetic latitude and may cause maximum ionisation around the stratopause region or below depending upon the proton spectrum. They can thus influence both the mesosphere and upper strato-

Region	Altitude	Ionisation source	Electron density	Primary ions
F	>130 km	EUV (9–91 nm)	$10^{11} - 10^{12}$ m^{-3}	O^+/N_2^+
E	95–130 km	X-rays/Lyman-β	$10^{9} - 10^{11}$ m^{-3}	O_2^+/NO^+
D	60–95 km	Lyman-α/GCR	$10^{8} - 10^{9}$ m^{-3}	NO^+

Table 2.1 Daytime characteristics of ionospheric regions [Brasseur and Solomon, 2005, pp. 533–536].

sphere. Peak ionisation rate can exceed 10^{10} m^{-3} s^{-1} and elevate the ionisation rate by several orders of magnitude above the normal background levels.

2.2 Effects on ion composition

D-region ion chemistry is quite complex compared to that of the upper ionospheric regions. This is due to the fact that minor constituents, being much more abundant than in the E region, significantly participate in the photochemistry of ions together with the main constituents. In addition to simple molecular ions, such as O_2^+ and NO^+ which are first produced, a multitude of other ions with significant concentrations exists, including water cluster ions as well as negative ions. In fact, rocket measurements have shown that below about 80 km the main positive ions are H^+ hydrates [Brasseur and Solomon, 2005, pp. 559–564]. The order of hydration *i.e.* the number of water molecules attached to an ion, which is typically from 2 to 4 but can be as high as 20, is dependent on the geophysical conditions. Lower temperatures and higher concentrations of H_2O favour higher orders of hydration.

Negative ions hold a substantial portion of the negative charge in the D-region ionosphere. The existence of negative ions was theoretically predicted based on observed diurnal variations of electron density, and later confirmed by rocket measurements [Johnson et al., 1958]. Negative ion chemistry is initiated by electron attachment to molecular oxygen

$$O_2 + e + M \rightarrow O_2^- + M \tag{2.1}$$

after which subsequent reactions lead to formation of more stable ions, *e.g.* NO_3^-, CO_3^-, and HCO_3^-, of which NO_3^- is especially stable because of its high electron affinity [*e.g.* Shimazaki, 1984]. Cluster ions can also be formed in reactions with, *e.g.*, water molecules. However, there are few measurements of negative ion composition available, and several issues related to their vertical distribution are still to be solved [Brasseur and Solomon, 2005, pp. 571–577]. Negative ions are present at altitudes below 80 km, where the atmospheric density is high enough so that the 3-body reaction of Eq. (2.1) is efficient. The balance with electrons is then determined by electron detachment reactions such as

$$O_2^- + O \rightarrow O_3 + e. \tag{2.2}$$

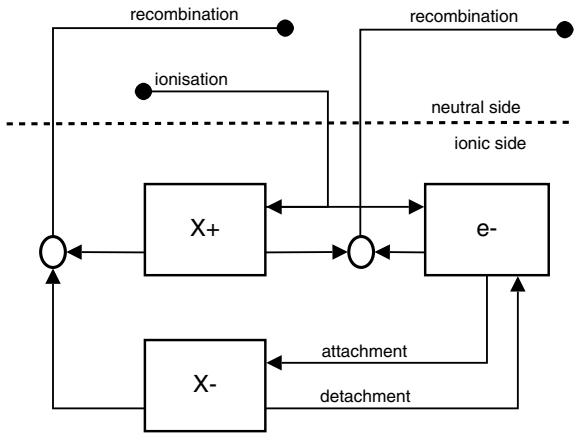

FIGURE 2.1. Schematic view on the charge transfer pathways between electrons and ions. X^+, X^-, e^- indicate positive ions, negative ions, and electrons, respectively.

Most of the balancing reactions depend upon the solar light such that at night the electrons nearly disappear from altitudes below 80 km and negative charge is held largely by the ions.

The production of positive and negative charge by ionisation is balanced by recombination reactions, which result in neutralisation. Fig. 2.1 shows a schematic view on the charge transfer pathways between electrons and ions. In equilibrium, the production Q is equal to the loss

$$Q = \alpha_e \, [\mathrm{X}^+] \, [\mathrm{e}^-] + \alpha_i \, [\mathrm{X}^+] \, [\mathrm{X}^-] \tag{2.3}$$

where $[\mathrm{X}^+]$ and $[\mathrm{X}^-]$ are the sums of concentration of positive and negative ions, respectively, $[\mathrm{e}^-]$ is the electron concentration, and α_e and α_i are the ion-electron and ion-ion recombination coefficients, respectively. The relative magnitudes of the right-hand-side terms of Eq. (2.3) are altitude-dependent, the ion-ion recombination being dominant where negative ions are more abundant than electrons, *i.e.* below about 70 km during daytime and below 80 km at night . Fig. 2.2 shows concentration profiles of electrons, and positive and negative ions for day and night conditions.

As shown in Fig. 1.4 (in Section 1.1), SPEs can significantly increase the ionisation rate in the D region ionosphere above the quiet-time levels. By looking at Fig. 2.1 one could think that while SPEs increase the production of electrons and ions and subsequently elevate their concentrations, the relative amount of different ionic species is not affected. However, although SPE-related changes in temperature and atmospheric transport could also have an effect, there are two main reasons why SPEs can significantly affect also the ion composition.

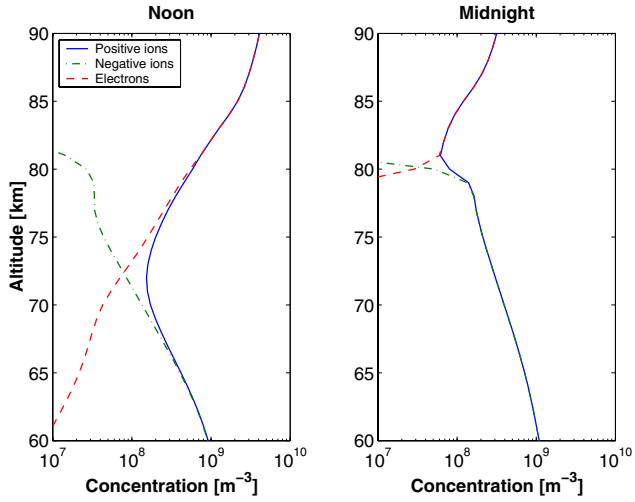

FIGURE 2.2. Altitude profiles of electrons, and positive and negative ions for day and night conditions. SIC model results. Solar EUV/Lyman-α, GCR, and scattered Lyman-α are considered as ionisation sources. Latitude 70°N, equinox. Note the disappearance of electrons below 80 km at night.

Under normal Lyman-α ionisation the main ion in the D-region is NO^+. During SPEs, and particle precipitation in general, the main ion is O_2^+ because the particles ionise mostly the main neutral components N_2 and O_2, and the created N_2^+ is very quickly converted to O_2^+ through the fast reaction

$$N_2^+ + O_2 \rightarrow O_2^+ + N_2. \tag{2.4}$$

As a result, the production of H^+ clusters is favoured over that of NO^+ clusters. There are also implications to the atmospheric effects of SPEs because the production of O_2^+ (instead of NO^+) results in more effective odd hydrogen production through hydrate ion reactions (see Section 2.3.2).

Another way for the SPEs to change the D-region ion composition is through minor neutral constituents. As will be presented in Section 2.3, SPEs produce large amounts of odd nitrogen and odd hydrogen constituents, which due to importance of minor neutral constituents to the D-region ion chemistry, will affect the ion composition. An especially important species in determining the ion composition is nitric oxide, NO. Increase in NO due to SPEs results in more production of NO^+ through Lyman-α ionisation. For negative ions, NO determines the balance between the CO_3^- and NO_3^- ions, higher amounts of NO favouring NO_3^- and its hydrates, which affects, for example, the characteristics of the transition between electrons and ions during twilight [Reid, 1987, Paper IV].

2.3 Changes in minor neutral constituents

In the middle atmosphere, the major constituents are N_2 and O_2. The relative concentrations of these compounds are more or less constant, and they hold ≈78% and ≈21% shares of the total, respectively. The remaining 1% consists of minor gases, mostly argon. Despite their small abundances, minor constituents such as ozone and carbon dioxide play important roles in atmospheric chemistry as well as in heating and cooling processes.

Middle atmospheric gases can be classified as primary or secondary constituents [Shimazaki, 1984, pp. 17–19]. Primaries have their sources near the surface or in the soil of the Earth, and are transported into the middle atmosphere by atmospheric motions. Examples of important primaries are N_2, O_2, H_2O, CO_2, N_2O, and CH_4. Secondaries are produced *in-situ* in the middle atmosphere either by photodissociation of primaries, or by photochemical reactions of secondary molecules with primaries or other secondaries. Important secondaries include, *e.g.*, O, O_3, NO, OH, and Cl, and HNO_3. In addition to the constituents of terrestrial origin, there are constituents that have an extra-terrestrial source. For example, sodium and magnesium are released from meteors in the mesopause region through ablation [Plane et al., 1999].

The concentrations of minor constituents may be affected by SPEs both in the mesosphere and stratosphere. In the following sections of this chapter, the decrease of ozone due to SPEs through enhancement of important minor catalysts OH and NO is described. Changes caused by SPEs have been observed in other minor constituents too [*e.g.* Lopéz-Puertas et al., 2005b; Orsolini et al., 2005], but detailed discussion of those effects is beyond the scope of the present work.

2.3.1 Odd nitrogen enhancement

Main source of odd nitrogen (N + NO + NO_2) in the stratosphere is N_2O which is produced at ground level by both natural and anthropogenic sources [Brasseur and Solomon, 2005, pp. 328–333], and is then transported into the stratosphere where it reacts with excited atomic oxygen to produce NO

$$N_2O + O(^1D) \rightarrow 2NO. \tag{2.5}$$

This process requires solar radiation and is strongest at the equator, where the maximum production of $O(^1D)$ by photodissociation of ozone and molecular oxygen occurs. Significant production of odd nitrogen occurs also at thermospheric heights, maximising around 110 km, where photoionisation by EUV and soft X-ray radiation and subsequent photoelectron impact dissociate N_2, producing atomic nitrogen which then reacts to form NO

$$N_2 + h\nu \;\; \rightarrow \;\; N_2^+ + e^* \tag{2.6}$$

$$e^* + N_2 \rightarrow 2N + e^* \quad (2.7)$$

$$N + O_2 \rightarrow NO + O. \quad (2.8)$$

In the auroral regions, particle precipitation contributes to the production, and is an important source of odd nitrogen. The process is similar to that by EUV/X-ray radiation. The primary particle, a high-energy proton or electron, first ionises N_2, the initial odd nitrogen product being atomic nitrogen mainly through secondary electron impact on N_2 [Porter et al., 1976]. Some production of odd nitrogen results also in dissociative ionisation of N_2 by the primary particle and in ion chemical reactions following the ionisation [*e.g.* Rusch et al., 1981]. The altitude of odd nitrogen production is dependent on the particle energy. High-energy galactic cosmic rays produce odd nitrogen in the lower stratosphere more or less constantly and their annual contribution is comparable to that by reaction (2.5), especially during solar minima [Vitt and Jackman, 1996]. Auroral electron precipitation contributes significantly at altitudes around 110 km and, although having significant time variation in magnitude, this process is constantly present and produces high amounts of odd nitrogen, exceeding the production by EUV, so that at lower thermospheric altitudes the maximum NO is located at auroral latitudes [*e.g.* Barth, 1992].

The main production altitudes of odd nitrogen being in the lower thermosphere and in the stratosphere results in a two-peak altitude profile for odd nitrogen, with a low-production region in between the peaks and a minimum located in the middle mesosphere. In this region, sporadic particle events, such as SPEs or relativistic electron precipitation, can significantly contribute to the odd nitrogen production. Estimated production rate of odd nitrogen varies between $1.2 - 1.6 \times Q$, where Q is the total ionisation rate due to proton precipitation [Rusch et al., 1981]. Typical peak ionisation rates during large SPEs are of the order 10^9–10^{10} m^{-3} s^{-1} in the stratopause region, thus the odd nitrogen amounts produced in relatively short period of time by an SPE are comparable to the normal quiet-time concentrations (10^{12}–10^{15} m^{-3}). Therefore, large SPEs are expected to enhance the odd nitrogen concentration significantly above background levels and order-of-magnitude increases have, indeed, been observed after large SPEs [Zadorozhny et al., 1994; Jackman et al., 2001]. Fig. 2.3 shows modelled NO_x changes caused by the SPE of October 1989.

The odd nitrogen loss in the middle atmosphere is driven by NO photodissociation, followed by reaction with the produced ground state atomic nitrogen

$$NO + h\nu \rightarrow N(^4S) + O \quad (2.9)$$

$$N(^4S) + NO \rightarrow N_2 + O, \quad (2.10)$$

The loss rate is dependent on the level of solar illumination. In sunlit conditions the photochemical lifetime of odd nitrogen is about one day in the upper

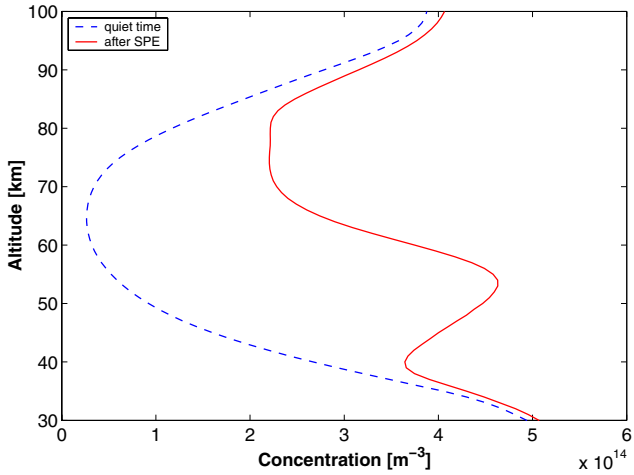

FIGURE 2.3. High-latitude, daytime profile of NO_x before and after the onset of the October 1989 SPE. SIC model results. The increase in NO_x is a result of two days of hard proton precipitation.

mesosphere and lower thermosphere, and from days to months in the stratosphere [Brasseur and Solomon, 2005, pp. 342–344]. In low-illumination conditions the lifetime is of the order of months throughout the middle atmosphere. Therefore, transport is important for the altitude and latitude distribution of odd nitrogen. This is especially true for the polar latitudes during winter time, and significant amounts of odd nitrogen can be transported from the upper mesosphere and lower thermosphere down to stratospheric altitudes [Siskind et al., 1997; Callis and Lambeth, 1998]. Also, the meridional transport from high-production equator to high latitudes can be important in the stratosphere. Although odd nitrogen has a relatively long photochemical lifetime, there is a strong diurnal variation between NO and NO_2. During daytime a photochemical equilibrium exists, but at night NO concentration is reduced by several orders of magnitude as, in the absence of solar light, it is rapidly converted to NO_2 at altitudes below about 60 km.

2.3.2 Odd hydrogen enhancement

Stratospheric and lower mesospheric odd hydrogen ($H + OH + HO_2$) is produced from water vapour in a reaction with excited atomic oxygen

$$H_2O + O(^1D) \rightarrow 2OH, \tag{2.11}$$

while in the upper mesosphere and thermosphere the main source is photodissociation of H_2O

$$H_2O + h\nu \rightarrow OH + H, \tag{2.12}$$

especially by Lyman-α radiation. Both of these reactions depend upon solar radiation, because $O(^1D)$ required in reaction (2.11) is produced by photodissociation. Odd hydrogen loss is due to reactions involving two odd hydrogen species, such as

$$OH + HO_2 \rightarrow H_2O + O_2, \tag{2.13}$$

and its photochemical lifetime is of the order of hours at altitudes below 80 km. Therefore, its density does not directly depend upon transport processes in the lower mesosphere and stratosphere [Brasseur and Solomon, 2005, pp. 321–325]. The short chemical lifetime results in a strong diurnal variation with several orders of magnitude lower concentrations at nighttime due to reduction in production by reactions (2.11) and (2.12).

Particle precipitation produces odd hydrogen, but this process is considerably more complex than the production of odd nitrogen, which is mostly due to direct impact of primary particles and secondary electrons on N_2. Odd hydrogen production involves two special features of the ionospheric D region, water cluster ions and negative ions, which must be combined for a full description of the process. It is dependent not only on the ionisation rate but also on the changes in minor neutral constituents during the particle forcing [Solomon et al., 1981]. The basic process is as follows. Ionisation results in a set of initial ions, including O_2^+, leading to formation of its hydrate $O_2^+(H_2O)$ via O_4^+. There are then a number of reaction pathways, with increasing degree of hydration and eventual recombination with an electron, as a result of which one water molecule can be converted into two odd hydrogen species, OH and H. These pathways are effective only at altitudes below 80 km, where water cluster ions can be formed, and can be interrupted by recombination of the intermediate ions, so that the production of odd hydrogen will vary with altitude. Also, at the lower altitudes where negative ions are more abundant than free electrons, the positive ions favour negative ions in recombination, resulting in production of HNO_3. Although a large part of the produced HNO_3 is photodissociated to produce OH, thus adding to odd hydrogen production, this pathway is not operative during nighttime and at daytime there is a delay in the odd hydrogen production due to photolysis lifetime of HNO_3 being of the order of hours. Similar pathways starting from the NO^+ ion exist. However, these are considered to be of lesser importance because the primary ion produced by particle precipitation is O_2^+.

Theoretically, during an SPE the maximum production efficiency of odd hydrogen is two molecules per each ion pair. Typical peak ionisation rates during large SPEs are more or less equal to the daytime production rate of odd hydrogen from water vapour. However, on average the ionisation rate is an order of magnitude lower. As a result, odd hydrogen concentration is significantly enhanced during night as well as during sunrise and sunset, when the background production from water vapour is relatively low, and during daytime only if very high

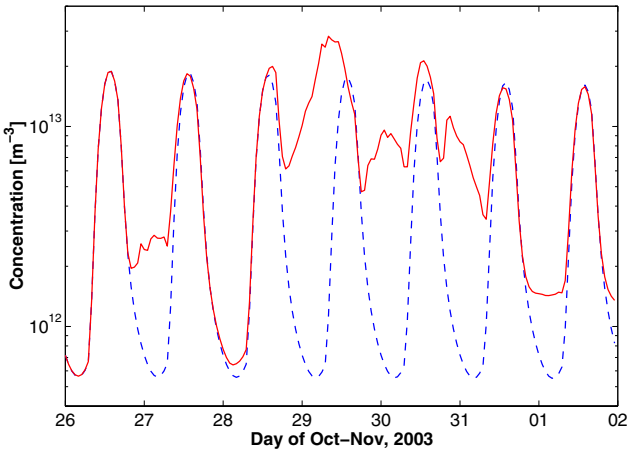

FIGURE 2.4. Diurnal variation in HO_x concentration at 72 km altitude in quiet conditions (blue dashed line) and during the October-November 2003 SPE (red solid line). SIC model results. Latitude 70°N.

ionisation rates occur. During an SPE, the efficiency of odd hydrogen production varies somewhat, reflecting the SPE-induced changes in the minor neutral constituents [Solomon et al., 1981]. Fig. 2.4 shows modelled SPE effects on the HO_x diurnal cycle during the SPE of October/November 2003.

To date, direct measurements of odd hydrogen changes during an SPE have not been available. Indirect measurements, *i.e.* of ozone, exist but the validation of odd hydrogen production theory would greatly benefit of measurements of OH and/or HO_2. Model estimates have predicted order-of-magnitude changes in odd hydrogen concentration during intense SPE forcing. Such changes should be relatively easy to confirm by measurements.

2.3.3 Ozone depletion

Middle atmospheric odd oxygen ($O_x = O + O_3$) chemistry is driven by solar radiation through photodissociation of molecular oxygen, which produces atomic oxygen

$$O_2 + h\nu \rightarrow O + O. \tag{2.14}$$

The pure oxygen chemistry has three significant reactions directly involving ozone:

$$O + O_2 + M \rightarrow O_3 + M \tag{2.15}$$

$$O_3 + h\nu \rightarrow O_2 + O \tag{2.16}$$

$$O + O_3 \rightarrow 2O_2 \tag{2.17}$$

Of these, (2.15) is the source of ozone in the atmosphere, and maintains the balance between ozone and atomic oxygen together with (2.16), while (2.17) results in loss of odd oxygen. Another loss reaction of odd oxygen,

$$\mathrm{O} + \mathrm{O} + \mathrm{M} \rightarrow \mathrm{O_2} + \mathrm{M}, \tag{2.18}$$

is generally much slower than (2.17) but increases in importance above the mesopause. These reactions constitute the basic scheme of pure oxygen chemistry proposed in the 1930s [Chapman, 1930].

After the first measurements of middle atmospheric ozone were obtained, it was evident that concentrations predicted by pure oxygen chemistry were considerably higher than those observed. It had been noted by Bates and Nicolet [1950] that catalytic reaction cycles such as

$$\mathrm{XO} + \mathrm{O} \rightarrow \mathrm{X} + \mathrm{O_2} \tag{2.19}$$

$$\mathrm{X} + \mathrm{O_3} \rightarrow \mathrm{XO} + \mathrm{O_2} \tag{2.20}$$

are very important in the atmosphere, and for ozone and odd oxygen in general they constitute the main loss processes. The catalyst X can be either Br, Cl, NO, or OH radical, and the relative importance of these constituents to ozone varies with atmospheric altitude. Generally, in the mesosphere the most important catalyst is OH, in the upper and middle stratosphere it is NO and Cl, respectively, while Br and OH are important in the lower stratosphere [*e.g.* Brasseur and Solomon, 2005, pp. 444–445]. In reality the situation is much more complex in the stratosphere, where more than ten catalytic cycles involving different catalyst have been identified and the altitude domains of the cycles overlap [*e.g.* Lary, 1997]. Most of the ozone is within the so-called ozone layer, which is located in the stratosphere between altitudes of 15 and 35 km. The ozone layer is a result of ozone production being dependent on the photodissociation coefficient of $\mathrm{O_2}$ and atmospheric density, the former increasing with height and the latter decreasing, such that the product of these has a maximum in the lower stratosphere. Another distinctive feature of the ozone concentration profile is the secondary maximum located in the mesopause region around 90 km, caused by the decrease of water vapour above 80 km due to Lyman-α dissociation diminishing the OH catalytic cycle and thus decreasing ozone loss [Allen et al., 1984]. The secondary maximum can be further enhanced by the transport of atomic oxygen from the thermosphere. Fig. 2.5 shows an annual average ozone distribution from satellite measurements.

Ozone has a strong diurnal variation in the upper stratosphere and mesosphere [see Allen et al., 1984, for detailed discussion], where its concentration is more or less comparable to that of atomic oxygen. The ozone values are higher at night because the absence of photodissociation, *i.e.* reaction (2.16), results in conversion of atomic oxygen to ozone through reaction (2.15). The sunrise/sunset transitions of both $\mathrm{O_3}$ and O are sharp, and around the 80 km ozone minimum

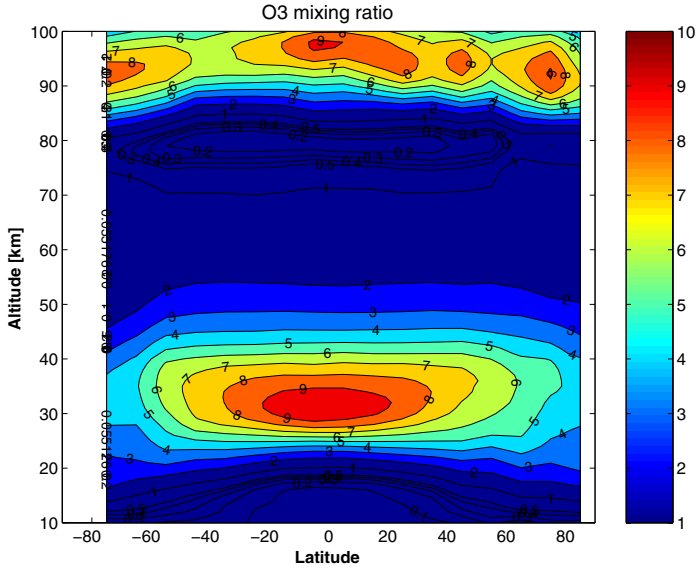

FIGURE 2.5. Annual average, night-time ozone distribution from measurements of the GOMOS instrument during 2003 (courtesy of E. Kyrölä, Finnish Meteorological Institute). Note the two distinctive maxima in mixing ratio (shown in ppmv units) at about 30 and 95 km, as well as the minimum at about 80 km.

the concentrations show significant temporal variation during daytime [*e.g.* Shimazaki, 1984, pp. 162–168].

In the lower stratosphere, the photochemical lifetime of ozone is relatively long. Therefore, in addition to photochemical production and loss, atmospheric transport can play an important role in determining its distribution. A manifestation of this is seen in observations of total ozone column that have shown the highest column densities at high latitudes, although the ozone production is strongest at the equator [Brasseur and Solomon, 2005, pp. 281–288].

As already discussed in Sections 2.3.1 and 2.3.2, significant production of odd nitrogen ($N + NO + NO_2 = NO_x$) and odd hydrogen ($H + OH + HO_2 = HO_x$) species occurs in the middle atmosphere during large SPEs. This can lead to depletion of ozone through enhancement of the catalytic reactions cycles involving NO_x and HO_x. As mentioned above, the HO_x cycles are most effective in the mesosphere, while NO_x cycles have their largest influence on ozone in the middle and upper stratosphere. Therefore, the ozone changes due the enhancement of NO_x and HO_x are generally seen at different altitudes, although there is overlap in the stratopause region. Most of the ozone-destroying catalytic NO_x and HO_x cycles involve atomic oxygen, which at altitudes below ∼80 km is available only

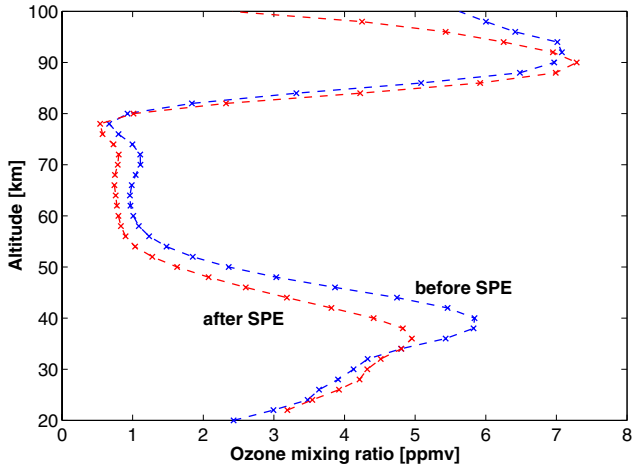

FIGURE 2.6. Ozone depletion due to the October-November 2003 SPE, as observed by the GOMOS instrument. The profiles are zonal averages for latitudes 70°N–75°N. The before-SPE and after-SPE profiles include night-time measurements from October 18–24 and November 3–6, respectively.

in sunlit conditions. As a result, ozone depletion requires solar radiation and is moderate at night-time. Largest depletions are seen during sunrise and sunset, when atomic oxygen is available and the background production of HO_x from water vapour is relatively low [*e.g.* Paper II].

The effect of HO_x increase on ozone is of relative short duration. The HO_x photochemical lifetime being short and ozone production in sunlit conditions being relatively fast result in a quick recovery of both species after a reduction in the flux of precipitating solar protons. On the other hand, NO_x can have a long photochemical lifetime, especially in conditions of low level of illumination, and the ozone decrease due to enhanced NO_x can last for months. In such time scales, the atmospheric transport of NO_x plays an important role in determining the ozone changes in the stratosphere. The ozone changes caused by an SPE typically occur above the ozone layer, thus the total column ozone is not significantly reduced. Instead, there is indication that if the SPE-produced NO_x is transported to lower stratosphere, it may interfere with the Cl and Br catalytic cycles below ∼22 km resulting in a slight increase of ozone in the lower stratosphere [Jackman et al., 2000]. Nevertheless, ozone reduction by tens of percent has been observed during and after large SPEs in both the mesosphere and upper stratosphere [*e.g.* Paper I]. Fig. 2.6 shows ozone profiles measured in the northern polar region before and after a large SPE.

Depletion of ozone results in temperature decrease in the middle atmosphere through reduction in the absorption of UV radiation. On the other hand, Joule

heating (in electron/ion/neutral collisions due to different velocities) during proton precipitation could increase the temperature in the mesosphere temporarily. These opposite effects have been estimated to change the temperature by about -3 K and $+10$ K, respectively, and could play a role in SPE-related wind changes [Jackman and McPeters, 2004, and references therein]. Rocket measurements during the October 1989 SPE have indicated a temperature decrease by -14 K in the stratopause region, which exceeds the theoretical estimations [Zadorozhny et al., 1994].

2.3.4 About the role of middle atmospheric dynamics

Due to continuous input of heat and momentum, the middle atmosphere does not reach an equilibrium state but is always in motion. The latitudinal temperature gradients drive zonal winds, which are strongly influenced by the seasonal variation in solar heating [Brasseur and Solomon, 2005, pp. 55–57]. The strong zonal advection effectively mixes the atmospheric species, so that in the longitudinal direction the variations of atmospheric quantities are relatively small when contrasted to variations with respect to altitude and latitude. In the meridional direction, the mean Brewer-Dobson circulation is characterised by upwelling in the summer hemisphere, meridional transport from summer to winter hemisphere in the mesosphere, and downwelling in the winter hemisphere. The primary cause of the mean meridional circulation is believed to be gravity waves, which originate from the ground level and dissipate in the stratosphere and mesosphere [Smith, 2004]. The momentum deposition by breaking waves together with the Coriolis effect forces the summer to winter flow, which then by continuity results in an ascending flow in the summer hemisphere and descending flow in the winter hemisphere. Wave breaking leads also to vertical mixing of heat and constituents by turbulent diffusion. In the stratosphere the mean circulation is driven more from equator to pole by breaking planetary waves, and it is strongest in the winter hemisphere.

In the winter polar stratosphere, strong westerly zonal winds, also know as polar night jets, form the so-called polar vortex [Brasseur and Solomon, 2005, pp. 108–109]. Located at latitude $\approx 60^\circ$ and above 16 km in altitude, it acts as an dynamical barrier and tends to isolate the polar cap region. The vortex can be disturbed by planetary-scale waves through deceleration of the zonal flow. As planetary waves are in general less intense in the Antarctic, the polar vortex is more stable there than in the Arctic. Strong waves may reverse the direction of polar jets and cause the breakdown of polar vortex, which leads to a strong downward motion and sudden stratospheric warming through adiabatic compression.

The long-term effects of SPEs on odd nitrogen and ozone are influenced by atmospheric dynamics of the polar regions, which is strongly dependent on the sea-

son [*e.g* Jackman et al., 1995]. In the summer pole the mean circulation transports constituents towards higher altitudes, which tends to prevent the large amounts of NO_x, produced at higher altitudes, from entering the upper stratosphere where catalytic ozone destruction by NO_x is most efficient. In the winter pole the situation is the opposite. It has been suggested for some time that significant amounts of NO_x, produced by energetic particle precipitation, may be transported into the stratosphere from the mesosphere and thermosphere inside the polar vortex [Solomon et al., 1982]. Observations of NO_2 and ozone from the GOMOS instruments showed that descent of NO_x and corresponding depletion of ozone occurred after the October/November 2003 SPE, until the breakup of the polar vortex in late December [Paper I]. Although there are also observations of such NO_x descent after electron precipitation events, the scarcity of the data has not allowed for strong conclusions on the importance of particle precipitation to stratospheric ozone in general [Callis, 2001].

3 Observations of SPE effects

In general, middle atmosphere and the D-region ionosphere are observed by either *in-situ* (local) or remote sensing methods. Stratospheric altitudes can be reached with balloons while mesospheric and D-region *in-situ* observations require rocket-borne instruments. A variety of both ionospheric and atmospheric quantities can be retrieved from *in-situ* measurements, including gas concentrations, winds, temperature etc. Of special importance have been rocket observations of D-region ion composition, which has not been measured directly by remote sensing. The disadvantage of *in-situ* observations is that they are momentary in the nature, thus providing data with rather limited spatial and temporal coverage.

Remote sensing (RS) is dominantly ground-based or satellite activity, although RS instruments have also been flown with balloons, aircrafts, and rockets. RS instruments measure electromagnetic radiation or sonic waves that have traversed the medium of interest, *i.e.* the atmosphere. The target quantity is not measured directly but has to be inverted from the modifications of observed signal caused by the medium, which may require detailed modelling of the signal propagation and *a priori* information about the medium. The signal itself can be natural, such as solar radiation, or it can be generated. RS data is generally good in temporal continuity, and the satellite measurements tend to have good global coverage.

This chapter briefly outlines measurements of both ionospheric and neutral atmospheric quantities that can be used to detect SPE-induced perturbations in the middle atmosphere. Special attention is given to instruments and measurements used in papers I–V. Section 3.2.1 is devoted to the GOMOS instrument, which has provided most important new data for this thesis work.

3.1 Monitors of ionospheric disturbances

Ionospheric disturbances during solar proton events have been observed almost solely by radio techniques, especially by riometers and incoherent scatter radars (see section 1.1.2). Depending upon the frequency, changes in the D-region electron density induce changes in the ionospheric reflectivity or absorption of the observed signal. As such, these measurements are used to monitor the basic ionospheric parameters, *i.e.* ionisation rate and electron density. Details on the ion composition can be obtained only by using appropriate ion chemistry models.

3.1.1 VLF radio signal receivers

Very Low Frequency (3–30 kHz), VLF, (long-wave) radio signals are used in communication systems, *e.g.* between ground stations and submarines. The signals used in communication systems are generated by high power transmitters but VLF signals can also be generated by natural processes such as lightning. Over distances greater than a few hundred kilometres, subionospheric VLF signal propagation can be treated theoretically in terms of a waveguide formed by the Earth's surface and the bottom of the Earth's ionosphere located between 50 and 100 km [Barr et al., 2000]. Therefore, changes in the lower ionosphere produce changes in the received amplitude and phase of the VLF signals.

The signals coming from distant transmitters, which are rather well distributed in geographic location, can be monitored by VLF receivers set up in different locations around the Earth. The amplitude and phase of the transmitted signal observed at the receiver location can also be modelled by considering the variation of geophysical parameters along the signal path [Clilverd et al., 2005b]. An important variable input in the calculations is the electron density profile which defines the upper boundary conditions for the waveguide. Comparisons of observed and modelled signal can be used to study lower ionospheric changes, which are know to be severe during SPEs. VLF measurements are used in Paper II.

3.1.2 Riometers

Riometers measure ionospheric absorption of cosmic radio noise, typically at frequencies of 20–60 MHz. Cosmic radio noise is of galactic origin and is considered to be constant over long periods of time, so that any changes in the signal observed on the ground are due to changes in ionospheric absorption. The absorption depends upon electron-neutral collision frequency, which, in turn, depends upon electron density and temperature. Typically, most of the absorption occurs in D-region altitudes, *i.e.* below 95 km. Riometers are relatively cheap, easy to operate, and can continuously measure the integrated ionisation levels of the overhead ionosphere. Interpretation of measurements includes determination of a quiet-day curve, which is then subtracted from measurements, so that the final absorption data by riometers are relative in nature. A riometer setup consists of a single wide-beam antenna, or an array of antennas which can be used to construct narrow beams. The latter setup is called an imaging riometer because it can provide a 2-D picture of the absorption, typically over 100×100 km area at 90 km altitude. For a description of riometer technique and measurements, see, *e.g.*, Ranta et al. [1983] or Detrick and Rosenberg [1990].

Cosmic radio noise absorption can also be estimated from electron densities

by calculating the electron collision frequencies of the main neutral atmospheric species using electron temperature [Banks and Kockarts, 1973, Part A, p. 194]. The Appleton-Hartree magnetoionic theory [*e.g.* Sen and Wyller, 1960] can then be used to compute differential absorption dL/dh. Height integration of the differential absorption then provides a quantity equivalent to the one observed by riometers. The absorption is significantly increased by SPE-induced ionisation in the D-region, the daytime riometer observations typically showing ∼10 dB values during a large event. Riometer measurements are used in Papers IV and V.

3.1.3 Incoherent scatter radars

Incoherent scatter (IS) radars provide altitude profiles of ionospheric quantities, such as electron density and temperature. The technique includes transmitting a coded power pulse, which is then scattered in the ionosphere by electrons, so that the returned power can be measured. The advantage of IS radars is that they are able to provide data from above as well as below the peak electron density with good spatial resolution [Hargreaves, 1992, pp. 81–88]. On the other hand, the scattered signal is very weak, so that a powerful transmitter and a sensitive receiver are required. Several experiment modes have been developed for the radars operated at VHF and UHF frequencies [*e.g.* Collis and Rietveld, 1990, and references therein], with specific purposes and altitude coverage. The radars are not operated continuously, but can provide a rather comprehensive set of ionospheric data with a ∼10 s temporal resolution.

The quiet-time electron densities in the lower D region, below ∼70 km, are of the order of 10^8 m^{-3} or less [*e.g.*, Hargreaves, 1992, pp. 231]. For this kind of small values the EISCAT signal-to-noise ratio is very low, making measurements impractical [Turunen, 1993]. However, during SPEs the D-region ionisation levels can be drastically elevated, allowing observations reaching stratopause altitudes. Incoherent scatter radar measurements are used in Paper IV.

3.2 Measurements of perturbations of minor neutral species

SPE-induced changes in minor neutral constituents have been occasionally observed by rocket measurements [Weeks et al., 1972; Zadorozhny et al., 1994], while the bulk of measurements has come from satellites (see section 1.1.2). However, night-time measurements have been lacking until quite recently. Important new data has been obtained from the GOMOS/Envisat instrument. The GOMOS observations of ozone and NO_2 are used in Papers I and II, while Paper III presents a validation of these rather unique night-time ozone data.

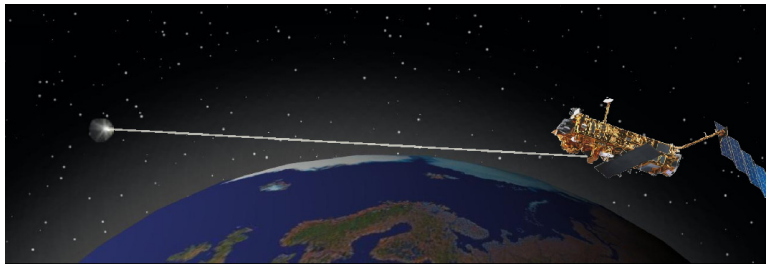

FIGURE 3.1. An artistic view on GOMOS making a stellar occultation above Finland (courtesy of VTT).

3.2.1 GOMOS instrument on board Envisat satellite

GOMOS (Global Ozone Monitoring by Occultation of Stars) is a UV-VIS spectrometer on board the European Space Agency's (ESA) Envisat satellite [Bertaux et al., 1991, 2004; Kyrölä et al., 2004]. GOMOS was designed for observations of middle atmospheric ozone and other species related to the ozone chemistry. Altitude profiles of gases can be inverted from GOMOS measurements that use the stellar occultation technique. In this technique, the instrument is pointed at a star and the stellar spectrum is measured, first when the line-of-sight (LOS) is above the atmosphere (tangent altitude ≈150 km). As the satellite advances in its orbit, the star seems to set behind the atmosphere and, while the instrument continuously measures the spectrum, LOS descends in altitude until it is eventually interrupted by the solid Earth if not the clouds. One such star tracking from the top of atmosphere down to the ground during which the stellar signal is obscured by the atmosphere is called an occultation. Fig. 3.1 displays an artistic view on GOMOS making a stellar occultation.

The advantages of stellar occultation technique are that 1) both daytime and night-time observations can be made because the measurements are not dependent on solar light, 2) the global coverage of observations is good because stars are distributed all around the sky, 3) the altitude resolution, which is dependent on the measurement geometry, is always better than 1.7 km, and 4) the measurements are self-calibrating because the reference spectrum of the star is recorded for each occultation. A disadvantage is that the accuracy of measurements depends on the stellar temperature and magnitude, and is thus different for each of the stars used. Also, some of the daytime measurements have a low signal-to-noise ratio due to scattered solar radiation entering the instrument.

The basic output from GOMOS is the transmission of light through the atmosphere for each tangent altitude, defined as I_{occ}/I_{ref}, where I_{occ} and I_{ref} are the intensities measured through and above the atmosphere, respectively. Knowing

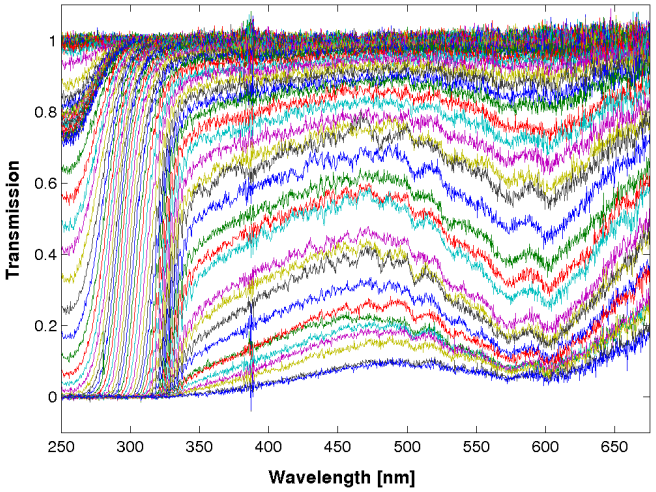

FIGURE 3.2. Level 1 transmissions at UV-VIS wavelengths measured by GOMOS during one occultation (courtesy of E. Kyrölä, Finnish Meteorological Institute). First, when the line-of-sight (LOS) is above the atmosphere, transmission is 1. But as LOS descends in altitude, the atmospheric gases absorb more and more of the initial radiation, so that for lower altitudes the transmission has decreased significantly. Different gases absorb at different wavelengths. For example, the absorption at the smaller wavelengths (< 350 nm) is mostly due to ozone in the mesosphere.

the wavelength-dependent absorption cross sections of the different atmospheric gases, their altitude profiles can be calculated from the transmission data using the Beer-Lambert absorption law and advanced inversion methods [Kyrölä et al., 1993]. Fig. 3.2 shows transmissions measured by GOMOS during one occultation.

The spectral range of GOMOS, 250–675 nm and two infrared channels, allows for inversion of several gas concentration profiles, including ozone and NO_2. Fig. 3.3 presents the altitude ranges of some of the unknown atmospheric quantities retrieved from GOMOS measurements. Note especially the extended altitude range of ozone measurements, from 5 to 100 km. Global measurements of atmospheric quantities have been made by the GOMOS instrument since the launch of the Envisat satellite in March, 2002. GOMOS successfully performs several hundred occultations per day with good global coverage, including the polar areas.

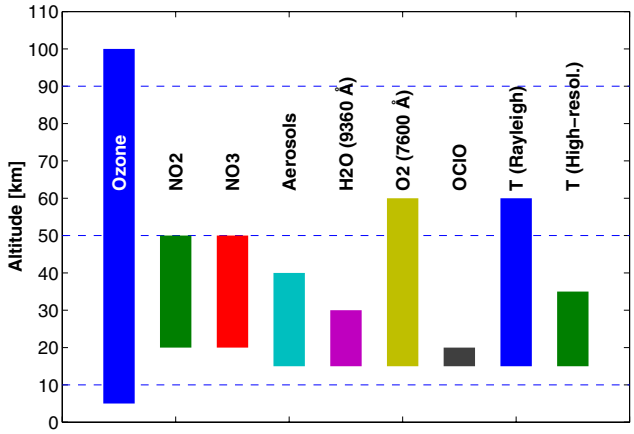

FIGURE 3.3. The altitude ranges of some of the unknown atmospheric quantities retrieved from GOMOS measurements. Most of the information obtained is for stratospheric heights but for ozone the altitude range is quite extensive, from 5 to 100 km in optimal conditions.

4 SIC: a 1-D ion and neutral chemistry model

Modelling is an important part of atmospheric research. Many times, measurements provide an indirect or partial view on the atmospheric properties and processes with a limited geographical and/or altitude coverage. Interpretation of such observations can be greatly improved by using suitable atmospheric models, leading to a better understanding of atmospheric processes. On the other hand, model results may provide important extra information, which can be used to guide the planning of future observations and laboratory work. Unlike measurements, modelling can provide a quite comprehensive representation of the atmosphere. However, no model is perfect. Not all processes of the atmosphere are well understood, some likely not even known of, and simplifying assumptions have to be made because the processes are many, their interactions are complex, and computing time is limited. Therefore, validation of model results using measurements is vital. Results based purely on modelling should be taken with appropriate extra caution.

In this chapter, a one-dimensional photochemical model of the lower ionosphere and middle atmosphere, the Sodankylä Ion Chemistry model, is presented. The following sections will outline the model inputs and outputs, describe the photochemical schemes included and how the model is used to study ionospheric and atmospheric effects of SPEs, and discuss its uncertainties, limitations, and applicability as well as future prospects.

4.1 Historical background

The Sodankylä Ion Chemistry model, also known as SIC, was developed in the late 1980s in the Sodankylä Geophysical Observatory by E. Turunen, H. Matveinen, and H. Ranta, after some original work by M. Dymek in the 1970s. A detailed chemical scheme, in a conceptually simple model, was built to be a tool for interpretation of D-region ionospheric observations. Originally, the model was designed for geophysically quiet conditions and it solved the concentrations of 35 ionic species, 24 positive and 11 negative, in sunlit conditions. The altitude range was from 70 to 100 km. The solar radiation (5–135 nm) and galactic cosmic radiation (GCR) were considered as ionisation sources acting on five primary neutral components. Photoequilibrium was assumed for all ions and thus transport effects were neglected. Neutral background atmosphere was taken to be constant and not affected by the ion chemistry. The model was first applied by Burns et al. [1991] in interpretation of incoherent scatter radar observations. A more detailed description of the original SIC is given by Turunen et al. [1996]. In due course, the model was extended to include electron and proton precipitation as ionisation

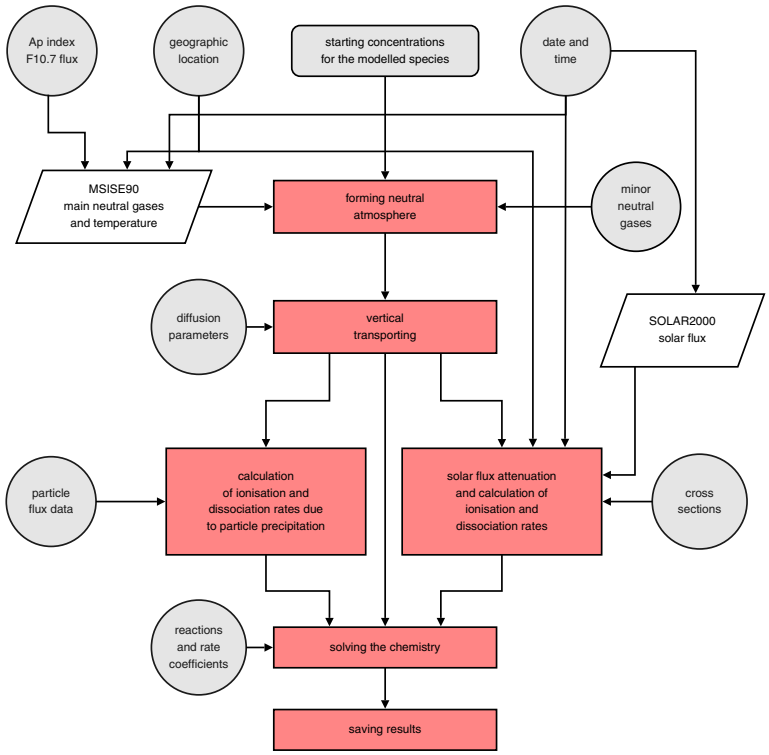

FIGURE 4.1. Schematic structure of the Sodankylä Ion Chemistry model. The circles, tilted squares, and squares indicate external input, external models used, and modules of the SIC model, respectively.

sources, the lower limit of altitude range was lowered from 70 to 50 km, and 20 new ionic species were included.

In the late 1990s a new phase in SIC development began. The model was converted into a 1-D coupled ion and neutral chemistry tool, with intentions to study effects of solar proton events on the neutral minor constituents, together with satellite measurements. The approach taken was to combine the quite detailed ion chemistry scheme with a basic set of neutral reactions of the upper stratosphere and mesosphere. Currently, the model solves the time-dependent concentrations of 79 constituents (36 positive ions, 28 negative ions, and 15 neutral species) at altitudes from 20 to 150 km, with 1 km resolution. The modelled species are listed in the Appendix. Fig. 4.1 presents a schematic view on the structure of the SIC model, some details of which are given in the following sections of this chapter.

4.2 Basic external input

4.2.1 Photoionisation and dissociation rates

The solar flux above the atmosphere $I_\infty(\lambda)$ is estimated by the SOLAR2000 model [Tobiska et al., 2000], which provides various daily 1 AU adjusted (or observed) solar irradiance products and historical data. SIC utilises a partial solar spectrum in 1 nm wavelength bins ($\lambda = 1$–423 nm), 39 individual EUV lines and wavelength groups in the EUV91/EUV97 format between 1.86–105.0 nm, and the Lyman-α line. This spectral range of solar radiation is responsible for the main photoionisation and photodissociation processes in the upper stratosphere, mesosphere, and lower thermosphere [Brasseur and Solomon, 2005]. The scattered component of the solar Lyman-α flux, which is an important source of ionisation in the mesosphere at night, is included using the empirical approximation given by Thomas and Bowman [1986].

At each altitude z_o, solar flux values I are determined for each wavelength λ using the well-known Beer-Lambert law

$$I(\lambda, z_o, \chi) = I_\infty(\lambda)\ e^{-\tau(\lambda, z_o, \chi)}, \tag{4.1}$$

where τ is the optical depth of the atmosphere depending upon the solar zenith angle χ and the above atmospheric composition. For the overhead sun ($\chi = 0$)

$$\tau(\lambda, z_o) = \sum_j \sigma_j(\lambda) \int_{z_o}^{\infty} n_j(z)\ dz, \tag{4.2}$$

where σ_j and n_j are the absorption cross section and concentration of atmospheric constituent j. Especially for a large χ, it is necessary to take into account the spherical geometry of the atmosphere, which makes Eq. (4.2) somewhat more complex. Without going into details here, we refer to Rees [1989, p. 12–13], who gives a procedure for optical depth calculation that we have adopted [description is also given by Turunen et al., 1996]. Photoionisation and photodissociation rates can then be calculated for each constituent at each altitude from

$$Q_j(z_o, \chi) = \int_\lambda I(\lambda, z_o, \chi)\ \eta_j(\lambda)\ \sigma_j(\lambda)\ n_j(z_o)\ d\lambda, \tag{4.3}$$

where η_j is the efficiency for ionisation/dissociation. A list of the SIC photoionisation and photodissociation processes and their products is given in the Appendix. Rates for most of these can be calculated according to Eq. (4.3). However, predissociation of NO, *i.e.* excitation by a photon followed by de-excitation and simultaneous dissociation, occurs at wavelengths less than about 191 nm, thus overlapping with the highly structured O_2 Schumann-Runge bands, so that accurate calculation of NO photodissociation requires a different approach [Brasseur

and Solomon, 2005, pp. 233–236]. We use a method that calculates NO photodissociation rate taking into account the slant columns of O_2 and NO, absorption by ozone in the Hartley band (242-310 nm), and the predissociation probability of NO from excited electronic state [Minschwaner and Siskind, 1993].

The sources of absorption cross sections and photoionisation/dissociation efficiencies are listed in the Appendix. In the O_2 Schumann-Runge bands (175–205 nm) the absorption lines show considerable structure and cross section varies by about 5 orders of magnitude, so that a more detailed consideration is required. Therefore, O_2 cross sections for the Schumann-Runge bands are calculated using a parameterisation, which depends on the line-of-sight column density of O_2 and local temperature [Murtagh, 1988; Koppers and Murtagh, 1996].

The primary ionisation by a photon creates an ion and a photoelectron. For the ionisation to occur, the incident photon must provide an amount of energy that is equal or exceeds the threshold ionisation energy of the neutral molecule (or atom) E_i. When more energy is provided than is needed for ionisation, the left-over energy E_s is

$$E_s = h\nu - E_i. \tag{4.4}$$

The excess energy E_s can lead to excitation of the ion. However, in practice a large part of E_s is converted to kinetic energy of the ionisation products, especially to that of the light electron [Rees, 1989]. For photon wavelengths less than about 35 nm, E_s is sufficiently high so that the created photoelectrons are capable of further ionisation, and can considerably increase the N_2 ionisation rate. To take the effect of photoelectrons into account, we utilise a simple parameterisation where the ionisation rate of N_2 due to photoelectrons Q^{pe} is proportional to that due to photons Q according to

$$Q^{pe}(z_o) = C(z_o)\ Q(z_o), \tag{4.5}$$

where C is an altitude-dependent constant set by detailed photoelectron model calculations [Fuller-Rowell, 1993, and references therein]. Fig. 4.2 shows some calculated ionisation rates due to photons and photoelectrons.

4.2.2 Neutral background atmosphere and temperature

By default, the background neutral atmosphere is generated using the semi-empirical MSISE-90 model [Hedin, 1991] and tables given by Shimazaki [1984]. However, any other source, including observational data, could readily be used. MSISE-90 provides climatological average altitude profiles (0–300 km) of N_2, O_2, Ar, He, and temperature with 1 km resolution for any given set of date, time, geographic location, planetary magnetic index A_p, and solar F10.7 flux. Shimazaki [1984] provides mid-latitude concentrations of N_2O, H_2, HNO_2, HCl, Cl, ClO,

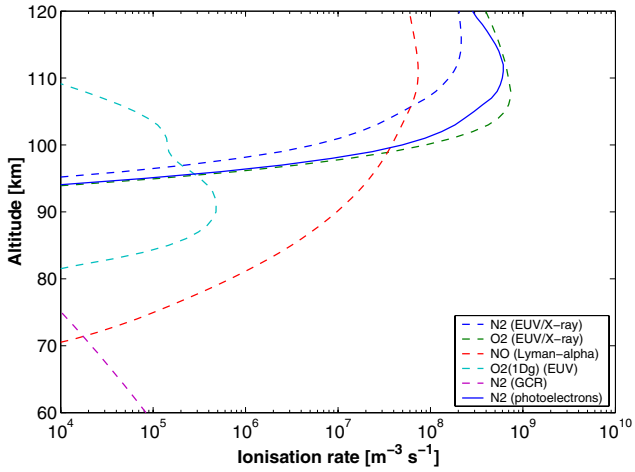

FIGURE 4.2. Daytime ionisation rates due to solar photons, photoelectrons, and GCR (solar maximum). SIC model results. Equinox, latitude 70°N, SZA = 69.6°. Note the photoelectron contribution to the N_2 ionisation rate.

CH_3, CH_4, CH_2O, and CO for noon and midnight conditions at altitudes 10, 15, 20, 25, 30, 45, 60, 80, and 100 km, which we then convert into altitude profiles of 1 km resolution by interpolation. For most of the Shimazaki-based background constituents there is no significant diurnal variation in the middle atmosphere. For those that do have diurnal variation, *e.g.* Cl and ClO, scaling with respect to solar flux level is applied. This allows for a crude approximation of twilight transition of these constituents from day to night concentrations and vice versa. The scaling factor is obtained by dividing the total flux between 99 and 422.5 nm by that pre-calculated for the same altitude and solar zenith angle of 45°. The total concentration is the sum of all individual constituents, and those of H_2O and CO_2 are calculated using fixed volume mixing ratio profiles, the default values are 5 ppmv (below 80 km) and 335 ppmv, respectively. This background atmosphere is then combined with the modelled neutral concentrations, providing a complete set of gases required by the model. For solar zenith angles greater than 90°, the optical depth calculation requires gas concentrations below the lower altitude limit of the model. These are currently taken from Brasseur and Solomon [1986] when not provided by the MSISE-90 model or Shimazaki [1984].

4.3 CHEMISTRY AND TRANSPORT

Concentrations of atmospheric gases are controlled by geochemical and biological processes at ground level, energy input by solar radiation and energetic parti-

cle precipitation, and chemical reactions and atmospheric transport. These concentrations may vary substantially with respect to altitude, geographic location, season, and time of day. Providing that the relevant processes are known, time-dependent concentration of an atmospheric species j can be solved from the continuity equation

$$\frac{\partial n_j}{\partial t} = P_j - L_j n_j - \nabla \cdot (n_j \bar{v}_j) \tag{4.6}$$

where n_j = concentration, t = time, P_j = local production rate, $L_j n_j$ = local loss rate, and $\bar{v}_j$ = velocity. Here, divergence of flux $\nabla \cdot (n_j \bar{v}_j)$ represents the atmospheric transport. P_j and $L_j n_j$ are sums of production and loss rates due to local processes, *i.e.*, photochemical reactions. For a two-body reaction

$$\mathrm{A} + \mathrm{B} \rightarrow \mathrm{C} + \mathrm{D} \tag{4.7}$$

the reaction rate R is obtained from

$$R = k[\mathrm{A}][\mathrm{B}], \tag{4.8}$$

where k is the reaction rate coefficient for this particular reaction, while [A] and [B] are the concentrations of constituents A and B, respectively. Reaction rate coefficients, which are in many cases temperature-dependent, are generally obtained from laboratory measurements because interactions between reacting gases are multidimensional and thus quite complex to model [Brasseur and Solomon, 2005, pp. 28–30].

4.3.1 Scheme of chemical reactions

The neutral chemistry scheme consists of reactions important to odd oxygen (O + O_3), odd nitrogen (N + NO + NO_2), and odd hydrogen (H + OH + HO_2) species in the upper stratosphere, mesosphere, and lower thermosphere. In addition, reactions of some other species that are important to ionospheric processes are included, such as those of metastable $O_2(^1\Delta_g)$. The scheme of positive ion reactions, presented in Fig. 4.3, is basically the same as the one given by Turunen et al. [1996], although a few reactions have been added and some rate coefficients have been updated. The negative ion scheme has been updated, see Fig. 4.4, with several, mostly hydrate ions added to the scheme of Turunen et al. [1996]. The rate coefficients have been updated where appropriate. Lists of included reactions and their rate coefficients are given in the Appendix.

Considering local production and loss for unknown gas constituents, which are dependent on each other, the continuity relation (4.6) becomes a non-linear

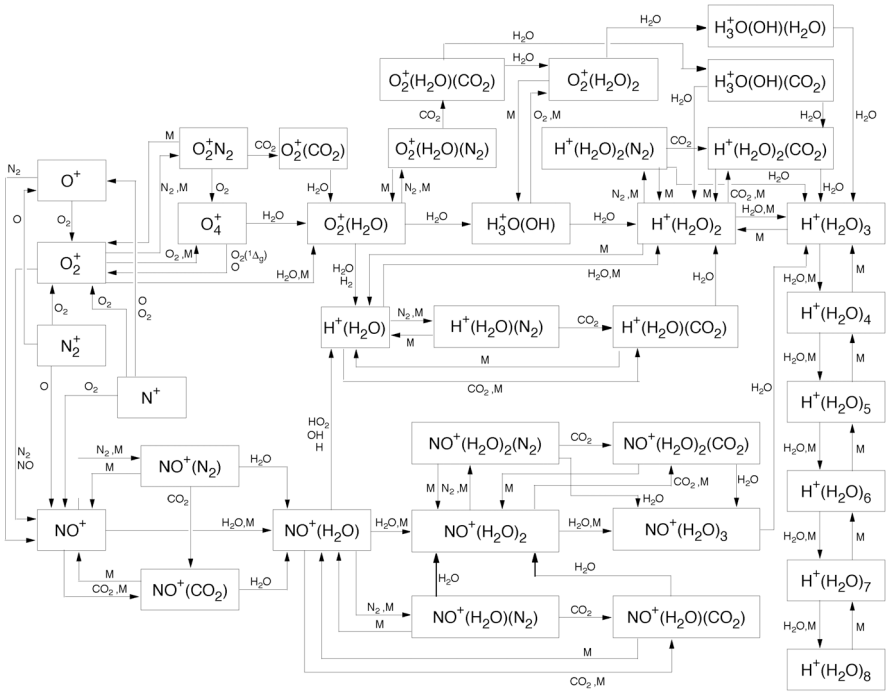

FIGURE 4.3. Block diagram for the positive ion scheme of the SIC model (courtesy of E. Turunen, Sodankylä Geophysical Observatory). The various ions in the blocks are either the reactants or the final products of the reactions sketched by the connecting arrows. The arrows are labelled with the neutral constituents taking part in the reactions. M denotes any atmospheric molecule.

set of equations and can be written in a vector form as

$$\frac{\partial \bar{N}}{\partial t} = \mathbf{B}\bar{N} + \bar{Q} = \begin{pmatrix} -\Lambda_1 & +\Pi_{12} & \dots & +\Pi_{1n} \\ +\Pi_{21} & -\Lambda_2 & & \\ \vdots & & \ddots & \\ +\Pi_{n1} & & & -\Lambda_n \end{pmatrix} \begin{pmatrix} n_1 \\ n_2 \\ n_3 \\ \vdots \\ n_n \end{pmatrix} + \begin{pmatrix} q_1 \\ q_2 \\ q_3 \\ \vdots \\ q_n \end{pmatrix}. \quad (4.9)$$

Eq. (4.9) gives a vector containing the rate of change ($\mathrm{m^{-3}\ s^{-1}}$) of the unknown species at a certain time t_o. The diagonal elements of matrix $\mathbf{B}$, $\Lambda_j = \sum L_j$, are the sum of chemical loss processes of species j, and non-diagonal elements $\Pi_{ji} = P_{ji}/n_i$ account for the production processes from constituent i. Vector $\bar{N}$ holds concentrations of the unknown species, and $\bar{Q}$ is the sum of production/loss rates due to ionisation and dissociation processes. Electron density, one of the

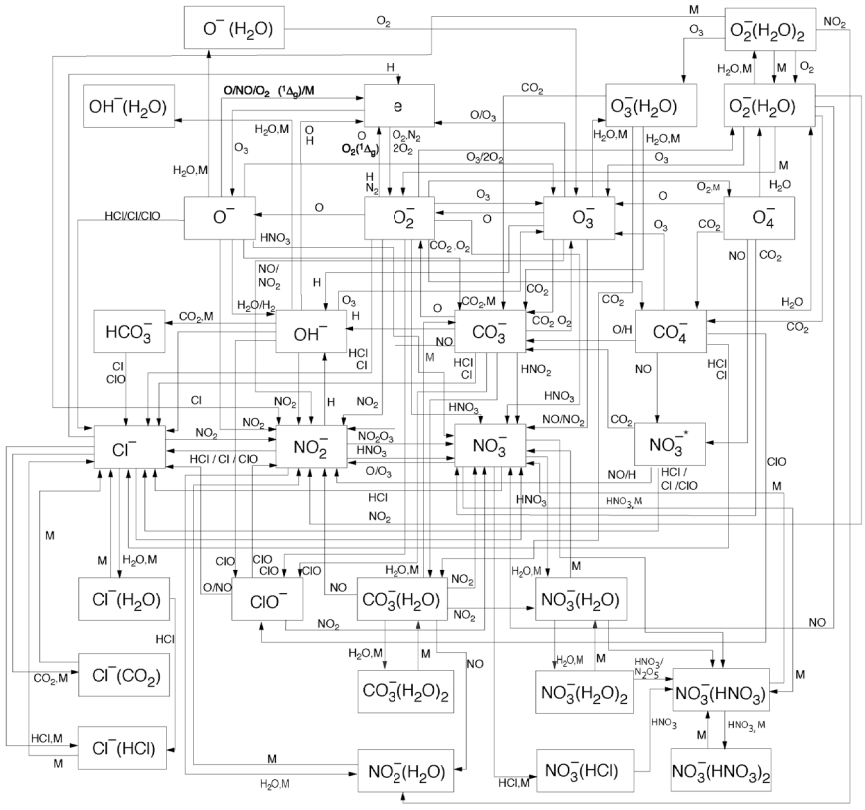

FIGURE 4.4. Same as Fig. 4.3 but for negative ions (courtesy of E. Turunen, Sodankylä Geophysical Observatory).

unknown quantities, is calculated from the ion concentrations by assuming overall charge neutrality

$$n_e = \sum_j [\mathrm{X}_j^+] - \sum_j [\mathrm{X}_j^-]. \tag{4.10}$$

Here $\sum_j[\mathrm{X}_j^+]$ and $\sum_j[\mathrm{X}_j^-]$ are the sums of positive ion and negative ion concentrations, respectively. Time-dependent concentrations of the chemical species are solved using the semi-implicit Euler method for stiff sets of equations [Press et al., 1992, pp. 727–731]. The concentrations $\bar{N}_{t_o+\Delta t}$ after a time step Δt are calculated

from the current concentrations $\bar{N}_{t_o}$ according to

$$\bar{N}_{t_o+\Delta t} = \bar{N}_{t_o} + \Delta t\ \bar{F}(\bar{N}_{t_o})\Big[\mathbf{1} - \Delta t\ \frac{\partial \bar{F}}{\partial \bar{N}}\Big|_{\vec{N}_{t_o}}\Big]^{-1} \tag{4.11}$$

The vector $\bar{F}(\bar{N}_{t_o}) = \partial \bar{N}/\partial t$ is calculated from Eq. (4.9). The information on how the constituents depend upon each other is given by a matrix containing the partial derivatives of $\bar{F}$ with respect to the individual concentrations, which we denote by $\partial \bar{F}/\partial \bar{N}$.

4.3.2 Molecular and eddy diffusion

The model being one-dimensional, the transport is represented by diffusion in the vertical direction only. The rate of change of a constituent j due to diffusion is

$$\frac{\partial n_j}{\partial t} = -\frac{\partial}{\partial z} F_j, \tag{4.12}$$

where F_j is the vertical flux ($\mathrm{m}^{-2}\ \mathrm{s}^{-1}$). We consider molecular and eddy diffusion, the former tends to separate the atmospheric species according to their mass while the latter leads towards complete mixing of the species. Therefore, these two processes compete with each other, having the same order of magnitude at altitudes around about 100 km. At lower altitudes eddy diffusion results in homogeneous distribution of gases, and at higher altitudes molecular diffusion leads to separation, the lighter gases tending towards higher altitudes. These two altitude regions are called the homosphere and heterosphere, respectively, and the limit of these regions, above which molecular diffusion cannot be neglected, is called the homopause. The molecular diffusion flux of species j at altitude z can by expressed by

$$F_j^D = -n_j\ D_j\Big[\frac{1}{n_j}\frac{\partial n_j}{\partial z} + \frac{1}{H_j} + \frac{1+\alpha_j^T}{T}\frac{\partial T}{\partial z}\Big], \tag{4.13}$$

where D_j is molecular diffusion coefficient, $H_j = kT/m_j g$ is the scale height of species j, α_j^T is the thermal diffusion factor, and T is temperature. For a derivation of Eq. (4.13), see Banks and Kockarts [1973, Part B, Chapt. 15]. Similarly, eddy diffusion flux is expressed by

$$F_j^K = -n_j\ K_{zz}\Big[\frac{1}{n_j}\frac{\partial n_j}{\partial z} + \frac{1}{H} + \frac{1}{T}\frac{\partial T}{\partial z}\Big], \tag{4.14}$$

where K_{zz} is the eddy diffusion coefficient, and $H = kT/mg$ is now the scale height of the atmosphere. Using the perfect gas law and assuming hydrostatic equilibrium, Eq. (4.14) can be expressed in the classical form

$$F_j^K = -n\ K_{zz}\ \frac{\partial N_j}{\partial z}, \tag{4.15}$$

Gas species	α_j^T	A	s
H	-0.38	4.90×10^{17}	0.708
O	–	9.69×10^{16}	0.774

Table 4.1 Thermal diffusion factor and parameters used to calculate molecular diffusion coefficient by Eq. (4.16). For the species not listed, thermal diffusion factor is set to zero and molecular diffusion coefficient is calculated by Eq. (4.17).

where N_j is the volume mixing ratio of species j. The total flux is then $F_j^D + F_j^K$, and the relative importance of the two processes depends upon their diffusion coefficients.

For molecular diffusion, the parameters in Eq. (4.13), D_j and α_j^T, can be estimated from gas kinetic theory or they can be set by measurements. The thermal diffusion factor, α_j^T, is associated with the temperature gradient and is negligible for many gases. We consider α_j^T for atomic hydrogen, adopting a constant value from Banks and Kockarts [1973, Part B, Chapt. 15]. The molecular diffusion coefficient can be calculated from

$$D_j = A \, \frac{T^s}{n}, \tag{4.16}$$

where n is total number density, and A and s are species-dependent parameters set by measurements. We use Eq. (4.16) for atomic hydrogen and atomic oxygen. For other species, measured A and s are not available and D_j is calculated, based on general kinetic theory and rigid sphere approximation, from

$$D_j = 1.52 \times 10^{18} \left(\frac{1}{M_j} + \frac{1}{M} \right)^{\frac{1}{2}} \frac{T^{\frac{1}{2}}}{n}, \tag{4.17}$$

where M_j is molecular mass of species j in atomic mass units and M is the mean atmospheric molecular mass. Table 4.1 summarises the values of α_j^T, A, and s used.

Evaluation of eddy diffusion coefficient K_{zz} is not as straightforward, as this parameter is more speculative in the nature. Depending primarily on the energy dissipation by atmospheric waves, which leads to turbulent diffusion, it can perhaps be accepted as an empirical parameter which describes the effects of transport in approximative way. Thus, K_{zz} represents, to a certain extent, the degree of turbulence in the atmosphere. Although parameterisations of K_{zz}, depending upon wave properties, exist, it is often derived from measurements of long-lived atmospheric constituents. For the model, we use an altitude profile of K_{zz} as input, assuming the same profile for all the unknown neutral species. By default, a mid-latitude, equinox profile similar to the one presented by Chabrillat et al. [2002] is assumed, but any other profile can readily be used instead. Fig. 4.5 shows examples of altitude profiles of diffusion coefficients.

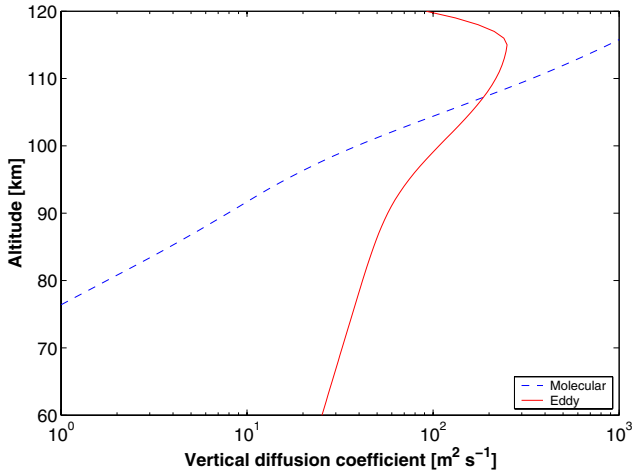

FIGURE 4.5. Example of molecular (for nitric oxide) and eddy diffusion coefficients, calculated by Eq. (4.17) and parameterisation given by Shimazaki [1971], respectively.

Eq. (4.12) is solved for after-transport gas concentrations by forming a tridiagonal system of linear equations with the dimension equal to the number of altitude grid points [*e.g.* Shimazaki, 1984; Chabrillat, 2001] and then using the LU (lower/upper) decomposition method [*e.g.* Press et al., 1992, pp. 34–47], taking into account boundary conditions at the upper and lower altitude limit. The boundary conditions are set individually for each constituent either as a fixed volume mixing ratio (VMR) or flux, based, *e.g.*, on MSISE-90 model results or measurements.

4.4 Forcing due to solar proton precipitation

4.4.1 Proton flux

High-energy proton flux measurements have been available since 1960s from satellite instruments orbiting in the near-Earth space. By default, we calculate the ionisation rate due to proton precipitation using proton flux data from the geostationary GOES satellites. These data are available from, *e.g.*, the NOAA National Geophysical Data Center World Wide Web server at *www.ndgc.noaa.gov/stp/stp.html*. GOES satellites give integrated proton fluxes above seven threshold energies: 1, 5, 10, 30, 50, 60, and 100 MeV.

An integrated proton flux J can be described by the exponential rigidity

relation [Freier and Webber, 1963],

$$J = J_0 \, e^{-P/P_0}, \tag{4.18}$$

which we use to convert the GOES measurements to differential proton fluxes over the energy range of 600 keV – 2000 MeV. In Eq. (4.18), P is proton rigidity, *i.e.* the momentum p per unit charge q, which can be related to proton energy E by

$$P = \frac{p}{q} = \frac{1}{qc}\sqrt{E(E + 2m_p c^2)}. \tag{4.19}$$

Here m_p is the rest mass of proton and c is the speed of light. P_0 and J_0 are the characteristic rigidity and corresponding flux, respectively, calculated for each consecutive pair of GOES energies E_i and E_{i+1} by solving from Eq. (4.18)

$$P_0 = \frac{P_i - P_{i+1}}{\ln J_{i+1} - \ln J_i} \tag{4.20}$$

$$J_0 = \frac{P_i \ln J_{i+1} - P_{i+1} \ln J_i}{P_{i+1} - P_i}. \tag{4.21}$$

After obtaining P_0 and J_0 for each successive pair of GOES energy limits, Eq. (4.18) is used to calculate integral flux values J for a desired energy grid within the range. Finally, the dense-grid integral flux values are converted to differential flux values F_d according to

$$F_d = \frac{J_k - J_{k+1}}{E_{k+1} - E_k} \tag{4.22}$$

with corresponding mean energy being

$$E_d = \frac{E_{k+1} + E_k}{2}. \tag{4.23}$$

Fig. 4.6 shows an example of GOES proton flux measurements and the converted differential spectrum.

For magnetic latitudes higher than about 60°, geomagnetic cutoff can be considered negligible, practically all energetic SPE protons are able to enter the atmosphere, and the GOES flux measurements at the geostationary orbit can be used as such [*e.g.* Hargreaves, 1992, p. 355–359]. For lower latitudes, it becomes necessary to consider the time-varying geomagnetic cutoff energy, which we calculate using a method given in Paper V. The method is based on the cutoff rigidity modelling by Smart and Shea [2003], and is dependent on the planetary magnetic index K_p. The output is a cutoff energy for protons at a given geographical location E_{cut}, which is then used to modify the differential flux of protons simply by setting the flux equal to zero for all energies lower than E_{cut}.

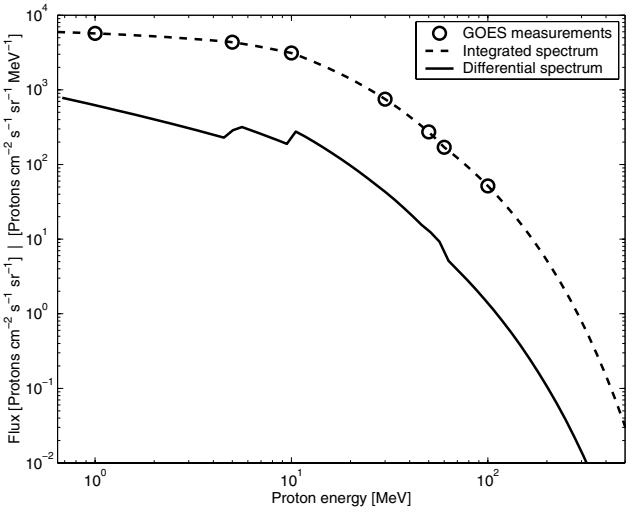

FIGURE 4.6. GOES proton flux measurements, and the corresponding integrated and differential spectrum after conversions. The measurements were made during the largest SPE of 1989, on October 23, and are mean values for 12–15 UT.

4.4.2 Ionisation and dissociation rates

Although at lower energies protons are able to undergo charge-exchange reactions with the neutral molecules, for the energy range relevant for middle atmosphere penetration they can be neglected, and the energy loss of precipitating protons is dominantly due to ionisation processes [Rees, 1982]. Several methods exist that can be used to calculate the energy input of protons and the resulting ionisation rate in the atmosphere. Decker et al. [1996] have presented a comparison of three different modelling approaches: Monte Carlo, linear transport, and continuously slowing-down approximation. They found a very good agreement between the three methods except for the cases where protons had penetrated so deep that their fluxes were significantly modified, which happens well below the bulk ionisation region. Recently, Schröter et al. [2005] have compared Monte Carlo and continuous energy loss models and found the calculated ionisation rates to be essentially the same for 1–500 MeV protons. Our ionisation rate calculation is done with a computationally fast procedure, and it is based on proton energy-range measurements in standard air [Bethe and Ashkin, 1953]. The energy-range relation for protons can be written

$$R(E) = aE^b \tag{4.24}$$

where R is the range, E is the proton energy, and a and b are parameters set by measurements. Using the following algorithm, originally presented by Reid [1961],

we calculate energy deposition rates on each altitude: The stopping power of a proton with initial energy E and pitch angle θ at altitude z_o is

$$\frac{dE}{dx} = \left(\frac{dR(E, z_o, \theta)}{dE} \right)^{-1} \tag{4.25}$$

where

$$R(E, z_o, \theta) = R(E) - \frac{1}{n(0)} \int_{z_o}^{\infty} \frac{n(z)}{\cos\theta} \, dz \tag{4.26}$$

is the remaining range at altitude z_o. The total concentrations $n(0)$ and $n(z)$ are taken at ground level and at altitude z, respectively. The last term in Eq. (4.26) is the standard air range, *i.e.* energy, lost by a proton in penetrating the atmosphere down to altitude z_o. By dividing Eq. (4.25) by mean ionisation energy $\Delta\epsilon$, taken to be 36 eV (see *e.g.* Rees [1989], pp. 35–45), and multiplying by the proton flux $F(E)$ and then integrating over energies and angles, we get the total ionisation rate for each altitude from

$$Q = \frac{1}{\Delta\epsilon} \int\int\int \left(\frac{dE}{dx} \right) F(E) \sin\theta \, d\theta d\phi dE \tag{4.27}$$

The angular distribution of protons is assumed to be isotropic over the upper atmosphere, which is valid in the near-Earth space [Hargreaves, 1992, pp. 353–355]. The integration is executed with the Gaussian quadrature method [Press et al., 1992, pp. 140–155]. Fig. 4.7 shows, as an example, the calculated ionisation rates during the October 1989 SPE.

The total ionisation rate is divided between N_2, O_2, and O according to their relative concentrations and cross sections [Rees, 1982], so that

$$Q_{N_2} = Q \, \frac{[N_2]}{[N_2] + [O_2] + 0.8 \, [O]} \tag{4.28}$$

$$Q_{O_2} = Q \, \frac{[O_2]}{[N_2] + [O_2] + 0.8 \, [O]} \tag{4.29}$$

$$Q_{O} = Q \, \frac{0.8 \, [O]}{[N_2] + [O_2] + 0.8 \, [O]}. \tag{4.30}$$

The ionisation rates of N_2 and O_2, are then divided between the ionisation and dissociative ionisation processes using the branching ratios given by Jones [1974] to obtain the production/loss rates for the individual species, see Table 4.2.

As a result of direct proton impact, we consider production of four different ionic species (N_2^+, N^+, O_2^+, and O^+) as well as atomic oxygen and atomic nitrogen. Dissociation of N_2 by secondary electrons is an important source of atomic nitrogen which we take into account using a simple parameterisation

$$D^{sec} = C \, Q(z_o), \tag{4.31}$$

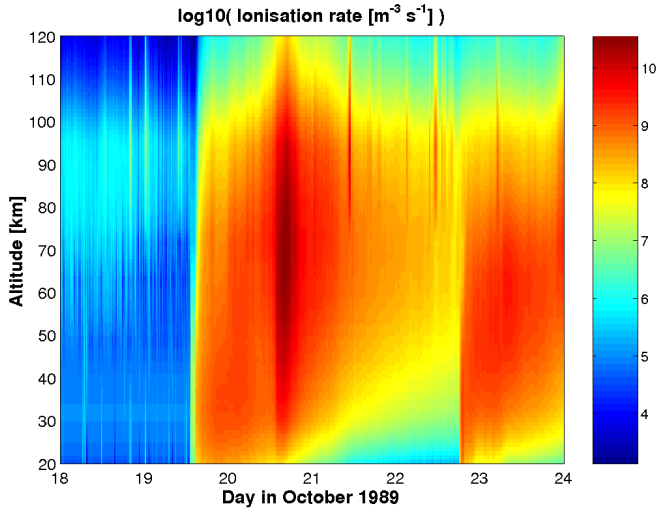

FIGURE 4.7. Total ionisation rate due to proton precipitation during the first days of the October 1989 SPE. Calculated by Eq. (4.27) using proton flux data from GOES-7 satellite.

where C is an altitude-independent constant. By default, the value of 0.8 is adopted for C according to the lower limit given by Rusch et al. [1981], based on relative magnitudes of dissociation and ionisation cross sections. For atomic nitrogen production, it is important to consider the branching between the ground state N(^{4}S) and the excited state N(^{2}D) because production of the former leads to odd nitrogen loss through fast reaction (2.10). Table 4.2 gives also the N(^{2}D)/N(^{4}S) branching ratios used as well as their sources.

4.5 EXECUTION OF THE MODEL

When the model is run, transport and chemistry are advanced in intervals during which the background atmosphere and external forcing are kept fixed. Typically 5 or 15-min intervals are used. For every interval, 1) new values for solar zenith angle, background atmosphere, and ionisation/dissociation rates due to solar radiation and particle precipitation are calculated, 2) all modelled neutral constituents, except the photochemically short-lived O(^{1}D) and N(^{2}D) and $O_2(^1\Delta_g)$, are transported, and 3) the chemistry is advanced. See Fig. 4.1 in the beginning of this chapter for a schematic structure of the model.

The individual photochemical lifetimes of modelled ions and neutrals vary by several orders of magnitude, making the set of ordinary differential equations in Eq. (4.9) stiff [*e.g.* Jacobson, 1999]. For an explicit solution, *i.e.* $N_{t_o+\Delta t} =$

Reaction			Rate (m^{-3} s^{-1})	$N(^2D)/N(^4S)$ branching
$N_2 + p$	$\rightarrow$	$N_2^+ + e^* + p'$	0.76 Q_{N_2}	–
$N_2 + p$	$\rightarrow$	$N^+ + N + e^* + p'$	0.24 Q_{N_2}	0.5/0.5 [Porter et al., 1976]
$O_2 + p$	$\rightarrow$	$O_2^+ + e^* + p'$	0.67 Q_{O_2}	–
$O_2 + p$	$\rightarrow$	$O^+ + O + e^* + p'$	0.33 Q_{O_2}	–
$N_2 + e^*$	$\rightarrow$	$2N + e^*$	0.80 Q	0.6/0.4 [Zipf et al., 1980]

Table 4.2 Ionisation and dissociation of N_2 and O_2 due to proton and secondary electron impact. p and p′ mark the proton before and after the ionisation, respectively. e^* is a secondary electron. The rates are given as fractions of ionisation rates.

$N_{t_o} + \bar{F}(\bar{N}_{t_o})\ \Delta t$, the time step Δt is limited by the lifetime of shortest-lived constituent, which may be of the order of 10^{-4} s or less, thus making the time integration over just hours very time-consuming and impractical. If longer time steps are used, the solution scheme may be destabilised. By adopting a semi-implicit scheme, like the one in Eq. (4.11), much longer time steps can be used. In addition, we use an exponentially increasing time step within each calculation interval. In the beginning the time step is quite small, less than one second, whereas the final step may be hundreds of seconds. The initially small time steps allow the fast species to settle in after sometimes very large changes in external forcing, after which it is possible to advance with longer time steps and keep the computing time reasonable.

Before the model is used for a scientific study, it needs to be initialised. This is done after selecting the location and day of year by repeatedly modelling the diurnal cycle for that specific day until the results converge. Then the model has reached a stable state, such that the modelled concentrations during the last diurnal cycle are not significantly changed from the previous one. The number of diurnal cycles required for a convergence depends on the assumed initial concentrations, a good guess reducing the number significantly. Typically, we use results of some previous modelling work as a starting set of concentrations, so that after 10–20 diurnal cycles the convergence is usually better than 2%.

4.6 About applicability, uncertainties, and future

The SIC model, being one-dimensional, represents the ionosphere and atmosphere at a single location. Because the atmospheric transport can only be taken into account in the vertical direction, it is evident that horizontal transport by winds restricts the model applicability significantly. SIC is best suited for short-term studies of photochemical changes caused by sudden disturbances, like SPEs, of which it can provide a rather detailed picture. In comparison with measurements, it may be more useful to look at relative changes rather than absolute concentra-

tions of species.

The SIC model representation of the atmosphere is obviously sensitive to the selected background atmosphere and other input (*i.e.* initialisation), as well as the selection of atmospheric processes included. The initial state of the model, in the beginning of a model run, will affect the final results, so that the initialisation should be made carefully, preferably using observations although these are many times not available. On the other hand, even if the model is initialised perfectly, the results are dependent on the capabilities of the model, *i.e.* what processes are included and to what extent they are taken into account. In the case of SIC model, horizontal transport is neglected. This means that the model is not able to determine the dynamical fate of long-lived species. Therefore, the model runs should be restricted in time, so that the effect of dynamics can be considered to be minor or at least not dominant. In practice this means that model runs lasting months are not meaningful. For example, SIC is a suitable tool for determining the production of NO_x during SPEs (duration from hours to days), but it cannot be used to study the subsequent long-term transport of the produced odd nitrogen.

Process selection also determines the relevant altitude range for the model. The operational range of the SIC model is from 20 to 150 km. However, the neutral chemistry currently included is sufficient for altitudes of the upper stratosphere and above. Also, the model does not include some positive nonproton hydrates or negative sulfur ions which are present in the stratosphere [Brasseur and Solomon, 2005, pp. 564–570 and 577–581]. In addition, it should be noted that the model takes the electron temperature equal to the neutral temperature, which is generally not true in the thermosphere.

Sources of uncertainty in the SIC model are various, starting from the daily average solar flux values, the neutral background atmosphere, and temperature. Further, ionisation and dissociation cross sections, diffusion parameters, and reaction rate coefficients have their own errors. In a complex atmospheric model like SIC, consisting of numerous processes of which many are dependent on each other, it is quite impossible to analytically evaluate the accuracy of the results. The sensitivity to one parameter or a set of input parameters can be studied, giving important information on the robustness of the model results, but the ultimate test to any model is comparison with observations. The better the agreement between the model and measurements, the better the model. However, one must remember that observations have also uncertainties and they can even be biased. Because there are many more or less "free" input parameters in the SIC model, it might be possible to reproduce any measurement with some combination of these parameters, without a guarantee that this combination really represented the true state of the atmosphere. It is, therefore, better to be somewhat conservative and cautious, and keep in mind the limitations of the model, when trying to match the measurements.

The SIC model has been applied to SPE studies, both ionospheric and ozonospheric, quite successfully. Similar studies have been also been done with electron precipitation events. The core of the model, the combined ion and neutral chemistry scheme, may readily be used to study any phenomena that involves atmospheric ionisation and dissociation and subsequent changes in ionic and neutral constituents. Thus the SIC future lies very much in the capability to model in detail specific ionospheric processes. For example, a parallel model is being developed at Sodankylä Geophysical Observatory, in order to study atmospheric effects of middle atmospheric lightning, *i.e.* sprites, elves, and blue jets, in the mesosphere. With the recent rise of whole atmosphere models, in which the altitude range is from ground level up to upper thermospheric heights, a need for an ion chemistry module for 3-D atmospheric models has emerged. Such a module, which should be simplified and computationally very fast, could be developed based on the SIC ion chemical scheme.

5 Results: Summaries of the original publications

This chapter summarises the work done in Papers I–V.

I This paper discusses the long-term changes observed in NO_2 and ozone concentrations after the October-November 2003 SPE. The GOMOS instrument measured, for the first time, effects of an SPE in the winter polar regions.

It was shown that the SPE produced significant amounts of NO_x at altitudes above 36 km in the polar cap region, with simultaneous ozone depletion of several tens of per cent. Descent of NO_x inside the polar vortex observed from the mesosphere to stratosphere resulted in the maximum ozone depletion by 60% in the upper stratosphere in the end of November, about one month after the SPE occurred. The observed partial column densities for the 36-50 km altitude range showed clear deviation from the climatological values after the event, returning towards normal levels in the end of the year. The changes in O_3 and NO_2 columns were strongly negatively correlated, as was expected from the known ozone chemistry. The SPE effects were shown to remain inside the polar vortex, until its breakup in the late December.

II This paper discusses diurnal variation of ozone depletion during the October-November 2003 SPE. A novel combination of ground-based radio propagation measurements and unique satellite measurements of ozone and NO_2 were used together with the SIC model, offering a more complete approach to SPE-induced processes than the previous work on the subject.

The variations in modelled and observed VLF signals showed very good agreement, giving confidence on the modelled ionospheric response of some substance. The model results showed order-of-magnitude changes in NO_x and HO_x concentrations at stratospheric and mesospheric altitudes, with clearly different recoveries after reduction in proton forcing. HO_x recovered during one quiet day, while the NO_x concentrations stayed at an elevated level showing no apparent recovery. The modelling indicated significant diurnal variation in mesospheric ozone depletion, with implications to the use of satellite measurements in determining the magnitude of the depletion. Largest depletions were modelled during sunrise and sunset times, when atomic oxygen is available for catalytic reaction cycles and background production of HO_x is relatively low. While in the mesosphere the ozone recovery was found to be fast during daytime, longer-term depletion was seen in the stratopause region due to NO_x increase and relatively smaller photodissociation-driven ozone production. At 35–70 km, the modelled NO_2 increase was confirmed by the GOMOS measurements indicating a correct

modelling of NO_x production by the SPE. The modelled day-to-day variations in ozone depletion agreed with GOMOS measurements, especially in the mesosphere. At stratopause region, the observed ozone depletion showed more variation than the model results, perhaps indicating a shortcoming in the modelled, SPE-induced ion-chemical production of HO_x.

III The GOMOS instrument provides unique night-time data of mesospheric ozone. Earlier observations have been made with ground-based and space shuttle instruments, but satellite data from the night side has been limited. Validation of GOMOS data has concentrated on stratospheric altitudes, and this paper is the first to consider also the mesospheric observations.

GOMOS night-time ozone profiles were compared with those from the MIPAS instrument. Due to lack of MIPAS observations in the mesosphere, the validation at this point was restricted to two dates. After compensating for the different vertical resolutions of the two instruments, both individual ozone profiles as well as statistical average profiles were compared. Agreement within 10–15% was found in the stratosphere and lower mesosphere. Although the relative difference was high around the 80 km ozone minimum, the absolute values agreed within 0.5–1 ppmv. In the mesopause region, around the secondary ozone maximum, the agreement was within 30%. It was concluded that GOMOS and MIPAS are generally in a good agreement throughout the middle atmosphere, giving confidence on data from both instruments.

IV This paper discusses the behaviour of D-region ionosphere during twilight, a long-standing problem. By combining a set of measurements from several instruments and a 1-D ion and neutral chemistry model, this study makes a new contribution to the D-region research.

We study the negative charge transition during the sunset of October 23, 1989, under SPE conditions. In the modelling, the changes in solar radiation and minor neutral species with respect to the solar zenith angle are taken into account, as well as the changes in neutral composition caused by the SPE since its onset on October 18. The sunset transition depends upon solar radiation at both ultraviolet (UV) and visible (VIS) wavelengths, relative sizes varying with altitude. For the case studied, it was shown that the VIS response is due to photodetachment reactions. On the other hand, the UV response comes mostly from the changes in atomic oxygen and excited molecular oxygen, rather than from photodetachment reactions. Further, negative ion composition and the sunset transition characteristics were shown to be sensitive to neutral atmospheric changes caused by the SPE, especially to the amount of nitric oxide. Therefore, correct modelling of minor neutral species is important, if not crucial for twilight studies in the D-region.

These model results were validated using ionospheric measurements from the Kilpisjärvi riometer and EISCAT incoherent scatter radar, and rocket-borne measurements of nitric oxide. The modelled sunset transition characteristics were confirmed by the observations, although differences in absolute electron densities existed. Since the model uncertainties were not able to fully explain the differences, and it was suggested that in addition to protons another ionisation source, most likely electron precipitation, was present. By including a simple estimation of electron spectrum in the model, the modelled and observed electron densities showed an excellent agreement.

V This paper discusses dynamic geomagnetic rigidity cutoff variations during the SPE of November 2001. A detailed comparison between theoretical cutoff rigidities and ground-based measurements during an SPE gave new information on the validity of particle-tracing and magnetic field models under different levels of magnetic disturbance, aiding a better definition of geomagnetic latitude coverage of the SPE effects.

Theoretical cutoff energies for protons during the SPE were determined using a K_p-dependent method based on satellite observations and particle-tracing modelling. The theoretical results were used to predict cosmic radio noise absorption observed by an imaging riometer at Halley Bay, Antarctica. It was shown that the theoretical absorption is in a good agreement with the cutoff-affected observations for low and mid levels of geomagnetic disturbance. During more disturbed condition, however, the predicted absorption is too high due to over-estimation of stretching of the geomagnetic field. It was concluded that the geomagnetic limit for the penetration of protons is rather more poleward than has been indicated previously. Theoretical predictions for highly disturbed conditions could be improved by using a different magnetic field model.

6 Concluding remarks

In this thesis, we have studied ionospheric and atmospheric effects of solar proton events, using a one-dimensional combined ion and neutral photochemistry model together with both ionospheric and atmospheric observations. Although SPEs have been studied since the 1950s, this work is quite unique in its approach. Instead of using simple approximations to model ion chemistry effects on minor neutral constituents, an extensive set of ionic reactions are combined with a basic set of neutral chemistry. Such a model is a most suitable tool for studying processes of ionosphere-atmosphere interaction during SPEs, or other similar disturbances, and allows for utilisation of large variation of measurements covering the chain of processes from ionisation to ozone depletion. These data, unique night-time ozone data from the GOMOS instrument as well as the wide selection of ionospheric data, have been used to validate the model results to an extent not seen before. Although the agreement with model results and the observations is generally good, there are areas needing further investigation. One such puzzling matter is the difference between the observed and modelled ozone depletion in the stratopause region. Nevertheless, exciting new results have been obtained, with a special thanks going to the GOMOS instrument which has shown the capabilities of stellar occultation technique in observing the middle atmosphere from the tropopause up to the mesopause region.

GOMOS measurements of ozone and NO_2 have shown how the October-November 2003 SPE lead to long-term changes in the northern hemispheric upper stratosphere. A large role in this was played by the exceptionally stable polar vortex which confined the affected air until a stratospheric warming in late December displaced the vortex from the pole. High levels of stratospheric odd nitrogen observed in the following spring have been associated to this large SPE by Natarajan et al. [2004], while the study by Randall et al. [2005] indicates another source in the beginning of 2004. GOMOS measurements could perhaps answer the questions whether the spring enhancement was due to the SPE or, *e.g.*, energetic electron precipitation later, but the data for early 2004 has not been available yet. Recently, [Clilverd et al., 2005c] have shown, based on ionospheric measurements, that the observed NO_x is likely of thermospheric origin.

The diurnal variation of ozone depletion was also observed by GOMOS during the October-November 2003 SPE, although the measurements for the selected latitude band were made at two local times only. Diurnal variations could perhaps be better observed by an ground-based instrument if it provided continuous observations, covering all local times with a fine time resolution. The bottom panel of Fig. 7 in Paper II, showing the ozone depletion time series at 50 km, displays some interesting features. The model is showing mainly the effect of odd nitrogen increase, *i.e.* more or less constant depletion after October 29, while the

measurements seem to show a combination of effects, *i.e.* a variable effect due to odd hydrogen increase superimposed on a fixed depletion level due to odd nitrogen increase. This could indicate a deficiency in the odd hydrogen modelling theory, and should be investigated. Measurements of odd hydrogen species would be a great aid when addressing this question.

Bibliography

Allen, M., Lunine, J. I., and Yung, Y. L., The vertical distribution of ozone in the mesosphere and lower thermosphere, *Journal of Geophysical Research*, *89*, 4841–4872, 1984.

Anderson, K. A. and Enemark, D. C., Observations of cosmic rays near the north magnetic pole, *Journal of Geophysical Research*, *65*, 2657–2671, 1960.

Arijs, E., Nevejans, D., and Ingels, J., Stratospheric positive ion composition measurements and acetonitrile detection: a consistent picture?, *International Journal of Mass Spectrometry and Ion Processes*, *81*, 15–31, 1987.

Bailey, D. K., Polar car absorption, *Planetary and Space Science*, *12*, 459–541, 1964.

Banks, P. M. and Kockarts, G., *Aeronomy*, Academic Press, 1973.

Barr, R., Jones, D. L., and Rodger, C. J., ELF and VLF radio waves, *Journal of Atmospheric and Terrestrial Physics*, *62*, 1689–1718, 2000.

Barth, C. A., Nitric oxide in the lower thermosphere, *Planetary and Space Science*, *40*, 315–336, 1992.

Bates, D. R. and Nicolet, M., The photochemistry of atmospheric water vapor, *Journal of Geophysical Research*, *55*, 301–327, 1950.

Bertaux, J. L., Megie, G., Widemann, T., Chassefiere, E., Pellinen, R., Kyrölä, E., Korpela, S., and Simon, P., Monitoring of ozone trend by stellar occultations: The GOMOS instrument, *Advances in Space Research*, *11*, 237–242, 1991.

Bertaux, J. L., Hauchecorne, A., Dalaudier, F., Cot, C., Kyrölä, E., Fussen, D., Tamminen, J., Leppelmeier, G. W., Sofieva, V., Hassinen, S., d'Andon, O. F., Barrot, G., Mangin, A., Théodore, B., Guirlet, M., Korablev, O., Snoeij, P., Koopman, R., and Fraisse, R., First results on GOMOS/Envisat, *Advances in Space Research*, *33*, 1029–1035, 2004.

Bethe, A. H. and Ashkin, J., *Passage of Radiations through Matter*, vol. 1 of *Experimetal Nuclear Physics, edited by E. Segre*, pp. 166–251, John Wiley & Sons, Inc., New York, USA, 1953.

Brasseur, G. and Solomon, S., *Aeronomy of the Middle Atmosphere*, D. Reidel Publishing Company, Dordrecht, 2nd edn., 1986.

Brasseur, G. P. and Solomon, S., *Aeronomy of the Middle Atmosphere*, Springer, Dordrecht, 3rd revised and enlarged edn., 2005.

Burns, C. J., Turunen, E., Matveinen, H., Ranta, H., and Hargreaves, J. K., Chemical Modeling of the Quiet Summer D- and E-regions Using EISCAT Electron Density Profiles, *Journal of Atmospheric and Terrestrial Physics*, *53*, 115–134, 1991.

Callis, L. B., Stratospheric studies consider crucial question of particle precipitation, *Transactions, American Geophysical Union (EOS)*, *82*, 297–301, 2001.

Callis, L. B. and Lambeth, J. D., NO_y formed by precipitating electron events in 1991 and 1992: Descent into the stratosphere as observed by ISAMS, *Geophysical Research Letters*, *25*, 1875–1878, 1998.

Callis, L. B., Boughner, R. E., Natarajan, M., Lambeth, J. D., Baker, D. N., and Blake, J. B., Ozone depletion in the high latitude lower stratosphere: 1979-1990, *Journal of Geophysical Research*, *96*, 2921–2937, 1991.

Cane, H. V., von Rosenvinge, T. T., Cohen, C. M. S., and Mewaldt, R. A., Two components in major solar particle events, *Geophysical Research Letters*, *30*, 8017, 2003.

Chabrillat, S., *Modélisation du changement global dans l'atmosphère moyenne*, Ph.D. thesis, Université Libre des Bruxelles, 2001.

Chabrillat, S., Kockarts, G., Fonteyn, D., and Brasseur, G., Impact of molecular diffusion on the CO_2 distribution and the temperature in the mesosphere, *Geophysical Research Letters*, *29*, 1–4, 2002.

Chapman, S., On ozone and atomic oxygen in the upper atmosphere, *Philosophical Magazine and Journal of Science*, *10*, 369–387, 1930.

Chivers, H. J. A. and Hargreaves, J. K., Conjugate observations of solar proton events: delayed ionospheric changes during twilight, *Planetary and Space Science*, *13*, 583–592, 1965.

Clarmann, T. v., Glatthor, N., Höpfner, M., Kellmann, S., Ruhnke, R., Stiller, G. P., Fischer, H., Funke, B., Gil-Lopéz, and Lopéz-Puertas, Experimental evidence of perturbed odd hydrogen and chlorine chemistry after the October 2003 solar proton events, *Journal of Geophysical Research*, *110*, A09S45, 2005.

Clilverd, M. A., Rodger, C. J., Ulich, T., Seppälä, A., Turunen, E., Botman, A., and Thomson, N. R., Modelling a large solar proton event in the southern polar cap, *Journal of Geophysical Research*, *110*, A09 307, 2005a.

Clilverd, M. A., Seppälä, A., Rodger, C. J., Thomson, N. R., Verronen, P. T., Turunen, E., Ulich, T., Lichtenberger, J., and Steinbach, P., Modelling polar ionospheric effects during the october-november 2003 solar proton events, *Radio Science*, accepted for publication, 2005b.

Clilverd, M. A., Seppälä, A., Rodger, C. J., Verronen, P. T., and Thomson, N. R., Ionospheric evidence of thermosphere-to-stratosphere descent of polar NO_x, *Geophysical Research Letters*, submitted, 2005c.

Collis, P. N. and Rietveld, M. T., Mesospheric observations with the EISCAT UHF radar during polar cap absorption events: 1. Electron densities and negative ions, *Annales Geophysicæ*, *8*, 809–824, 1990.

Crutzen, P. J., Isaksen, I. S. A., and Reid, G. C., Solar proton events: Stratospheric sources of nitric oxide, *Science*, *189*, 457–458, 1975.

Dalgarno, A., Atmospheric reactions with energetic particles, *Space Research*, *7*, 849–861, 1971.

Decker, D. T., Kozelov, B. V., Basu, B., Jasperse, J. R., and Ivanov, V. E., Collisional degradation of the proton-H atom fluxes in the atmosphere: A comparison of theoretical techniques, *Journal of Geophysical Research*, *101*, 26 947–26 960, 1996.

Degenstein, D. A., Lloyd, N. D., Bourassa, A. E., Gattinger, R. L., and Llewellyn, E. J., Observations of mesospheric ozone depletion during the October 28, 2003 solar proton event by OSIRIS, *Geophysical Research Letters*, *32*, 2005.

DeMore, W. B., Sander, S. P., Golden, D. M., Hampson, R. F., Kurylo, M. J., Howard, C. J., Ravishankara, A. R., Kolb, C. E., and Molina, M. J., *Chemical Kinetics and Photochemical Data for Use in Stratospheric Modeling*, JPL Publication 92-20, Jet Propulsion Laboratory, California Institute of Technology, Pasadena, USA, 1992.

Detrick, D. L. and Rosenberg, T. J., A phased-array radiowave imager for studies of cosmic noise absorption, *Radio Science*, *25*, 325–338, 1990.

Farman, J. C., Gardiner, B. G., and Shanklin, J. D., Large losses of total ozone in antarctica reveal seasonal ClO_x/NO_x interaction, *Nature*, *315*, 207–210, 1985.

Fell, C., Steinfeld, J. I., and Miller, S., Quenching of N(2D) by O(3P), *Journal of Chemical Physics*, *92*, 4768–4777, 1990.

Freier, P. S. and Webber, W. R., Exponential Rigidity Spectrums for Solar-Flare Cosmic Rays, *Journal of Geophysical Research*, *68*, 1605–1629, 1963.

Fuller-Rowell, T. J., Modeling the solar cycle change in nitric oxide in the thermosphere and upper mesosphere, *Journal of Geophysical Research*, *98*, 1559–1570, 1993.

Gillmor, C. S., The day-to-night ratio of cosmic noise absortion during polar cap absorition events, *Journal of Atmospheric and Terrestrial Physics*, *25*, 263–266, 1963.

Hargreaves, J. K., *The solar-terrestrial environment*, Cambridge Atmospheric and Space Science Series, Cambridge University Press, Cambridge, UK, 1992.

Hargreaves, J. K., Ranta, H., Ranta, A., Turunen, E., and Turunen, T., Observations of the polar cap absorption event of February 1984 by the EISCAT incoherent scatter radar, *Planetary and Space Science*, *35*, 947–958, 1987.

Heaps, M. G., *The effect of a solar proton event on the minor neutral constituents of the summer polar mesosphere*, no. ASL-TR0012 in U.S. Army Atmospheric Science Laboratory Reports, 1978.

Heath, M., Krueger, A., and Crutzen, P., Solar proton event- influence on stratospheric ozone, *Science*, *197*, 886–889, 1977.

Hedin, A. E., Extension of the MSIS Thermospheric Model into the Middle and Lower Atmosphere, *Journal of Geophysical Research*, *96*, 1159–1172, 1991.

Hertzberg, L., The possible importance of nitric oxide formation during polar cap ionospheric absorption events, *Journal of Geophysical Research*, *65*, 3505, 1960.

Jackman, C. H. and McPeters, R. D., The responce of ozone to solar proton events during solar cycle 21: A theoretical interpretation, *Journal of Geophysical Research*, *90*, 7955–7966, 1985.

Jackman, C. H. and McPeters, R. D., The Effect of Solar Proton Events on Ozone and Other Constituents, in *Solar Variability and its Effects on Climate*, vol. 141 of *Geophysical Monograph*, pp. 305–319, American Geophysical Union, 2004.

Jackman, C. H., Frederick, J. E., and Stolarski, R. S., Production of odd nitrogen in the stratosphere and mesosphere - An intercomparison of source strengths, *Journal of Geophysical Research*, *85*, 7495–7505, 1980.

Jackman, C. H., Douglass, A. R., Rood, R. B., McPeters, R. D., and Meade, P. E., Effect of solar proton events on the middle atmosphere during the past two solar cycles as computed using a two-dimensional model, *Journal of Geophysical Research*, *95*, 7417–7428, 1990.

Jackman, C. H., Cerniglia, M. C., Nielsen, J. E., Allen, D. J., Zawodny, J. M., McPeters, R. D., Douglass, A. R., Rosenfield, J. E., and Hood, R. B., Two-dimensional and three-dimensional model simulations, measurements, and interpretation of the October 1989 solar proton events on the middle atmosphere, *Journal of Geophysical Research*, *100*, 11 641–11 660, 1995.

Jackman, C. H., Fleming, E. L., Chandra, S., Considine, D. B., and Rosenfield, J. E., Past, present, and future modeled ozone trends with comparisons to observed trends, *Journal of Geophysical Research*, *101*, 28 753–28 768, 1996.

Jackman, C. H., Fleming, E. L., and Vitt, F. M., Influence of extremely large solar proton events in a changing stratosphere, *Journal of Geophysical Research*, *105*, 11 659–11 670, 2000.

Jackman, C. H., McPeters, R. D., Labow, G. J., Fleming, E. L., Praderas, C. J., and Russel, J. M., Northern hemisphere atmospheric effects due to the July 2000 solar proton events, *Geophysical Research Letters*, *28*, 2883–2886, 2001.

Jacobson, M. Z., *Fundamentals of atmospheric modeling*, Cambridge University Press, 1999.

Johnson, C. Y., Meadows, E. B., and Holmes, C. J., Ion composition of the arctic ionosphere, *Journal of Geophysical Research*, *63*, 443–451, 1958.

Jones, A. V., *Aurora*, D. Reidel Publishing Co., Dordrecht, Holland, 1974.

Kazil, J., *The University of Bern Atmospheric Ion Model: Time-dependent ion modeling in the stratosphere, mesosphere, and lower thermosphere*, Ph.D. thesis, University of Bern, 2002.

Koppers, G. A. A. and Murtagh, D. P., Model studies of the influence of O_2 photodissociation parameterizations in the Schumann-Runge bands on ozone related photolysis in the upper atmosphere, *Annales Geophysicæ*, *14*, 68–79, 1996.

Kyrölä, E., Sihvola, E., Kotivuori, Y., Tikka, M., Tuomi, T., and Haario, H., Inverse theory for occultation measurements, 1, Spectral inversion, *Journal of Geophysical Research*, *98*, 7367–7381, 1993.

Kyrölä, E., Tamminen, J., Leppelmeier, G. W., Sofieva, V., Hassinen, S., Bertaux, J.-L., Hauchecorne, A., Dalaudier, F., Cot, C., Korablev, O., d'Andon, O. F., Barrot, G., Mangin, A., Theodore, B., Guirlet, M., Etanchaud, F., Snoeij, P., Koopman, R., Saavedra, L., Fraisse, R., Fussen, D., and Vanhellemont, F., GOMOS on Envisat: An overview, *Advances in Space Research*, *33*, 1020–1028, 2004.

Lary, D. J., Catalytic destruction of stratospheric ozone, *Journal of Geophysical Research*, *102*, 21 515–21 526, 1997.

Lopéz-Puertas, M., Funke, B., Gil-Lopéz, S., Clarmann, T. v., Stiller, G. P., Höpfner, M., Kellmann, S., Fischer, H., and Jackman, C. H., Observation of NO_x enhancement and ozone depletion in the northern and southern hemispheres after the October-November 2003 solar proton events, *Journal of Geophysical Research*, *110*, A09S43, 2005a.

Lopéz-Puertas, M., Funke, B., Gil-Lopéz, S., Clarmann, T. v., Stiller, G. P., Höpfner, M., Kellmann, S., Mengistu Tsidu, G., Fischer, H., and Jackman, C. H., HNO_3, N_2O_5 and $ClONO_2$ enchancements after the October-November 2003 solar proton events, *Journal of Geophysical Research*, *110*, A09S44, 2005b.

Matsuoka, S., Nakamura, H., and Tamura, T., Ion-molecule reactions of N_3^+, N_4^+, O_2^+, and NO_2^+ in nitrogen containing traces of oxygen, *Journal of Chemical Physics*, *75*, 681–689, 1981.

McPeters, R. D., A nitric oxide increase observed following the July 1982 solar proton event, *Geophysical Research Letters*, *13*, 667–670, 1986.

McPeters, R. D. and Jackman, C. H., The response of Ozone to Solar Proton Events During Solar Cycle 21: The Observations, *Journal of Geophysical Research*, *90*, 7945–7954, 1985.

Minschwaner, K. and Siskind, D. E., A New Calculation of Nitric Oxide Photolysis in the Stratosphere, Mesosphere, and Lower Thermosphere, *Journal of Geophysical Research*, *98*, 20 401–20 412, 1993.

Murtagh, D. P., The O_2 Schumann-Runge system - New calculations of photodissociation cross-sections, *Planetary and Space Science*, *36*, 819–828, 1988.

Natarajan, M., Remsberg, E. E., Deaver, L. E., and Russell, J. M., Anomalously high levels of NO_x in the polar upper stratosphere during April, 2004: Photochemical consistency of HALOE observations, *Geophysical Research Letters*, *31*, L15 113, 2004.

Ohshio, M., Maeda, R., and Sakagami, H., Height distribution of local photoionization efficiency, *Journal of the Radio Research Laboratory*, *13*, 245, 1966.

Orsolini, Y. J., Manney, G. L., Santee, M. L., and Randall, C. E., An upper stratospheric layer of enhanced HNO_3 following exceptional solar storms, *Geophysical Research Letters*, *32*, L12S01, 2005.

Peterson, J. R., Sunlight photodestruction of CO_3^-, its hydrate, and O_3^- - The importance of photodissociation to the D region electron densities at sunrise, *Journal of Geophysical Research*, *81*, 1433–1435, 1976.

Plane, J. M. C., Cox, R. M., and Rollason, R. J., Metallic layers in the mesopause and lower thermosphere region, *Advances in Space Research*, *24*, 1559–1570, 1999.

Porter, H. S., Jackman, C. H., and Green, A. E. S., Efficiencies for production of atomic nitrogen and oxygen by relativistic proton impact in air, *Journal of Chemical Physics*, *65*, 154–167, 1976.

Press, W. H., Teukolsky, S. A., Vetterling, W. T., and Flannery, B. P., *Numerical Recipes in FORTRAN, The Art of Scientific Computing*, Clarendon Press, Oxford, 1992.

Randall, C. E., Siskind, D. E., and Bevilacqua, R. M., Stratospheric NO_x enhancements in the southern hemisphere vortex in winter/spring of 2000, *Geophysical Research Letters*, *28*, 2385–2388, 2001.

Randall, C. E., Harvey, V. L., Manney, G. L., Orsolini, Y., Codrescu, M., Sioris, C., Brohede, S., Haley, C. S., Gordley, L. L., Zawodny, J. M., and Russell, J. M., Stratospheric effects of energetic particle precipitation in 2003-2004, *Geophysical Research Letters*, *32*, L05 802, 2005.

Ranta, H., Ranta, A., Rosenberg, T. J., and Detrick, D. L., Autumn and winter anomalies in ionospheric absorption as measured by riometers, *Journal of Atmospheric and Terrestrial Physics*, *45*, 193–202, 1983.

Reagan, J. B. and Watt, T. M., Simultaneous satellite and radar studies of the D region ionosphere during the intense solar particle events of August 1972, *Journal of Geophysical Research*, *81*, 4579–4596, 1976.

Rees, M. H., On the interaction of auroral protons with the earth's atmosphere, *Planetary and Space Science*, *30*, 463–472, 1982.

Rees, M. H., *Physics and chemistry of the upper atmosphere*, Cambridge atmospheric and space science series, Cambridge University Press, Cambridge, UK, 1989.

Reid, G. C., A study of the enhanced ionization produced by solar protons during a polar cap absorbtion event, *Journal of Geophysical Research*, *66*, 4071–4085, 1961.

Reid, G. C., Radar observations of negative-ion photodetachment at sunrise in the auroral-zone mesosphere, *Planetary and Space Science*, *35*, 27–37, 1987.

Reid, G. C. and Collins, C., Observations of abnormal VHF radio wave absortion at medium and high latitudes, *Journal of Atmospheric and Terrestrial Physics*, *14*, 68–81, 1959.

Reid, G. C., Solomon, S., and Garcia, R. R., Response of the middle atmosphere to the solar proton events of August-December, 1989, *Geophysical Research Letters*, *18*, 1019–1022, 1991.

Rohen, G., Savigny, C. v., Sinnhuber, M., Llewellyn, E. J., Kaiser, J. W., Jackman, C. H., Kallenrode, M.-B., Schröter, J., Eichmann, K.-U., Bovensmann, H., and Burrows, J. P., Ozone deplection during the solar proton events of October/November 2003 as seen by SCIAMACHY, *Journal of Geophysical Research*, *110*, A09S39, 2005.

Rusch, D. W., Gérard, J.-C., Solomon, S., Crutzen, P. J., and Reid, G. C., The effect of particle precipitation events on the neutral and ion chemistry of the middle atmosphere – I. Odd nitrogen, *Planetary and Space Science*, *29*, 767–774, 1981.

Sander, S. P., Friedl, R. R., Golden, D. M., Kurylo, M. J., Huie, R. E., Orkin, V. L., Moortgat, G. K., Ravishankara, A. R., Kolb, C. E., Molina, M. J., and Finlayson-Pitts, B. J., *Chemical Kinetics and Photochemical Data for Use in Stratospheric Modeling: Evaluation number 14*, JPL Publication 02-25, Jet Propulsion Laboratory, California Institute of Technology, Pasadena, USA, 2003.

Schröter, J., Heber, B., Steinhilber, F., and Kallenrode, M., Energetic particles in the atmosphere: A Monte-carlo simulation, *Advances in Space Research*, in press, 2005.

Sen, H. K. and Wyller, A. A., On the generalization of the Appleton-Hartree magnetoionic formulas, *Journal of Geophysical Research*, *65*, 3931–3950, 1960.

Shimazaki, T., Effective eddy diffusion coefficient and atmospheric composition in the lower thermosphere, *Journal of Atmospheric and Terrestrial Physics*, *33*, 1383, 1971.

Shimazaki, T., *Minor Constituents in the Middle Atmosphere (Developments in Earth and Planetary Physics, No 6)*, D. Reidel Publishing Co., Dordrecht, Holland, 1984.

Sinnhuber, M., Burrows, J. P., Chipperfield, M. P., Jackman, C. H., Kallenrode, M.-B., Künzi, K. F., and Quack, M., A model study of the impact of magnetic field structure on atmospheric composition during solar proton events, *Geophysical Research Letters*, *30*, ASC10, 2003.

Siskind, D. E., Strickland, D. J., Meier, R. R., Majeed, T., and Eparvier, F. G., On the relationship between the solar soft X ray flux and thermospheric nitric oxide: An update with an improved photoelectron model, *Journal of Geophysical Research*, *100*, 19 687–19 694, 1995.

Siskind, D. E., Bacmeister, J. T., Summers, M. E., and Russell, J. M., Two-dimensional Model Calculations of Nitric Oxide Transport in the Middle Atmosphere and Comparison with Halogen Occultation Experiment Data, *Journal of Geophysical Research*, *102*, 3527–3545, 1997.

Smart, D. F. and Shea, M. A., The space-developed dynamic vertical cutoff rigidity model and its applicability to aircraft radiation dose, *Advances in Space Research*, *32*, 103–108, 2003.

Smith, A. K., Physics and chemistry of the mesopause region, *Journal of Atmospheric and Solar-Terrestrial Physics*, *66*, 839–857, 2004.

Solomon, S., Stratospheric ozone depletion: a review of concepts and history, *Reviews of Geophysics*, *37*, 275–316, 1999.

Solomon, S., Rusch, D. W., Gérard, J.-C., Reid, G. C., and Crutzen, P. J., The effect of particle precipitation events on the neutral and ion chemistry of the middle atmosphere: II. Odd hydrogen, *Planetary and Space Science*, *8*, 885–893, 1981.

Solomon, S., Crutzen, P. J., and Roble, R. G., Photochemical coupling between the thermosphere and the lower atmosphere 1. Odd nitrogen from 50 to 120 km, *Journal of Geophysical Research*, *87*, 7206–7220, 1982.

Solomon, S., Reid, G. C., Rusch, D. W., and Thomas, R. J., Mesospheric ozone depletion during the solar proton event of July 13, 1982 Part II. Comparions between theory and measurements, *Geophysical Research Letters*, *10*, 257–260, 1983.

Størmer, C., Periodische Elektronenbahnen im Feld eines Elementramagnetron und ihre Anwendung auf Bruches Modellversuche und auf Eschenhagens Elementarwellen des Erdmagnetismus, *Zeitschrift für Astrophysik*, *1*, 237–274, 1930.

Swider, W. and Keneshea, T., Decrease of ozone and atomic oxygen in the lower mesosphere during a PCA event, *Planetary and Space Science*, *21*, 1969–1973, 1973.

Thomas, L. and Bowman, M. R., A study of pre-sunrise changes in negative ions and electrons in the D-region, *Journal of Atmospheric and Terrestrial Physics*, *4*, 219, 1986.

Thomas, R. J., Barth, C. A., Rottman, G. J., Rusch, D. W., Mount, G. H., Lawrence, G. M., Sanders, R. W., Thomas, G. E., and Clemens, L. E., Mesospheric ozone depletion during the solar proton event of July 13, 1982 Part I: Measurement, *Geophysical Research Letters*, *10*, 253–255, 1983.

Tobiska, W. K., Woods, T., Eparvier, F., Viereck, R., Floyd, L. D. B., Rottman, G., and White, O. R., The SOLAR2000 empirical solar irradiance model and forecast tool, *Journal of Atmospheric and Terrestrial Physics*, *62*, 1233–1250, 2000.

Torr, M. A., Torr, D. G., and Ong, R. A., Ionization frequencies for major thermospheric constituents as a function of solar cycle 21, *Geophysical Research Letters*, *6*, 771–774, 1979.

Turunen, E., EISCAT incoherent scatter radar observations and model studies of day to twilight variations in the D region during the PCA event of August 1989, *Journal of Atmospheric and Terrestrial Physics*, *55*, 767–781, 1993.

Turunen, E., Matveinen, H., Tolvanen, J., and Ranta, H., D-region ion chemistry model, in *STEP Handbook of Ionospheric Models*, edited by R. W. Schunk, pp. 1–25, SCOSTEP Secretariat, Boulder, Colorado, USA, 1996.

Verronen, P. T., Turunen, E., Ulich, T., and Kyrölä, E., New possibilities for studying ozone destruction by odd nitrogen in the middle atmosphere through GOMOS and MIPAS measurements, in *ESAMS99, European Symposium on Atmospheric Measurements from Space*, vol. WPP-161, pp. 607–610, European Space Agency, ESTEC, Noordwijk, Netherlands, 1999.

Vitt, F. M. and Jackman, C. H., A comparison of sources of odd nitrogen production from 1974 through 1993 in the Earth's middle atmosphere as calculated using a two-dimensional model, *Journal of Geophysical Research*, *101*, 6729–6740, 1996.

Weeks, L. H., Cuikay, R. S., and Corbin, J. R., Ozone Measurements in the Mesosphere During The Solar Proton Event of 2 November 1969, *Journal of the Atmospheric Sciences*, *29*, 1138–1142, 1972.

Westerlund, S., Reder, F. H., and Abom, C., Effects of polar cap absorption events on VLF transmissions, *Planetary and Space Science*, *17*, 1329–1374, 1969.

WMO, *Global ozone research and monitoring project - Report no. 16: Atmospheric Ozone 1985*, World Meteorological Organization, Geneva, Switzerland, 1985.

Zadorozhny, A. M., Tuchkov, G. A., Kikthenko, V. N., Laštovička, J., Boška, J., and Novák, A., Nitric oxide and lower ionosphere quantities during solar particle events of October 1989 after rocket and ground-based measurements, *Journal of Atmospheric and Terrestrial Physics*, *54*, 183–192, 1992.

Zadorozhny, A. M., Kikhtenko, V. N., Kokin, G. A., Tuchkov, G. A., Tyutin, A. A., Chizhov, A. F., and Shtirkov, O. V., Middle atmosphere response to the solar proton events of October 1989 using the results of rocket measurements, *Journal of Geophysical Research*, *99*, 21 059–21 069, 1994.

Zipf, E. C., Espy, P. J., and Boyle, C. F., The Excitation and Collisional Deactivation of Metastable N(^{2}P) Atoms in Auroras, *Journal of Geophysical Research*, *85*, 687–694, 1980.

Appendix: Tables of photochemical reactions

The following tables list the photochemical reactions currently included in the Sodankylä Ion and Neutral Chemistry model. Notation: M is any atmospheric molecule, T is temperature, and P is pressure. X^- and X^+ is any negative and positive ion, respectively. Units: reaction rate coefficients are given in either s^{-1}, $cm^3\ s^{-1}$, or $cm^6\ s^{-1}$, as appropriate for the reaction shown.

Table A.1 Modelled ions and minor neutrals.

O, $O(^1D)$, $O_2(^1\Delta_g)$, O_3
N, $N(^2D)$, NO, NO_2, NO_3, HNO_3, N_2O_5
H, OH, HO_2, H_2O_2
O^+, O_2^+, O_4^+, $O_2^+(H_2O)$, $O_2^+N_2$, $O_2^+CO_2$, $O_2^+(H_2O)N_2$, $O_2^+(H_2O)CO_2$, $O_2^+(H_2O)_2$
N^+, N_2^+, NO^+, $NO^+(N_2)$, $NO^+(CO_2)$, $NO^+(H_2O)$, $NO^+(H_2O)_2$, $NO^+(H_2O)_3$, $NO^+(H_2O)(N_2)$,
$NO^+(H_2O)(CO_2)$, $NO^+(H_2O)_2(N_2)$, $NO^+(H_2O)_2(CO_2)$
$H^+(H_2O)$, $H^+(H_2O)_2$, $H^+(H_2O)_3$, $H^+(H_2O)_4$, $H^+(H_2O)_5$, $H^+(H_2O)_6$, $H^+(H_2O)_7$, $H^+(H_2O)_8$
$H_3O^+(OH)$, $H_3O^+(OH)H_2O$, $H_3O^+(OH)CO_2$, $H^+(H_2O)_2(CO_2)$, $H^+(H_2O)_2N_2$, $H^+(H_2O)CO_2$, $H^+(H_2O)N_2$
O^-, O_2^-, O_3^-, O_4^-, $O^-(H_2O)$, $O_2^-(H_2O)$, $O_2^-(H_2O)_2$, $O_3^-(H_2O)$
OH^-, $OH^-(H_2O)$,
CO_3^-, CO_4^-, $CO_3^-(H_2O)$, $CO_3^-(H_2O)_2$, HCO_3^-
NO_2^-, NO_3^-, NO_3^-(*), $NO_3^-(H_2O)$, $NO_2^-(H20)$, $NO_3^-(H_20)_2$, $NO_3^-(HNO_3)$, $NO_3^-(HNO_3)_2$, $NO_3^-(HCl)$
Cl^-, ClO^-, $Cl^-(H_2O)$, $Cl^-(CO_2)$, $Cl^-(HCl)$

Table A.2 Photoionisation reactions.

$N_2 + h\nu$	→	$N_2^+ + e$	[Torr et al., 1979; Siskind et al., 1995]
– " –	→	$N^+ + N/N(^2D) + e$	– " –
$O_2 + h\nu$	→	$O_2^+ + e$	[Torr et al., 1979; Siskind et al., 1995]
– " –	→	$O^+ + O + e$	– " –
$NO + h\nu$	→	$NO^+ + e$	[Ohshio et al., 1966]
$O_2(^1\Delta_g) + h\nu$	→	$O_2^- + e$	[Torr et al., 1979]
$O + h\nu$	→	$O^+ + O + e$	[Torr et al., 1979]

Table A.3 Photodissociation reactions.

$O_2 + h\nu$	→	$O + O$	Shimazaki [1984]; WMO [1985]; Murtagh [1988]; Koppers and Murtagh [1996]
– " –	→	$O + O(^1D)$	– " –
$O_3 + h\nu$	→	$O_2 + O$	Shimazaki [1984]; WMO [1985]; DeMore et al. [1992]; Brasseur and Solomon [2005]
– " –	→	$O_2(^1\Delta_g) + O(^1D)$	– " –
$N_2 + h\nu$	→	$N + N(^2D)$	Rees [1989]
$NO + h\nu$	→	$N + O$	[Minschwaner and Siskind, 1993]
$NO_2 + h\nu$	→	$NO + O$	Shimazaki [1984]; DeMore et al. [1992]
$NO_3 + h\nu$	→	$NO_2 + O$	Sander et al. [2003]
– " –	→	$NO + O_2$	– " –
$HNO_3 + h\nu$	→	$NO_2 + OH$	DeMore et al. [1992]
$N_2O_5 + h\nu$	→	$NO_2 + NO_3$	DeMore et al. [1992]
– " –	→	$O + NO + NO_3$	– " –
$H_2O + h\nu$	→	$OH + H$	Shimazaki [1984]; DeMore et al. [1992]
– " –	→	$O(^1D) + H_2$	– " –
$H_2O_2 + h\nu$	→	$OH + OH$	Sander et al. [2003]

Table A.4 Positive ion reactions. The sources of reaction rate coefficients are given in Turunen et al. [1996], except † which is taken from Matsuoka et al. [1981].

$O^+ + O_2$	→	$O_2^+ + O$	$1.5 \times 10^{-11} \times (300/T)$	
$O^+ + N_2$	→	$NO^+ + N$	$1.2 \times 10^{-12} \times (300/T)$	
$O^+ + N(^2D)$	→	$N^+ + O$	1.3×10^{-10}	
$O^+ + NO$	→	$NO^+ + O$	8×10^{-13}	
$O_2^+ + NO$	→	$NO^+ + O_2$	4.4×10^{-10}	
$O_2^+ + N_2$	→	$NO^+ + NO$	2×10^{-18}	†
$O_2^+ + O_2 + M$	→	$O_4^+ + M$	$4.0 \times 10^{-30} \times (300/T)^{2.93}$	
$O_2^+ + H_2O + M$	→	$O_2^+(H_2O) + M$	2.8×10^{-28}	
$O_2^+ + N_2 + M$	→	$O_2^+N_2 + M$	$1.0 \times 10^{-30} \times (300/T)^{3.2}$	
$O_2^+ + N$	→	$NO^+ + O$	1.2×10^{-10}	
$O_2^+ + N(^2D)$	→	$N^+ + O_2$	2.5×10^{-10}	
$O_2^+(H_2O) + H_2O$	→	$H_3O^+(OH) + O_2$	9.0×10^{-10}	
$O_2^+(H_2O) + H_2O$	→	$H^+(H_2O) + OH + O_2$	2.4×10^{-10}	
$O_2^+(H_2O) + N_2 + M$	→	$O_2^+(H_2O)N_2 + M$	1×10^{-27}	
$O_2^+(N_2) + O_2$	→	$O_4^+ + N_2$	5×10^{-10}	
$O_2^+(N_2) + M$	→	$O_2^+ + N_2 + M$	$1.7 \times 10^{-7} \times (300/T)^{3.2} \times e^{-2676/T}$	
$O_2^+(N_2) + CO_2$	→	$O_2^+(CO_2) + N_2$	10^{-9}	
$O_2^+CO_2 + H_2O$	→	$O_2^+(H_2O) + CO_2$	1.1×10^{-9}	
$O_2^+(H_2O)N_2 + CO_2$	→	$O_2^+(H_2O)CO_2 + N_2$	1.5×10^{-10}	
$O_2^+(H_2O)N_2 + M$	→	$O_2^+(H_2O) + N_2 + M$	7.7×10^{-13}	
$O_2^+(H_2O)CO_2 + H_2O$	→	$O_2^+(H_2O)_2 + CO_2$	5×10^{-10}	
$O_2^+(H_2O)CO_2 + H_2O$	→	$H_3O^+(OH)CO_2 + O_2$	5×10^{-10}	
$O_2^+(H_2O)_2 + H_2O$	→	$H_3O^+(OH)H_2O + O_2$	1.3×10^{-9}	
$O_4^+ + O_2(^1\Delta_g)$	→	$O_2^+ + 2O_2$	1.5×10^{-10}	
$O_4^+ + H_2O$	→	$O_2^+(H_2O) + O_2$	1.7×10^{-9}	
$O_4^+ + O$	→	$O_2^+ + O_3$	3×10^{-10}	
$O_4^+ + M$	→	$O_2^+ + O_2 + M$	$2.8 \times 10^{-5} \times (300/T)^{3.93} \times e^{-5400/T}$	
$N^+ + O_2$	→	$NO^+ + O$	2.6×10^{-10}	
$N^+ + O_2$	→	$O_2^+ + N$	1.1×10^{-10}	
$N^+ + O_2$	→	$O^+ + NO$	3.0×10^{-11}	
$N^+ + O$	→	$O^+ + N$	5.0×10^{-13}	
$N^+ + O_2$	→	$O_2^+ + N(^2D)$	2.0×10^{-10}	
$N_2^+ + O$	→	$NO^+ + N(^2D)$	$1.4 \times 10^{-10} \times (300/T)^{0.44}$	
$N_2^+ + O$	→	$O^+ + N_2$	$9.8 \times 10^{-12} \times (300/T)^{0.23}$	
$N_2^+ + O_2$	→	$O_2^+ + N_2$	$5 \times 10^{-11} \times (300/T)^{0.8}$	
$N_2^+ + NO$	→	$NO^+ + N_2$	3.3×10^{-10}	
$NO^+ + N_2 + M$	→	$NO^+(N_2) + M$	$3.0 \times 10^{-31} \times (300/T)^{4.3}$	
$NO^+ + CO_2 + M$	→	$NO^+(CO_2) + M$	$1.4 \times 10^{-29} \times (300/T)^4$	
$NO^+ + H_2O + M$	→	$NO^+(H_2O) + M$	$1.8 \times 10^{-28} \times (308/T)^{4.7}$	
$NO^+(N_2) + CO_2$	→	$NO^+(CO_2) + N_2$	10^{-9}	
$NO^+(N_2) + H_2O$	→	$NO^+(H_2O) + N_2$	10^{-9}	
$NO^+(N_2) + M$	→	$NO^+ + N_2 + M$	$1.5 \times 10^{-8} \times (300/T)^{4.3} \times e^{-2093/T}$	
$NO^+(CO_2) + H_2O$	→	$NO^+(H_2O) + CO_2$	10^{-9}	
$NO^+(CO_2) + M$	→	$NO^+ + CO_2 + M$	$3.1 \times 10^4 \times T^{-4} \times e^{-4590/T}$	
$NO^+(H_2O) + HO_2$	→	$H^+(H_2O) + NO_3$	0.5×10^{-9}	
$NO^+(H_2O) + OH$	→	$H^+(H_2O) + NO_2$	10^{-10}	
$NO^+(H_2O) + H$	→	$H^+(H_2O) + NO$	7×10^{-12}	
$NO^+(H_2O) + H_2O + M$	→	$NO^+(H_2O)_2 + M$	$1 \times 10^{-27} \times (308/T)^{4.7}$	
$NO^+(H_2O) + N_2 + M$	→	$NO^+(H_2O)(N_2) + M$	$2 \times 10^{-31} \times (300/T)^{4.4}$	
$NO^+(H_2O) + CO_2 + M$	→	$NO^+(H_2O)(CO_2) + M$	$7 \times 10^{-30} \times (300/T)^5$	
$NO^+(H_2O)_2 + H_2O + M$	→	$NO^+(H_2O)_3 + M$	$1.0 \times 10^{-27} \times (308/T)^{4.7}$	
$NO^+(H_2O)_2 + N_2 + M$	→	$NO^+(H_2O)_2(N_2) + M$	$2 \times 10^{-31} \times (300/T)^{4.4}$	
$NO^+(H_2O)_2 + CO_2 + M$	→	$NO^+(H_2O)_2(CO_2) + M$	$7 \times 10^{-30} \times (300/T)^3$	
$NO^+(H_2O)_3 + H_2O$	→	$H^+(H_2O)_3 + HNO_2$	7×10^{-11}	
$NO^+(H_2O)(N_2) + H_2O$	→	$NO^+(H_2O)_2 + N_2$	10^{-9}	
$NO^+(H_2O)(N_2) + CO_2$	→	$NO^+(H_2O)(CO_2) + N_2$	10^{-9}	
$NO^+(H_2O)(N_2) + M$	→	$NO^+(H_2O) + N_2 + M$	$1.5 \times 10^6 \times T^{-5.4} \times e^{-2150/T}$	
$NO^+(H_2O)(CO_2) + H_2O$	→	$NO^+(H_2O)_2 + CO_2$	10^{-9}	
$NO^+(H_2O)(CO_2) + M$	→	$NO^+(H_2O) + CO_2 + M$	$3.8 \times 10^{-6} \times (300/T)^5 \times e^{-4025/T}$	
$NO^+(H_2O)_2(N_2) + H_2O$	→	$NO^+(H_2O)_3 + N_2$	1.0×10^{-9}	
$NO^+(H_2O)_2(N_2) + CO_2$	→	$NO^+(H_2O)_2(CO_2) + N_2$	10^{-9}	
$NO^+(H_2O)_2(N_2) + M$	→	$NO^+(H_2O)_2 + N_2 + M$	$1.5 \times 10^6 \times T^{-5.4} \times e^{-1800/T}$	
$NO^+(H_2O)_2(CO_2) + H_2O$	→	$NO^+(H_2O)_3 + CO_2$	10^{-9}	
$NO^+(H_2O)_2(CO_2) + M$	→	$NO^+(H_2O)_2 + CO_2 + M$	$3.8 \times 10^{-6} \times (300/T)^5 \times e^{-3335/T}$	
$H^+(H_2O) + H_2O + M$	→	$H^+(H_2O)_2 + M$	$4.6 \times 10^{-27} \times (300/T)^4$	
$H^+(H_2O) + CO_2 + M$	→	$H^+(H_2O)CO_2 + M$	$8.5 \times 10^{-28} \times (300/T)^{4.0}$	
$H^+(H_2O) + N_2 + M$	→	$H^+(H_2O)N_2 + M$	$3.5 \times 10^{-31} \times (300/T)^{4.0}$	
$H^+(H_2O)_2 + M$	→	$H^+(H_2O) + H_2O + M$	$2.5 \times 10^{-2} \times (300/T)^5 \times e^{-15900/T}$	
$H^+(H_2O)_2 + H_2O + M$	→	$H^+(H_2O)_3 + M$	$8.6 \times 10^{-27} \times (300/T)^{7.5}$	
$H^+(H_2O)_2 + CO_2 + M$	→	$H^+(H_2O)_2(CO_2) + M$	$8.5 \times 10^{-28} \times (300/T)^{4.0}$	
$H^+(H_2O)_2 + N_2 + M$	→	$H^+(H_2O)_2N_2 + M$	$3.5 \times 10^{-31} \times (300/T)^{4.0}$	
$H^+(H_2O)_3 + M$	→	$H^+(H_2O)_2 + H_2O + M$	$1.2 \times 10^{-2} \times (300/T)^{8.5} \times e^{-9800/T}$	
$H^+(H_2O)_3 + H_2O + M$	→	$H^+(H_2O)_4 + M$	$3.6 \times 10^{-27} \times (300/T)^{8.1}$	

$H^+(H_2O)_4 + M$	→	$H^+(H_2O)_3 + H_2O + M$	$1.5 \times 10^{-1} \times (300/T)^{9.1} \times e^{-9000/T}$
$H^+(H_2O)_4 + H_2O + M$	→	$H^+(H_2O)_5 + M$	$4.6 \times 10^{-28} \times (300/T)^{14}$
$H^+(H_2O)_5 + M$	→	$H^+(H_2O)_4 + H_2O + M$	$1.7 \times 10^{-3} \times (300/T)^{15} \times e^{-6400/T}$
$H^+(H_2O)_5 + H_2O + M$	→	$H^+(H_2O)_6 + M$	$5.8 \times 10^{-29} \times (300/T)^{15.3}$
$H^+(H_2O)_6 + M$	→	$H^+(H_2O)_5 + H_2O + M$	$4.0 \times 10^{-3} \times (300/T)^{16.3} \times e^{-5800/T}$
$H^+(H_2O)_6 + H_2O + M$	→	$H^+(H_2O)_7 + M$	$9 \times 10^{-28} \times (300/T)^{15.3}$
$H^+(H_2O)_7 + M$	→	$H^+(H_2O)_6 + H_2O + M$	$1.3 \times 10^{-2} \times (300/T)^{16.3} \times e^{-5400/T}$
$H^+(H_2O)_7 + H_2O + M$	→	$H^+(H_2O)_8 + M$	$9 \times 10^{-28} \times (300/T)^4$
$H^+(H_2O)_8 + M$	→	$H^+(H_2O)_7 + H_2O + M$	$2.3 \times 10^{1}0 \times T^{-5} \times e^{-5000/T}$
$H^+(H_2O)_2(CO_2) + H_2O$	→	$H^+(H_2O)_3 + CO_2$	1.0×10^{-9}
$H^+(H_2O)_2(CO_2) + M$	→	$H^+(H_2O)_2 + CO_2 + M$	$1.0 \times 10^{-3} \times (300/T)^{5.0} \times e^{-6200/T}$
$H^+(H_2O)_2N_2 + CO_2$	→	$H^+(H_2O)_2(CO_2) + N_2$	1×10^{-9}
$H^+(H_2O)_2N_2 + M$	→	$H^+(H_2O)_2 + N_2 + M$	$1.2 \times 10^{-8} \times (300/T)^{5.4} \times e^{-2700/T}$
$H^+(H_2O)_2N_2 + H_2O$	→	$H^+(H_2O)_3 + N_2$	$1.2 \times 10^{-8} \times (300/T)^{5.4} \times e^{-2700/T}$
$H^+(H_2O)CO_2 + H_2O$	→	$H^+(H_2O)_2 + CO_2$	1×10^{-9}
$H^+(H_2O)CO_2 + M$	→	$H^+(H_2O) + CO_2 + M$	$5.5 \times 10^{-3} \times (300/T)^{5.0} \times e^{-7700/T}$
$H^+(H_2O)N_2 + CO_2$	→	$H^+(H_2O)CO_2 + N_2$	1×10^{-9}
$H^+(H_2O)N_2 + M$	→	$H^+(H_2O) + N_2 + M$	$1.0 \times 10^{-8} \times (300/T)^{5.4} \times e^{-2800/T}$
$H_3O^+(OH) + H_2O$	→	$H^+(H_2O)_2 + OH$	2.0×10^{-9}
$H_3O^+(OH) + O_2 + M$	→	$O_2^+(H_2O)_2 + M$	$3 \times 10^{-30} \times (293/T)^4$
$H_3O^+(OH)H_2O + H_2O$	→	$H^+(H_2O)_3 + OH$	1.9×10^{-9}
$H_3O^+(OH)CO_2 + H_2O$	→	$H^+(H_2O)_2(CO_2) + OH$	5×10^{-10}
$H_3O^+(OH)CO_2 + H_2O$	→	$H^+(H_2O)_2 + OH + CO_2$	5×10^{-10}

Table A.5 Recombination of positive ions with electrons. The sources of reaction rate coefficients are given in Turunen et al. [1996].

$O^+ + e$	→	O	$4.0 \times 10^{-12} \times (300/T)^{0.7}$
$O_2^+ + e$	→	2O	$1.6 \times 10^{-7} \times (300/T)^{0.625}$
$O_4^+ + e$	→	$2O_2$	$4.2 \times 10^{-6} \times (300/T)^{0.5}$
$N^+ + e$	→	N	1.0×10^{-12}
$N_2^+ + e$	→	$N + N(^2D)$	$1.8 \times 10^{-7} \times (300/T)^{0.39}$
$NO^+ + e$	→	$N/N(^2D) + O$	$4.2 \times 10^{-7} \times (300/T)^{0.85}$
$NO^+(N_2) + e$	→	$NO + N_2$	$1.4 \times 10^{-6} \times (300/T)^{0.4}$
$NO^+(CO_2) + e$	→	$NO + CO_2$	1.5×10^{-6}
$NO^+(H_2O) + e$	→	$NO + H_2O$	1.5×10^{-6}
$NO^+(H_2O)_2 + e$	→	$NO + 2H_2O$	2.0×10^{-6}
$NO^+(H_2O)_3 + e$	→	$NO + 3H_2O$	2.0×10^{-6}
$NO^+(H_2O)(N_2) + e$	→	$NO + H_2O + N_2$	3.0×10^{-6}
$NO^+(H_2O)(CO_2) + e$	→	$NO + H_2O + CO_2$	3.0×10^{-6}
$NO^+(H_2O)_2(N_2) + e$	→	$NO + 2H_2O + N_2$	3.0×10^{-6}
$NO^+(H_2O)_2(CO_2) + e$	→	$NO + 2H_2O + CO_2$	3.0×10^{-6}
$O_2^+(H_2O) + e$	→	$O_2 + H_2O$	2.0×10^{-6}
$H_3O^+(OH) + e$	→	$OH + H + H_2O$	1.5×10^{-6}
$H^+(H_2O) + e$	→	$H + H_2O$	$6.3 \times 10^{-7} \times (300/T)^{0.5}$
$H^+(H_2O)_2 + e$	→	$H + 2H_2O$	$2.5 \times 10^{-6} \times (300/T)^{0.1}$
$H^+(H_2O)_3 + e$	→	$H + 3H_2O$	$3.0 \times 10^{-6} \times (300/T)^{0.1}$
$H^+(H_2O)_4 + e$	→	$H + 4H_2O$	3.6×10^{-6}
$H^+(H_2O)_5 + e$	→	$H + 5H_2O$	5.0×10^{-6}
$H^+(H_2O)_6 + e$	→	$H + 6H_2O$	5.0×10^{-6}
$H^+(H_2O)_7 + e$	→	$H + 7H_2O$	4×10^{-6}
$H^+(H_2O)_8 + e$	→	$H + 8H_2O$	1.0×10^{-5}
$H^+(H_2O)_2(CO_2) + e$	→	$H + 2H_2O + CO_2$	3×10^{-6}
$H^+(H_2O)_2N_2 + e$	→	$H + 2H_2O + N_2$	1.5×10^{-6}
$H^+(H_2O)CO_2 + e$	→	$H + H_2O + CO_2$	1.5×10^{-6}

Table A.6 Positive ion photodissociation. The source of reaction rate coefficient is given in Turunen et al. [1996].

$O_2^+(H_2O) + h\nu$	→	$O_2^+ + H_2O$	0.42

Table A.7 Electron attachment on neutrals. The sources of reaction rate coefficients are given in Turunen et al. [1996].

$O_2 + N_2 + e$	$\rightarrow$	$O_2^- + N_2$	$10^{-31} \times (300/T) \times e^{-600/T}$
$O_3 + e$	$\rightarrow$	$O^- + O_2$	$9.1 \times 10^{-12} \times (300/T)^{-1.46}$
$2O_2 + e$	$\rightarrow$	$O_2^- + O_2$	$4 \times 10^{-30} \times e^{-193/T}$

Table A.8 Negative ion reactions. The sources of reaction rate coefficients are given in Kazil [2002].

$O^- + O_3$	$\rightarrow$	$O_3^- + O$	8.0×10^{-10}
$O^- + 2O_2$	$\rightarrow$	$O_3^- + O_2$	1.4×10^{-30}
$O^- + H_2O$	$\rightarrow$	$OH^- + OH$	6.0×10^{-13}
$O^- + NO_2$	$\rightarrow$	$NO_2^- + O$	1.0×10^{-9}
$O^- + CO_2 + M$	$\rightarrow$	$CO_3^- + M$	2.0×10^{-28}
$O^- + H_2$	$\rightarrow$	$OH^- + H$	3.2×10^{-11}
$O^- + HCl$	$\rightarrow$	$Cl^- + OH$	2.7×10^{-9}
$O^- + Cl$	$\rightarrow$	$Cl^- + O_2$	1.0×10^{-10}
$O^- + ClO$	$\rightarrow$	$Cl^- + O_2$	1.0×10^{-10}
$O^- + CH_4$	$\rightarrow$	$OH^- + CH_3$	1.0×10^{-10}
$O^- + HNO_3$	$\rightarrow$	$NO_3^- + OH$	3.6×10^{-9}
$O^- + H_2O + M$	$\rightarrow$	$O^-(H_2O) + M$	1.3×10^{-28}
$O^-(H_2O) + O_2$	$\rightarrow$	$O_3^- + H_2O$	6.2×10^{-11}
$O_2^- + O$	$\rightarrow$	$O^- + O_2$	1.5×10^{-10}
$O_2^- + O_3$	$\rightarrow$	$O_3^- + O_2$	7.8×10^{-10}
$O_2^- + CO_2 + O_2$	$\rightarrow$	$CO_4^- + O_2$	4.7×10^{-29}
$O_2^- + NO_2$	$\rightarrow$	$NO_2^- + O_2$	7×10^{-10}
$O_2^- + O_2 + M$	$\rightarrow$	$O_4^- + M$	3.4×10^{-31}
$O_2^- + H_2O + M$	$\rightarrow$	$O_2^-(H_2O) + M$	2.2×10^{-28}
$O_2^- + HCl$	$\rightarrow$	$Cl^- + HO_2$	2.0×10^{-9}
$O_2^- + Cl$	$\rightarrow$	$Cl^- + O_2$	1.0×10^{-10}
$O_2^- + ClO$	$\rightarrow$	$ClO^- + O_2$	1.0×10^{-10}
$O_2^- + HNO_3$	$\rightarrow$	$NO_3^- + HO_2$	2.9×10^{-9}
$O_2^-(H_2O) + CO_2$	$\rightarrow$	$CO_4^- + H_2O$	5.8×10^{-10}
$O_2^-(H_2O) + NO$	$\rightarrow$	$NO_3^- + H_2O$	2.0×10^{-10}
$O_2^-(H_2O) + O_3$	$\rightarrow$	$O_3^- + O_2 + H_2O$	8.0×10^{-10}
$O_2^-(H_2O) + H_2O + M$	$\rightarrow$	$O_2^-(H_2O)_2 + M$	5.4×10^{-28}
$O_2^-(H_2O) + NO_2$	$\rightarrow$	$NO_2^- + H_2O + O_2$	9.0×10^{-10}
$O_2^-(H_2O) + M$	$\rightarrow$	$O_2^- + H_2O + M$	$1.33 \times 10^{-4} \times (300/T) \times e^{-9261/T}$
$O_2^-(H_2O)_2 + M$	$\rightarrow$	$O_2^-(H_2O) + H_2O + M$	$4.0 \times 10^{-10} \times (300/T) \times e^{-8660/T}$
$O_2^-(H_2O)_2 + NO_2$	$\rightarrow$	$NO_2^-(H_20) + H_2O + O_2$	9.0×10^{-10}
$O_2^-(H_2O)_2 + O_3$	$\rightarrow$	$O_3^-(H_2O) + H_2O + O_2$	7.8×10^{-10}
$O_3^- + O$	$\rightarrow$	$O_2^- + O_2$	2.5×10^{-10}
$O_3^- + H$	$\rightarrow$	$OH^- + O_2$	8.4×10^{-10}
$O_3^- + CO_2$	$\rightarrow$	$CO_3^- + O_2$	5.5×10^{-10}
$O_3^- + NO$	$\rightarrow$	$NO_3^- + O$	$1.05 \times 10^{-12} \times (300/T)^{2.15}$
$O_3^- + NO_2$	$\rightarrow$	$NO_3^- + O_2$	$2.50 \times 10^{-11} \times (300/T)^{0.79}$
$O_3^- + H_2O + M$	$\rightarrow$	$O_3^-(H_2O) + M$	2.7×10^{-28}
$O_3^- + NO_2$	$\rightarrow$	$NO_2^- + O$	$7.5 \times 10^{-11} \times (300/T)^{0.79}$
$O_3^- + NO$	$\rightarrow$	$NO_2^- + O_2$	$1.05 \times 10^{-12} \times (300/T)^{2.15}$
$O_3^-(H_2O) + CO_2$	$\rightarrow$	$CO_3^- + H_2O + O_2$	1.75×10^{-10}
$O_3^-(H_2O) + CO_2$	$\rightarrow$	$CO_3^-(H_2O) + O_2$	1.75×10^{-10}
$O_4^- + O$	$\rightarrow$	$O_3^- + O_2$	4×10^{-10}
$O_4^- + CO_2$	$\rightarrow$	$CO_4^- + O_2$	4.3×10^{-10}
$O_4^- + NO$	$\rightarrow$	$NO_3^-(*) + O_2$	2.5×10^{-10}
$O_4^- + H_2O$	$\rightarrow$	$O_2^-(H_2O) + O_2$	1×10^{-10}
$OH^- + O_3$	$\rightarrow$	$O_3^- + OH$	9×10^{-10}
$OH^- + NO_2$	$\rightarrow$	$NO_2^- + OH$	1.1×10^{-9}
$OH^- + CO_2 + M$	$\rightarrow$	$HCO_3^- + M$	7.6×10^{-28}
$OH^- + HCl$	$\rightarrow$	$Cl^- + H_2O$	1.0×10^{-9}
$OH^- + H_2O + M$	$\rightarrow$	$OH^-(H_2O) + M$	2.5×10^{-28}
$OH^- + Cl$	$\rightarrow$	$Cl^- + OH$	1.0×10^{-10}
$OH^- + ClO$	$\rightarrow$	$ClO^- + OH$	1.0×10^{-10}

CO_3^- + O	→	O_2^- + CO_2	1.1×10^{-10}
CO_3^- + O_2	→	O_3^- + CO_2	6.0×10^{-15}
CO_3^- + H	→	OH^- + CO_2	1.7×10^{-10}
CO_3^- + NO	→	NO_2^- + CO_2	1.0×10^{-10}
CO_3^- + NO_2	→	NO_3^- + CO_2	2×10^{-10}
CO_3^- + HCl	→	Cl^- + OH + CO_2	3.0×10^{-11}
CO_3^- + H_2O + M	→	$CO_3^-(H_2O)$ + M	1.0×10^{-28}
CO_3^- + Cl	→	Cl^- + CO_2 + O	1.0×10^{-10}
CO_3^- + Cl	→	ClO^- + CO_2	1.0×10^{-10}
CO_3^- + ClO	→	Cl^- + CO_2 + O_2	1.0×10^{-11}
CO_3^- + HNO_3	→	NO_3^- + CO_2 + OH	3.51×10^{-10}
$CO_3^-(H_2O)$ + NO	→	NO_2^- + H_2O + CO_2	3.5×10^{-12}
$CO_3^-(H_2O)$ + NO_2	→	NO_3^- + H_2O + CO_2	4.0×10^{-11}
$CO_3^-(H_2O)$ + H_2O + M	→	$CO_3^-(H_2O)_2$ + M	1.0×10^{-28}
$CO_3^-(H_2O)$ + NO_2	→	$NO_3^-(H_2O)$ + CO_2	4.0×10^{-11}
$CO_3^-(H_2O)$ + NO	→	$NO_2^-(H_20)$ + CO_2	3.5×10^{-12}
$CO_3^-(H_2O)$ + M	→	CO_3^- + H_2O + M	$7.2 \times 10^{-4} \times (300/T) \times e^{-7050/T}$
$CO_3^-(H_2O)_2$ + M	→	$CO_3^-(H_2O)$ + H_2O + M	$6.5 \times 10^{-3} \times (300/T) \times e^{-6800/T}$
CO_4^- + O_3	→	O_3^- + O_2 + CO_2	1.3×10^{-10}
CO_4^- + H	→	CO_3^- + OH	2.2×10^{-10}
CO_4^- + O	→	CO_3^- + O_2	1.4×10^{-10}
CO_4^- + NO	→	NO_3^-(*) + CO_2	4.8×10^{-11}
CO_4^- + H_2O	→	$O_2^-(H_2O)$ + CO_2	2.5×10^{-10}
CO_4^- + HCl	→	Cl^- + HO_2 + CO_2	1.2×10^{-9}
CO_4^- + Cl	→	Cl^- + CO_2 + O_2	1.0×10^{-10}
CO_4^- + ClO	→	ClO^- + CO_2 + O_2	1.0×10^{-10}
NO_2^- + H	→	OH^- + NO	3×10^{-10}
NO_2^- + NO_2	→	NO_3^- + NO	2×10^{-13}
NO_2^- + O_3	→	NO_3^- + O_2	1.2×10^{-10}
NO_2^- + HCl	→	Cl^- + HNO_2	1.4×10^{-9}
NO_2^- + Cl	→	Cl^- + NO_2	1.0×10^{-10}
NO_2^- + ClO	→	Cl^- + NO_3	1.0×10^{-10}
NO_2^- + HNO_3	→	NO_3^- + HNO_2	1.6×10^{-9}
NO_2^- + H_2O + M	→	$NO_2^-(H_20)$ + M	1.6×10^{-28}
$NO_2^-(H_20)$ + M	→	NO_2^- + H_2O + M	$5.7 \times 10^{-4} \times (300/T) \times e^{-7600/T}$
NO_3^- + O	→	NO_2^- + O_2	0.5×10^{-11}
NO_3^- + O_3	→	NO_2^- + $2O_2$	1×10^{-13}
NO_3^- + H_2O + M	→	$NO_3^-(H_2O)$ + M	1.6×10^{-28}
NO_3^- + HCl	→	Cl^- + HNO_3	1.0×10^{-12}
NO_3^- + HCl + M	→	NO_3^-(HCl) + M	$5.22 \times 10^{-28} \times (300/T)^{2.62}$
NO_3^- + HNO_3 + M	→	$NO_3^-(HNO_3)$ + M	1.45×10^{-26}
$NO_3^-(H_2O)$ + M	→	NO_3^- + H_2O + M	$1.0 \times 10^{-3} \times (300/T) \times e^{-7300/T}$
$NO_3^-(H_2O)$ + H_2O + M	→	$NO_3^-(H_20)_2$ + M	1.6×10^{-28}
$NO_3^-(H_2O)$ + N_2O_5	→	$NO_3^-(HNO_3)$ + HNO_3	7.0×10^{-10}
$NO_3^-(H_20)_2$ + M	→	$NO_3^-(H_2O)$ + H_2O + M	$1.5 \times 10^{-2} \times (300/T) \times e^{-7150/T}$
$NO_3^-(H_20)_2$ + N_2O_5	→	$NO_3^-(HNO_3)$ + HNO_3 + H_2O	7.0×10^{-10}
$NO_3^-(H_2O)$ + HNO_3	→	$NO_3^-(HNO_3)$ + H_2O	1.6×10^{-9}
$NO_3^-(HNO_3)$ + M	→	NO_3^- + HNO_3 + M	$6 \times 10^{-3} \times (300/T) \times e^{-13130/T}$
$NO_3^-(HNO_3)$ + HNO_3 + M	→	$NO_3^-(HNO_3)_2$ + M	1.0×10^{-26}
$NO_3^-(HNO_3)_2$ + M	→	$NO_3^-(HNO_3)$ + HNO_3 + M	$36.4 \times (300/T) \times e^{-8046/T}$
NO_3^-(HCl) + HNO_3	→	$NO_3^-(HNO_3)$ + HCl	7.6×10^{-10}
NO_3^-(*) + CO_2	→	CO_3^- + NO_2	1.0×10^{-11}
NO_3^-(*) + H	→	NO_2^- + OH	7.2×10^{-10}
NO_3^-(*) + NO	→	NO_2^- + NO_2	1.0×10^{-12}
NO_3^-(*) + HCl	→	Cl^- + HNO_3	1.0×10^{-12}
NO_3^-(*) + Cl	→	Cl^- + NO + O_2	1.0×10^{-10}
NO_3^-(*) + ClO	→	Cl^- + NO_2 + O_2	1.0×10^{-11}
HCO_3^- + Cl	→	Cl^- + OH + CO_2	1.0×10^{-10}
HCO_3^- + ClO	→	Cl^- + HO_2 + CO_2	1.0×10^{-9}
Cl^- + NO_2	→	NO_2^- + Cl	6×10^{-12}
Cl^- + H_2O + M	→	$Cl^-(H_2O)$ + M	2.0×10^{-29}
Cl^- + HNO_3	→	NO_3^- + HCl	2.8×10^{-9}
Cl^- + CO_2 + M	→	$Cl^-(CO_2)$ + M	$6.0 \times 10^{-29} \times (300/T)^2$
Cl^- + HCl + M	→	Cl^-(HCl) + M	1.0×10^{-27}
$Cl^-(H_2O)$ + M	→	Cl^- + H_2O + M	$2.0 \times 10^{-8} \times e^{-6600/T}$
$Cl^-(H_2O)$ + HCl	→	Cl^-(HCl) + H_2O	1.30×10^{-9}
$Cl^-(CO_2)$ + M	→	Cl^- + CO_2 + M	$2.6 \times 10^{-5} \times (300/T)^3 \times e^{-4000/T}$
Cl^-(HCl) + M	→	Cl^- + HCl + M	$3.33 \times 10^{-3} \times (300/T) \times e^{-11926/T}$
ClO^- + NO	→	Cl^- + NO_2	2.9×10^{-11}
ClO^- + NO	→	NO_2^- + Cl	2.9×10^{-12}
ClO^- + O	→	Cl^- + O_2	2.0×10^{-10}

Table A.9 Negative ion photodissociation. The sources of reaction rate coefficients are given in Turunen et al. [1996] unless stated otherwise.

$O_3^- + h\nu$	→	$O^- + O_2$	0.47	
$O_4^- + h\nu$	→	$O_2^- + O_2$	0.24	
$CO_3^- + h\nu$	→	$O^- + CO_2$	0.15	
$CO_4^- + h\nu$	→	$O_2^- + CO_2$	6.2×10^{-3}	
$CO_3^-(H_2O) + h\nu$	→	$CO_3^- + H_2O$	1.0	Peterson [1976]

Table A.10 Photodetachment of electrons from negative ions. The sources of reaction rate coefficients are given in Turunen et al. [1996].

$O^- + h\nu$	→	O + e	1.4
$O_2^- + h\nu$	→	O_2 + e	3.8×10^{-1}
$O_3^- + h\nu$	→	O_3 + e	4.7×10^{-2}
$OH^- + h\nu$	→	OH + e	1.1
$CO_3^- + h\nu$	→	CO_3 + e	2.2×10^{-2}
$NO_2^- + h\nu$	→	NO_2 + e	8.0×10^{-4}
$NO_3^- + h\nu$	→	NO_3 + e	5.2×10^{-2}

Table A.11 Electron detachment from negative ions. The sources of reaction rate coefficients are given in Turunen et al. [1996].

$O^- + O$	→	O_2 + e	1.9×10^{-10}
$O^- + NO$	→	NO_2 + e	$3.1 \times 10^{-10} \times (300/T)^{0.83}$
$O^- + O_2(^1\Delta_g)$	→	O_3 + e	3×10^{-10}
$O^- + M$	→	O + M + e	0.5×10^{-12}
$O^- + H_2$	→	H_2O + e	5.8×10^{-10}
$O_2^- + O$	→	O_3 + e	1.5×10^{-10}
$O_2^- + O_2(^1\Delta_g)$	→	$2O_2$ + e	2×10^{-10}
$O_2^- + N_2$	→	$N_2 + O_2$ + e	$1.9 \times 10^{-12} \times (300/T)^{-1.5} \times e^{-4990/T}$
$O_2^- + H$	→	HO_2 + e	1.4×10^{-9}
$O_3^- + O$	→	$2O_2$ + e	10^{-10}
$O_3^- + O_3$	→	$3O_2$ + e	10^{-10}
$OH^- + O$	→	HO_2 + e	2×10^{-10}
$OH^- + H$	→	H_2O + e	1.4×10^{-9}
$Cl^- + H$	→	HCl + e	9.6×10^{-10}

Table A.12 Ion-ion recombination.

$X^- + X^+$	→	products	$6.0 \times 10^{-8} \times (300/T)^{0.5}$	Arijs et al. [1987]
$X^- + X^+ + M$	→	products	$1.25 \times 10^{-25} \times (300/T)^4$	Arijs et al. [1987]

Table A.13 Neutral species reactions. The reaction rate coefficients have been taken from Sander et al. [2003] unless stated otherwise.

$H + O_2 + M$	→	$HO_2 + M$	$5.7 \times 10^{-32} \times (300/T)^{1.6}$	
$O(^1D) + H_2O$	→	$OH + OH$	2.2×10^{-10}	
$H + O_3$	→	$OH + O_2$	$1.4 \times 10^{-10} \times e^{-470/T}$	
$O(^1D) + CH_4$	→	$OH + CH_3$	1.5×10^{-10}	
$O(^1D) + CH_4$	→	$H_2O + CH_2O$	1.5×10^{-10}	
$O + H_2$	→	$OH + H$	$8.5 \times 10^{-20} \times T^{2.7} \times e^{-3160/T}$	
$O(^1D) + H_2$	→	$OH + H$	1.1×10^{-10}	
$O + OH$	→	$O_2 + H$	$2.2 \times 10^{-11} \times e^{120/T}$	
$OH + O_3$	→	$HO_2 + O_2$	$1.7 \times 10^{-12} \times e^{-940/T}$	
$HO_2 + O_3$	→	$OH + O_2 + O_2$	$1.0 \times 10^{-14} \times e^{-490/T}$	
$O + HO_2$	→	$OH + O_2$	$3.0 \times 10^{-11} \times e^{200/T}$	
$OH + OH$	→	$O + H_2O$	$4.2 \times 10^{-12} \times e^{-240/T}$	
$OH + HO_2$	→	$H_2O + O_2$	$4.8 \times 10^{-11} \times e^{250/T}$	
$OH + H_2$	→	$H_2O + H$	$5.5 \times 10^{-12} \times e^{-2000/T}$	
$H + HO_2$	→	$OH + OH$	$0.9 \times 8.1 \times 10^{-11}$	
$H + HO_2$	→	$H_2 + O_2$	$0.08 \times 8.1 \times 10^{-11}$	
$H + HO_2$	→	$H_2O + O$	$0.02 \times 8.1 \times 10^{-11}$	
$NO + HO_2$	→	$NO_2 + OH$	$3.5 \times 10^{-12} \times e^{250/T}$	
$HO_2 + HO_2$	→	$H_2O_2 + O_2$	$2.3 \times 10^{-13} \times e^{600/T}$	
$OH + H_2O_2$	→	$H_2O + HO_2$	$2.9 \times 10^{-12} \times e^{-160/T}$	
$OH + CO$	→	$H + CO_2$	$1.5 \times 10^{-13} \times (1 + 0.6 \times P)$	
$H_2O_2 + O$	→	$OH + HO_2$	$1.4 \times 10^{-12} \times e^{-2000/T}$	
$OH + OH + M$	→	$H_2O_2 + M$	$6.9 \times 10^{-31} \times (300/T)^{1.0}$	
$O + NO_2$	→	$NO + O_2$	$5.6 \times 10^{-12} \times e^{180/T}$	
$NO + O_3$	→	$NO_2 + O_2$	$3.0 \times 10^{-12} \times e^{-1500/T}$	
$N + NO_2$	→	$N_2O + O$	$5.8 \times 10^{-12} \times e^{220/T}$	
$N + NO$	→	$N_2 + O$	$2.1 \times 10^{-11} \times e^{100/T}$	
$N + O_2$	→	$NO + O$	$1.5 \times 10^{-11} \times e^{-3600/T}$	
$N(^2D) + O_2$	→	$NO + O$	2.95×10^{-12}	Fell et al. [1990]
$N(^2D) + O_2$	→	$NO + O(^1D)$	2.95×10^{-12}	Fell et al. [1990]
$N(^2D) + O$	→	$N + O$	6.9×10^{-13}	Fell et al. [1990]
$N(^2D) + NO$	→	$N_2 + O$	7.0×10^{-11}	Rees [1989]
$NO_2 + O_3$	→	$NO_3 + O_2$	$1.2 \times 10^{-13} \times e^{-2450/T}$	
$NO_2 + NO_3 + M$	→	$N_2O_5 + M$	$2.0 \times 10^{-30} \times (300/T)^{4.4}$	
$NO + OH + M$	→	$HNO_2 + M$	$7.0 \times 10^{-31} \times (300/T)^{2.6}$	
$OH + NO_2 + M$	→	$HNO_3 + M$	$2.0 \times 10^{-30} \times (300/T)^{3.2}$	
$OH + HNO_2$	→	$NO_2 + H_2O$	$1.8 \times 10^{-11} \times e^{-390/T}$	
$OH + HNO_3$	→	$NO_3 + H_2O$	$7.2 \times 10^{-15} \times e^{785/T}$	
$O(^1D) + N_2O$	→	$N_2 + O_2$	4.9×10^{-11}	
$O(^1D) + N_2O$	→	$NO + NO$	6.7×10^{-11}	
$O + NO_3$	→	$NO_2 + O_2$	1.0×10^{-11}	
$OH + NO_3$	→	$NO_2 + HO_2$	2.2×10^{-11}	
$NO + O + M$	→	$NO_2 + M$	$9.0 \times 10^{-31} \times (300/T)^{1.5}$	
$NO + NO_3$	→	$NO_2 + NO_2$	$1.5 \times 10^{-11} \times e^{170/T}$	
$NO_2 + O + M$	→	$NO_3 + M$	$2.5 \times 10^{-31} \times (300/T)^{1.8}$	
$NO_3 + NO_3$	→	$NO_2 + NO_2 + O_2$	$8.5 \times 10^{-13} \times e^{-2450/T}$	
$H + NO_2$	→	$OH + NO$	$4.0 \times 10^{-10} \times e^{-340/T}$	
$Cl + O_3$	→	$ClO + O_2$	$2.3 \times 10^{-11} \times e^{-200/T}$	
$ClO + O$	→	$Cl + O_2$	$3.0 \times 10^{-11} \times e^{70/T}$	
$ClO + NO$	→	$NO_2 + Cl$	$6.4 \times 10^{-12} \times e^{290/T}$	
$O + O + M$	→	$O_2 + M$	$4.7 \times 10^{-33} \times (300/T)^2$	Brasseur and Solomon [1986]
$O + O_2 + N_2$	→	$O_3 + N_2$	$6.0 \times 10^{-34} \times (300/T)^{2.4}$	
$O + O_2 + O_2$	→	$O_3 + O_2$	$6.0 \times 10^{-34} \times (300/T)^{2.4}$	
$O + O + O_2$	→	$O_3 + O$	$6.0 \times 10^{-34} \times (300/T)^{2.4}$	
$O + O_3$	→	$O_2 + O_2$	$8.0 \times 10^{-12} \times e^{-2060/T}$	
$O(^1D) + N_2$	→	$O + N_2$	$1.8 \times 10^{-11} \times e^{110/T}$	
$O(^1D) + O_2$	→	$O + O_2$	$3.2 \times 10^{-11} \times e^{70/T}$	
$O(^1D) + O_3$	→	$O_2 + O_2$	1.2×10^{-10}	
$O(^1D) + O_3$	→	$O + O + O_2$	1.2×10^{-10}	
$O(^1D) + N_2 + M$	→	$N_2O + M$	$3.5 \times 10^{-37} \times (300/T)^{0.6}$	
$O_2(^1\Delta_g) + O_2$	→	$O_2 + O_2$	$3.6 \times 10^{-18} \times e^{-220/T}$	